SINGLE AND MULTIPLE HETEROATOM INCORPORATION IN MFI ZEOLITES

A Dissertation

by

NATALY GARCIA VARGAS

Submitted to the Office of Graduate Studies of
Texas A&M University
in partial fulfillment of the requirements for the degree of

DOCTOR OF PHILOSOPHY

Approved by:

Chair of Committee,	Daniel Shantz
Committee Members,	Abraham Clearfield
	Perla Balbuena
	Hae-Kwon Jeong
Head of Department,	Nazmul Karim

December 2012

Major Subject: Chemical Engineering

ABSTRACT

Zeolites are crystalline inorganic solids that are industrially used for adsorption, ion exchange and catalysis. As catalysts, they have been particularly successful in the hydrocarbon processing industry due to their unique activities and selectivities. Zeolites are mainly used in acid catalyzed reactions, but their catalytic functionality can be diversified through the incorporation of elements that are traditionally not part of their framework. The incorporation of various elements has been studied in recent decades resulting in zeolites with potential to perform different chemistries or improve catalytic performance in existing ones. However, many of these investigations have been conducted under conditions that do not necessarily represent realistic scenarios for industrial implementation.

The main objective of this dissertation was to study the single and simultaneous framework incorporation of tin, boron, germanium and aluminum in MFI zeolites under synthesis conditions that are more in line with industrial preparations. These include the use of mixtures in alkaline media with high concentration of precursor species. The interest on tin resides on its potential for Lewis acid catalysis, while boron and germanium have potential for modulating acid strength and enhancing catalytic properties respectively. Three specific systems were studied: MFI zeolites with simultaneous incorporation of germanium and aluminum (i.e. Ge-Al-MFI zeolites), MFI zeolites with simultaneous incorporation of germanium and boron (i.e. B-Ge-MFI zeolites), and MFI zeolites with single incorporation of tin (i.e. Sn-MFI zeolites).

Systematic synthesis experiments were coupled with extensive analytical characterization in order to assess how element incorporation and zeolite physicochemical properties are affected by synthesis conditions. In addition, the catalytic activity of Sn-MFI zeolites for the hydroxylation of phenol was studied.

The general conclusion from this work is that framework incorporation of these elements is highly influenced by pH, mixture composition and the presence of sodium cations. Sodium cations are commonly included in industrial preparations through the use of sodium hydroxide, but they were found to negatively affect framework incorporation due to a tendency to form stable extra-framework impurities with the heteroatoms, especially germanium and tin. pH and mixture composition are particularly influential in controlling germanium and boron incorporation, while the incorporation of tin, its coordination environment and catalytic performance were found to depend on synthesis conditions as well as post-synthesis treatments.

To my loving parents

ACKNOWLEDGEMENTS

I would like to thank Dr. Daniel Shantz for giving me the opportunity to be part of his research group and providing the conditions for the successful development of this research project. It has been a time of professional growth that I have enjoyed very much due to his guidance, support and constant encouragement to explore my ideas and learn along the way. I also extend gratitude to my committee members, Dr. Abraham Clearfield, Dr. Perla Balbuena and Dr. Hae-Kwon Jeong for their support and involvement in this research project.

I would like to acknowledge SABIC Americas Inc. for providing financial support to carry out this investigation. In addition, I would like to acknowledge the technical support I received from Dr. Nattamai Bhuvanesh, Dr. Vladimir Bakhmoutov and Dr. Amanda Young when I required the use of XRD, NMR and UV-Vis analytical instruments.

Finally, I would like to thank my parents and brother for their unconditional love and encouragement to pursue my goals, and to my husband, for his love and endless support during the time we have shared together, and for the many fruitful technical discussions we had related to this research work.

NOMENCLATURE

A	Absorbance
A	Absorption factor (in equation 2.5)
a, b, c	Unit cell lattice constants
A_i	Area of peak corresponding to element *i*
A_j	Area of peak corresponding to element *j*
C	Concentration of the compound
c	Speed of light
d	Path length of the sample (in equation 2.11)
d, d_{hkl}	Interplanar distance in a given set of *hkl* planes
d_{exp}, d_{cal}	Experimental and calculated interplanar distance in a given set of *hkl* planes
e	Electron charge
E	Kinetic energy of the electrons passing through the analyzer
E_B	Binding energy of emitted electron
E_K	Kinetic energy of emitted electron
$\boldsymbol{F}(hkl)$	Structure factor vector for a given *hkl* plane
$F(hkl)$	Structure factor amplitude for a given *hkl* plane
F_i	Sensitivity factor of element *i*
F_j	Sensitivity factor of element *j*
f_j	Scattering factor of an atom *j*
h	Plank's constant

hkl	Miller indexes
$I(hkl)$	Intensity of the reflection peak of a given set of hkl planes
I_0, I	Intensity of incident radiation, intensity of transmitted or reflected radiation
K	Constant
Lp	Lorenz and polarization factor
m	Electron mass
N	Number of unit cells per unit volume
R_1, R_2	Radii of the inner and outer hemispheres respectively
T	Temperature factor (in equation 2.5)
T	Transmittance
V	Volume of the unit cell
x_i	Molar fraction of an element i in the sample
x_j, y_j, z_j	Spatial coordinates of an atom j

Greek symbols

α, β, γ	Unit cell angles
ΔV	Potential difference between the hemispheres
$\phi(hkl)$	Structure factor phase for a given set of hkl planes
λ	Radiation wavelength
ν	Radiation frequency
θ	Angle between the incident radiation and the scattering planes

$\rho(xyz)$	Electron density in a *xyz* point

Abbreviations and acronyms

CAT	Catechol
CP	Cross Polarization
CTMA	Cetyltrimethylammonium
D4MR	Double Four-Membered Ring
DFT	Density Functional Theory
DTA	Differential Thermal Analysis
EDS	Energy Dispersive X-ray Spectroscopy
En	Ethylenediamine
EXAFS	Extended X-ray Absorption Fine Structure
FE-SEM	Field Emission Scanning Electron Microscopy
FT-IR	Fourier Transform Infrared Spectroscopy
HAS	Hemispherical Sector Analyzer
HMF	Hydroxymethylfurfural
HMP	Hexamethylenediamine
HPLC	High Performance Liquid Chromatography
HQ	Hydroquinone
ICP	Inductive Coupled Plasma Spectroscopy
IZA	International Zeolite Association
MAS	Magic Angle Spinning

MFI	Code for the structure of Zeolite Socony **M**obil - **Fi**ve (ZSM-5)
MPV, MPVO	Meerwein-Ponndorf-Verley, Meerwein-Ponndorf-Verley-Oppenauer
NMR	Nuclear Magnetic Resonance
ONIOM	**O**ur Own **N**-Layered **I**ntegrated Molecular **O**rbital and **M**olecular Mechanics
OSDA, OSDAs	Organic Structure Directing Agent (agents)
PDA	Propylenediamine
PXRD	Powder X-ray Diffraction
rpm	Revolutions per minute
SAXS	Small-Angle X-ray Scattering
SDA, SDAs	Structure Directing Agent (agents)
SEM	Scanning Electron Microscopy
STEM	Scanning Transmission Electron Microscopy
TBAOH	Tetrabutylammonium Hydroxide
TEA	Tetraethylammonium
TEAOH	Tetraethylammonium Hydroxide
TEM	Transmission Electron Microscopy
TEOS	Tetraethyl Orthosilicate
TETA	Triethylenetetramine
TG	Thermogravimetric
TGA	Thermogravimetric Analysis
TMA	Tetramethylammonium

TMOS	Tetramethyl Orthosilicate
TPA	Tetrapropylammonium
TPABr	Tetrapropylammonium Bromide
TPAOH	Tetrapropylammonium Hydroxide
TPD	Temperature-Programmed Desorption
TPeA	Tetrapentylammonium
UHV	Ultra High Vacuum
IUPAC	International Union of Pure and Applied Chemistry
USD	United States Dollar
UV-Vis	Ultraviolet-Visible
UV-Vis-NIR	Ultraviolet-Visible-Near Infrared
XANES	X-ray Absorption Near Edge Structure
XAS	X-ray Absorption Spectroscopy
XPS	X-ray Photoelectron Spectroscopy
XRD	X-ray Diffraction
XRF	X-ray Fluorescence
ZSM-5	Zeolite Socony Mobil - Five

TABLE OF CONTENTS

Page

LIST OF FIGURES

LIST OF TABLES

CHAPTER I

INTRODUCTION

1.1 Overview

Major scientific and technologic breakthroughs throughout time have deeply influenced the human life style. Among these, the development of chemical conversion processes to obtain a variety of products ranging from fuel and fertilizers to drugs and plastics has hugely impacted modern society. Chemical reactions are at the heart of these processes, and catalysts play a key role in the reactions occurring in an efficient and economic fashion. It is estimated that nine out of ten processes in the chemical and petrochemical industries are catalytic in nature[1], with many of them involving heterogeneous catalysts. Among heterogeneous catalysts, zeolites enjoy a privileged position and are widely used. Zeolites are crystalline microporous aluminosilicates that are particularly successful catalysts for oil refining, petrochemical conversion, and production of specialty chemicals due to their unique structures[2]. Zeolites possess highly uniform molecular-sized channels and cavities that confine molecules and expose them to specific catalytic sites resulting in activities and selectivities that are unique. In addition, they have remarkable thermal and hydrothermal stability. Since the properties of zeolites are so intimately dependent on their structure, the synthesis of zeolites with improved topologies and compositions, and their fundamental understanding, has been and continues to be the target of many scientists. Even though remarkable advances in zeolite science have been accomplished in the last century, there is room for growth in

several areas, including the diversification of zeolite chemical compositions (i.e. incorporation of other elements in their framework) to expand their applications. The present dissertation makes advances in this regard. Zeolites with novel compositions that include elements such as titanium and tin have been reported to have great potential for non-traditional applications. However, investigations to understand how different parameters affect the complex synthesis process, especially under commercially relevant conditions, are still needed. Systematic synthesis experiments and extensive characterization are required to achieve this, and this dissertation attempts to do that in relation to the single and multiple incorporation of germanium, boron, aluminum and tin in MFI type zeolites.

1.2 Zeolite fundamentals

1.2.1 Definition and general properties

Zeolites are crystalline porous materials that have three-dimensional frameworks with channels and cavities of highly uniform dimensions[3]. Zeolite frameworks are formed by oxygen-bridged TO_4 tetrahedral units, with T atoms being traditionally Si or Si and Al combinations[4]. Other elements (e.g. B, Ge, Sn, Ti, Fe, Ga) can, up to some extent, be incorporated in the framework of zeolites expanding their compositional range[5]. Zeolite pores are of molecular dimensions, ranging from 3 to 15 angstroms[6], which define them as microporous under the IUPAC classification system[7].

Due to their highly uniform molecular-sized pores, zeolites can act as molecular sieves by adsorbing/excluding molecules based on their size and shape. This is a very

unique property that is industrially exploited in separation and catalytic processes. For catalytic applications in particular, the highly uniform pore systems dictate selectivity if the reactions occur inside the highly constrained channels and cavities[8].

When Al^{+3}, or any other trivalent element, is present in the zeolite, the framework becomes anionic and requires the presence of extra-framework cations to satisfy charge neutrality. The cations are located in the pore system and are exchangeable, making zeolites powerful ion-exchangers. The amount and nature of the cations dictates the ion-exchange capacity and the adsorption properties of zeolites.

Zeolites also have catalytic properties. The most important one is their ability to act as acid catalysts. Acid sites are formed when the highly mobile H^+ balances the negative charge in zeolites containing Al^{+3} or other T^{+3} atoms[9] (Figure 1.1). The strength of the acid sites can be fine tuned by modifying the type and the amount of T^{+3} atoms. Zeolites can be as acidic as strong inorganic acids[10], with the advantage that they are robust easy to handle solids. Zeolites can also have other types of active sites. They are formed when different T^{+4} atoms (e.g. Ti^{+4} and Sn^{+4}) are part of the framework. Zeolites containing Ti^{+4} and Sn^{+4} can act as Redox and Lewis acid catalysts respectively. By contacting molecules with the respective active sites in confined well-ordered spaces, zeolites catalyze reactions with activities and selectivities that many other materials cannot achieve. Zeolites also have excellent thermal and hydrothermal stabilities (crystalline SiO_2 base) necessary for many catalytic applications.

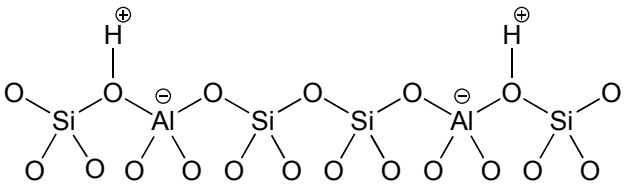

Figure 1.1 Representation of Brønsted acid sites in zeolites.

1.2.2 Brief historical background

In 1756, the Swede Alex Fredrick Cronstedt (1722-1765) was the first to recognize the existence and unique properties of natural zeolites, and offer a name and mineralogical classification for them[11]. He combined the Greek words "zein" (to boil) and "lithos" (rock) to form the word zeolite, after observing that by heating a natural zeolite it appeared to bubble and dance, as water was lost from the pores of the material[12]. Even though Cronstedt was a prominent mineralogist, zeolites remained largely unstudied for the following 200 years. They were regarded as rare minerals, found mainly as large isolated crystals in basaltic rocks[12]. Only few studies reporting on the reversibility of the hydration-dehydration cycle[13], the ion-exchange properties of zeolites[14], their ability to adsorb organic liquids[15] and the molecular sieve effect[16] surfaced in 1857, 1858, 1896 and 1925 respectively.

The first major breakthrough in zeolite science started with the work done by Richard Barrer on the sorption of gases in natural zeolites and his initial attempts to prepare synthetic zeolites. In 1948, aiming to duplicate the likely geological conditions for the formation of natural zeolites, Barrer reacted known silica materials and other aluminosilicates under high temperatures (170°C – 300°C) and autogenous pressures, and was able to synthesize mordenite[17] and ZK-5[18], the latter being the first zeolite with

no natural counterpart. Influenced by Barrer's work on the synthetic preparation of zeolites, Bob Milton, from the Linde Air Products Division of Union Carbide, used more reactive materials and milder conditions to attempt the synthesis of zeolites[12]. This approach led to the synthesis in 1950 of zeolite A and zeolite X[19,20], which are widely used in industrial processes. In subsequent years, Milton was joined by a group of other scientists (including Donald Breck, Edith Flanigen and Jule Rabo) that made profound contributions to zeolite science. In 1954, by attempting to make more stable zeolites with higher Si/Al ratios than those observed in zeolites A and X, Breck synthesized zeolite Y[21], which later became the most prominent zeolite for catalytic applications. By 1956, approximately 20 synthetic zeolites (many not having a natural counterpart) had been prepared at Union Carbide[19], and several of them produced and commercialized (starting in 1954) for use as adsorbents in separations and purifications by the same company[12]. In 1957, Jule Rabo and other members of the Union Carbide group discovered that zeolites could also exhibit acid properties and that their activity in several petroleum refining reactions was in fact far superior to that of amorphous silica/alumina acid catalysts employed at the time[22]. Union Carbide then established a practical way to synthesize H-Y zeolite, helped developed (along with Union Oil) the first zeolite-based catalytic hydrocracking process in 1959, and started the commercialization of zeolites as hydrocarbon conversion catalysts[12]. By the end of the 50s and the beginning of the 60s, other companies (that eventually became pioneers in zeolite science) were also at the same time working on similar lines. Socony Mobil researchers (including Edward Rosinsky and Charles Plank) developed metal-exchanged

acid faujasite zeolite cracking catalysts that were later estimated in 1967 to save up to 200 million barrels of oil per year[23]. Weisz and Frilette (from Socony Mobil as well) announced in 1960 that they had observed unique catalytic activities in zeolites with a NaX zeolite showing superior performance for cracking of normal alkanes with activities and selectivities that could be altered by changing the cation in the zeolite[24]. They introduced two key concepts that helped the understanding of the superior activity of zeolite versus the amorphous materials used at the time. They attributed the catalytic activity to the acidity of zeolites and, more importantly, they introduced and demonstrated the concept that the reactions took place inside the pores of the zeolites, meaning that the pore size and shape was key to the activities and selectivities[25,26]. The latter concept of size and shape selectivity is one of the most important in zeolite catalysis and it is estimated to form the base for the use of zeolites in a large number of commercial processes[12]. All of these discoveries and announcements had an enormous impact in transforming the petroleum refining industry from the 1960s until today. Zeolites became of high interest for all major petrochemical companies and they were implemented in several different refining and petrochemical processes, including the Fluid Catalytic Cracking for production of gasoline. This resulted in significant increases in yield and quality of products estimated to annually save billions of dollars[27] leading to a much more efficient and cost-effective refining industry.

Another important breakthrough in zeolite science came after Richard Barrer and Patrick Denny used tetraalkylammonium cations during the synthesis of zeolites in 1961[6]. Up to that point, syntheses only included silica and aluminum sources with

inorganic bases, resulting in zeolites with Si/Al ratios lower than 5, which made them very hydrophilic. When large organic cations were introduced, zeolites with much higher Si/Al ratios could be prepared making zeolites very hydrophobic with strong affinity for organic compounds[28,29]. These studies led to the discovery in 1967 (by Mobil researchers Robert Wadlinger, George Kerr and Edward Rosinsky) of the first high silica zeolite, zeolite beta[30] with Si/Al = 5 – 100, which became the most siliceous and most active zeolite catalyst up to that point. The discovery by Argauer, Olson and Landolt of the high silica ZSM-5 (Zeolite Socony Mobil number 5) zeolite followed and was reported in 1969[31]. All the excitement generated by these discoveries and the remarkable catalytic properties of the new materials was continued with investigations that deepened the understanding of zeolites. The next decade saw advances that included the synthesis of silicalite-1[32] (all-silica ZSM-5 by Edith Flanigen), the discovery of other high-silica and all-silica zeolites, the determination of many crystal structures using XRD, the initial development of characterization techniques such as TEM[33] and NMR[34] for the understanding of zeolites topologies and local structures, and the introduction of fluoride media for zeolite synthesis[35-37] (which later allowed the synthesis of many novel structures and heterosubstituted zeolites). During the 1980s and 1990s, AlPOs (aluminophosphates)[38,39], SAPOs (silicoaluminophosphates)[40] and mesoporous (MCM-41)[41,42] materials were discovered, marking another big advance in the field of porous materials. In addition, the synthesis of TS-1[43] (a titanium-substituted MFI zeolites with unique oxidation catalytic properties), the synthesis of zeolites with larger pore sizes than those previously known[44], and the advancement of microscopy and spectroscopy for

zeolite study was achieved[6]. In the last decade, the field of zeolites continues to be a prominent one. Many new novel zeolites have been discovered using new synthetic routes including fluoride media, incorporation of other elements during synthesis and use of high throughput experimentation. The tendencies are to prepare zeolites with larger pores sizes (so bulkier molecules can be treated), fine-tune the topology and composition of zeolites for more specialized applications and continue to pursue the understanding of the zeolite formation process.

1.2.3 Market and applications

The worldwide consumption of synthetic zeolites is estimated to be 1.7 – 2 million metric tons per year with a market value of 2 billion USD per year[45]. The main applications are in detergency, catalysis and adsorption[4] (Figure 1.2). The use of zeolites as catalysts requires 14% by weight of the supply, but it actually represents about 30% of the market value.

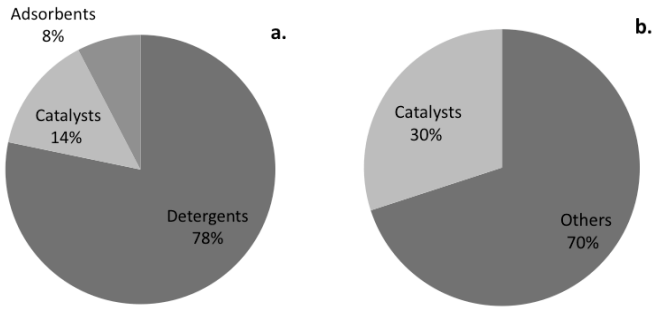

Figure 1.2 Applications of zeolites by production volume (a) and market value (b). Prepared using data published in *Introduction to Zeolite Science and Practice*[4].

Only 17 zeolite types (out of 201 known) are of commercial interest and produced synthetically[4]. FAU type zeolites are the most used for catalytic applications representing more than 95% of the zeolite catalyst market value. MFI type zeolites are the second most used, followed by BEA type zeolites. Table 1.1 shows some important industrial processes that use zeolite catalysts.

Table 1.1 Some important industrial processes that use zeolite catalysts[45,46].

Process	**Zeolites used**
Fluid catalytic cracking	*Y (FAU), ZSM-5 (MFI)*
Hydrocracking	*Y (FAU)*
Catalytic dewaxing by cracking and alkane isomerization	*ZSM-5 (MFI)*
Aromatization of short alkanes	*ZSM-5 (MFI)*
Catalytic reforming of naphtha	*L (LTL)*
Xylene isomerization	*ZSM-5 (MFI), Mordenite (MOR)*
Production of ethylbenzene	*ZSM-5 (MFI)*
Phenol hydroxylation	*TS-1 (MFI)*
Production of ε-caprolactam	*Si-1 (MFI)*

The worldwide production of natural zeolites is estimated at 3 million metric tons per year with China consuming about 80% mainly for strengthening of cement[4]. Other applications of natural zeolites are related to agriculture, horticulture, odor and pH control, and for ion exchange to remove radioactive isotopes[4].

1.2.4 Chemical structure

1.2.4.1 Framework topology

Zeolites are characteristic for having three-dimensional frameworks made of oxygen-bridged TO_4 tetrahedra. Even though TO_4 tetrahedra are the basic building units of the frameworks, several larger structural units common for different framework types

are formed when the TO_4 units connect to each other. These include cages, channels, chains and sheets, and are very useful to describe the topology of zeolite frameworks[47]. Figure 1.3 shows some of these units and how they lead to four zeolite framework types.

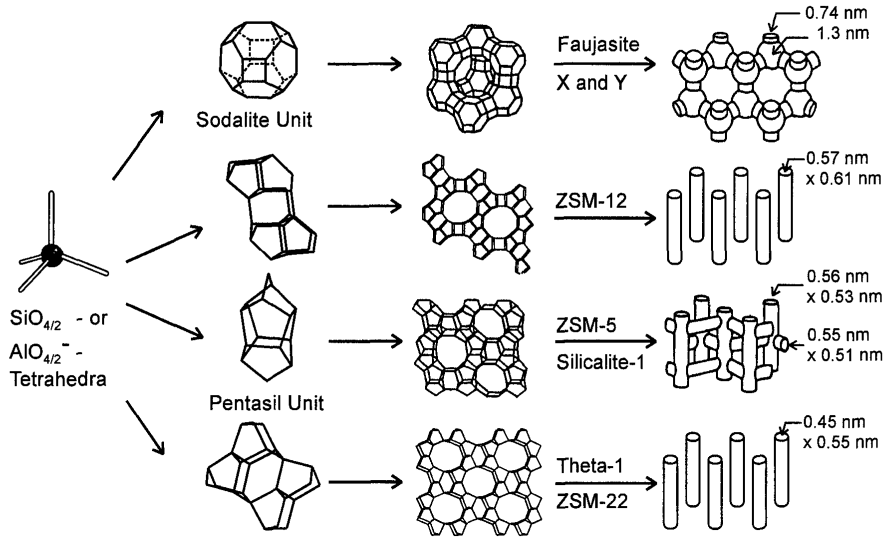

Figure 1.3 Framework topology of four selected zeolites and their building units. Adapted from Weitkamp, J., *Solid State Ionics* **2000**, 131, 175-188[27].

Due to the large number of ways in which the tetrahedra can connect, a great variety of framework types exist. So far, 201 frameworks have been identified and assigned a unique three-letter code by the International Zeolite Association (IZA) for identification[48]. Zeolite scientists have classified the different framework types based on the connectivity of the tetrahedral atoms in the highest possible symmetry without considering chemical composition or actual symmetry observed[4]. Therefore, a framework type only describes:

i. Approximate size and shape of pore openings

ii. Dimensionality of the channel system (1D, 2D, 3D)

iii. Approximate volume of the cages

iv. Types of cations available

Knowing the topology of zeolites is important because it determines the size and shape of molecules that can be admitted in the framework, their possible pathways and constrains. This is especially important to achieve unique selectivities in catalysis. Reactant, product and transition-state type selectivities are observed in zeolites[8] (Figure 1.4). In reactant selectivity, only those molecules able to enter the zeolite pore system are able to participate in the reaction and be converted. In product selectivity, only molecules able to effectively diffuse out of the pore system are seen. In transition state selectivity, only reactions carried out through a specific pathway that includes a transition state molecule that fits the size and shape of the pore system are preferred.

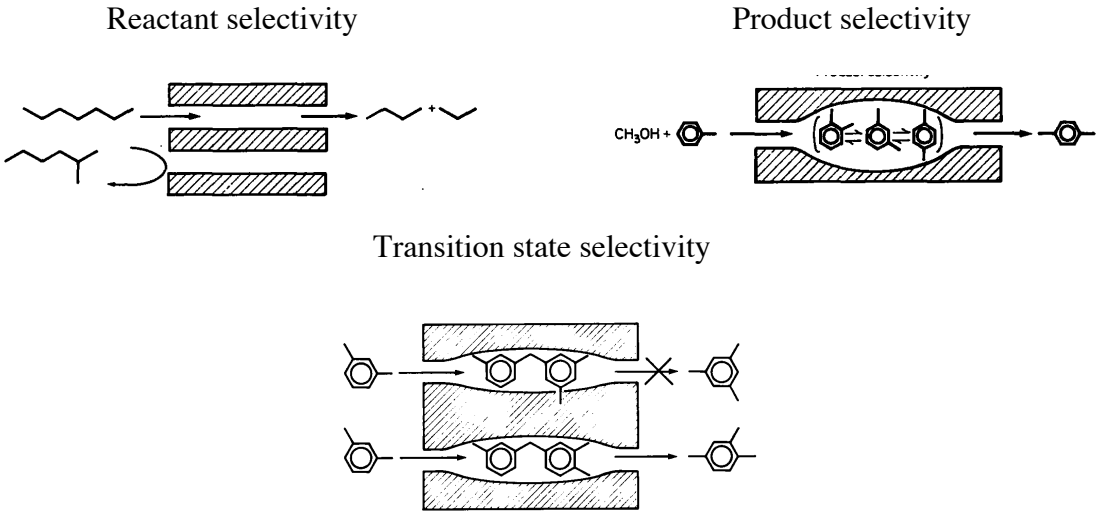

Figure 1.4 Types of zeolite shape selectivity. Adapted from Csicsery, S.M., *Zeolites* **1984**, 4, 202-213[8].

1.2.4.2 Framework composition

1.2.4.2.1 Framework atoms

Zeolites are typically composed of Si and Al (Si/Al ≥ 1). They are commonly classified as low-silica (Si/Al = 1 – 2), intermediate-silica (Si/Al = 2 – 5) and high-silica (Si/Al > 5) zeolites[49]. Many zeolites can also be made in a purely siliceous form. Zeolites containing elements such as Ti, Sn, B, Fe, Ge, and Ga in the framework have also been made. This is an area of high interest (and the major focus of this dissertation) because even small amounts of those elements can confer different catalytic properties to the zeolites. The extent of incorporation depends on synthesis conditions used (reagents, pH and media) as well as the nature of the element (size, charge, reactivity).

1.2.4.2.2 Extra-framework species

Extra-framework species are located in the channels and cavities of zeolites. They can be water molecules, organic species used for synthesis (OSDAs), and species that balance charge deficient frameworks with trivalent atoms. The latter are typically alkali metals, alkali earth metals and transition metal compounds.

1.2.4.2.3 Effect on properties

The properties of zeolites are strongly affected by their chemical composition. High-silica zeolites (Si/Al > 5) are hydrophobic and thermally stable while low-silica zeolites (Si/Al = 1 – 2) are hydrophilic with much lower stability[49]. These define what kind of applications can be carried out (high versus low temperature reactions or

polarity/affinity of molecules to adsorb). The acid strength is also determined by the number and type of T^{+3} framework atoms and it typically decreases as follows $Al^{+3} > Ga^{+3} >> B^{+3}$. Zeolites containing other elements can perform different types of catalysis, such as redox catalysis with Ti and Lewis acid catalysis with Ti and Sn[9]. Therefore, composition affects thermal and hydrothermal stability, polarity, type and strength of catalytic sites, ion exchange properties, and topological features that include unit cell volume/symmetry and size of pore openings.

1.2.4.3 The MFI structure

This dissertation focuses on zeolites with the MFI topology because it is one of the most industrially relevant. This framework type was discovered in 1963 in Socony Mobil and patented in 1969[31]. The aluminosilicate version is called ZSM-5[50] (Zeolite Socony Mobil number 5) and the siliceous version silicalite-1[32]. The MFI topology is made of pentasil chains that connect with mirror images to form corrugated sheets. The sheets have 10-ring openings and when they connect to each other a three-dimensional 10-ring channel system is formed[50] (Figure 1.5).

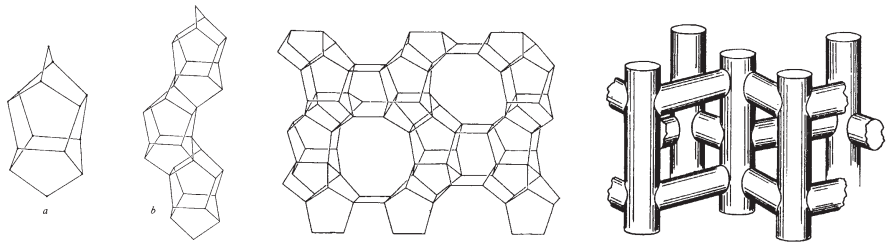

Figure 1.5 MFI framework topology and channel system. Adapted from Kokotailo G.T., Lawton S.L., Olson, D.H., *Nature* **1978**, 272, 437-438[50].

Table 1.2 highlights some of the most relevant characteristics of the MFI framework topology, the elements that have been incorporated in the framework and the related materials.

Table 1.2 Selected characteristics of the MFI framework type[5].

Channels	Straight (10R 5.3 x 5.6 Å) and sinusoidal (10R 5.1 x 5.5 Å) *Interconnected 3D channel system*
Ring types	10R, 6R, 5R and 4R
Framework density	18.4 T atoms per 1000 $Å^3$
Highest symmetry	P*nma*
T atoms per unit cell	96
O-T-O bond angles	105° – 113° (average ~ 109°)
T-O-T angles	176° and 178°
Si/Al	~ 15 – ∞
Other T atoms	Ti, B, Sn, Ge, Fe, V, Ga
Related materials	ZSM-5 (Al-MFI), Si-1 (Si-MFI), TS-1 (Ti-MFI), BOR-C (B-MFI), Sn-MFI, Fe-MFI, Ga-MFI, NU-4, NU-5, AMS-1B, AZ-1
Typical SDA	Tetrapropylammonium (TPA)

1.3 Synthesis

Zeolite formation generally occurs from solutions containing a reactive silica source, a reactive aluminum source (or a source of any other desired element), a mineralizing agent (OH^- of F^-), and, in some cases, metal cations and/or organic structure-directing agents[5]. The solutions are treated at specific conditions of temperature and pressure (typically > 100°C and > 1bar) for times that can range from a few hours to several months. Zeolite formation is driven by the precipitation of silica, which under the right conditions yields zeolitic framework types that depend on the conditions used. Even though the synthesis procedure is relatively simple, zeolite formation is a complex process. The combination of numerous soluble species and

amorphous phases with solution-precipitation, polymerization-depolymerization and nucleation-crystallization reactions makes zeolite formation very dependent on solution composition and factors such as stirring, aging and order of addition of reagents[5]. For this reason, zeolite synthesis requires a large amount of experimentation and relies on recipe-like procedures. The understanding of zeolite formation is still the most challenging problem in zeolite science, although significant advances have been made[6,49].

1.3.1 Hydrothermal synthesis route

Zeolites are mainly made using the hydrothermal route. This refers to syntheses with aqueous solutions in a closed system under relatively high temperatures and pressures[4]. Gel composition, reactant sources, pH, inorganic/organic cations, temperature, stirring, seeding and aging all affect the hydrothermal process. Among those, gel composition, reactant sources and pH are arguably the most relevant.

1.3.1.1 Gel composition

Gel composition is crucial for determining the final crystalline phase. Different phases, combination of phases (or no phases) can be obtained just by varying the water content, the type and amount of cations and structure directing agents used, or the nature and concentration of the silica and aluminum (or any other element) source[3,4]. Due to this dependency, numerous experiments covering wide compositional ranges are required to identify the preferred phases. In addition, gel composition can also affect

physicochemical properties such as final zeolite composition, crystal morphology, phase purity and local chemical environment in the zeolites.

1.3.1.2 Element sources

The chemical and physical nature of the reactants affects zeolite formation. Different silica sources (TEOS, TMOS, fumed silica, colloidal silica, sodium water-glass) and different aluminum sources (sodium aluminate, aluminum hydroxide, aluminum sulfate, aluminum isopropoxide) have different reactivity and solubility, which affects the crystallization time, the crystal morphology, particle size distribution, and in some cases (for aluminum) the crystal phase[4]. The same is true for other elements (e.g. Ti, Sn, Ge, B) where the nature of the precursor determines how readily the element can be incorporated into the growing crystal. Therefore, special attention is required to find element sources that are soluble and undergo the appropriate chemistry to facilitate zeolite synthesis.

1.3.1.3 pH

The pH is an important factor in zeolite synthesis because it controls the solubility of the reactants and the type of chemistry they undergo. Therefore, it determines in many cases the rate of zeolite crystallization, the purity of crystal phase obtained, crystal morphology and size distribution, and the extent of heteroatom incorporation in zeolites.

1.3.2 Other synthesis routes

Other and considerably less used synthetic routes for zeolite formation have been developed over the years. For instance, solvothermal routes (non-aqueous systems involving the use of organic solvents such as ethers and alcohols), ionothermal routes (use of ionic liquids), microwave-assisted hydrothermal syntheses, and fluoride routes (use of fluoride anion as mineralizing agent) have been explored[4].

The fluoride route has been particularly useful for the synthesis of new structures, large zeolite crystals and the incorporation of other elements (e.g. B, Al, Ge, Ga, Sn) into zeolite frameworks. It is reported that this route is advantageous for heteroatom incorporation because fluoride can coordinate with metals to form stable fluoride complexes that facilitate the element substitution in the framework, while in hydroxide meditated synthesis, metals ions tend to preferentially form precipitated oxide and hydroxides. However, the major drawback of this route is the use of dangerous fluoride compounds (e.g. hydrofluoric acid or ammonium fluoride), which makes commercial implementation not practical.

1.4 Heteroatom incorporation in zeolites

Heteroatom incorporation in zeolites is of high interest because it expands the zeolite compositional range and therefore their properties and potential applications. The present dissertation deals with the study of tin, germanium, aluminum and boron incorporation in MFI type zeolites. A review of the current state in these areas is given below.

1.4.1 Tin

The incorporation of tin in zeolites has been mainly motivated by the Lewis acid characteristic of this element (and therefore the potential use of tin-containing zeolites in Lewis-acid catalyzed reactions), and the fact that it is a tetravalent element that belongs to the same group of silicon in the periodic table. Even though the incorporation of tin in zeolites has not yet been as widely studied compared to other elements, there are already several promising investigations showing that tin-containing zeolites are capable of acting as Lewis acid catalysts in several reactions involving carbonyl and biomass derived compounds.

1.4.1.1 Incorporation of tin in MFI zeolites

Initial reports of tin-containing MFI zeolites were published in the patent literature[51,52]. They claimed that tin-containing MFI materials were formed when gels containing a silica source, a tin source (typically $SnCl_4$ or $SnCl_4 \cdot 5H_2O$) and tetrapropylammonium halides were used. The zeolites were made in hydroxide media with the use of alkali metal oxides and hydroxides[51] or in fluoride and hydroxide media in the absence of alkali metals[52]. In all cases, the materials were not fully characterized and little information about their properties was given. Other patents reported the incorporation of tin in the framework of zeolites containing silicon and aluminum. The incorporation of tin was done by treating the already synthesized zeolites with tin compounds or fluoride salts of tin[53,54]. However, the studies were more focused on framework types other than MFI. Regarding the open literature, the first synthesis of

Sn-MFI zeolites was reported by Mal et al[55]. Preparations in hydroxide media with TPAOH as structure directing agent, and TEOS and $SnCl_4 \cdot 5H_2O$ as silica and tin sources respectively were used. The materials made had Si/Sn ratios from 133 to 33 that corresponded well with those used in the gels. However enrichment of tin on the outer surface was observed in zeolites with Si/Sn ratios < 75. It was shown that with increasing tin content in the zeolites, the unit cell volume increased, and a shoulder at 975 cm^{-1} in the FT-IR spectra appeared suggesting that at least a fraction of the tin atoms were part of the framework. In a later publication, the authors explored different ways of mixing the reagents and the synthesis in fluoride media[56]. They concluded that a procedure in which $SnCl_4 \cdot 5H_2O$ is dissolved in $Si(OC_2H_5)_4$ (TEOS) before hydrolysis by TPAOH resulted in better materials in terms of crystallinity than procedures that involve the addition of $SnCl_4 \cdot 5H_2O$ after complete hydrolysis of TEOS. In addition, ^{29}Si MAS NMR and ^{119}Sn MAS and static NMR were used to investigate the environment of the tin atoms[56]. ^{29}Si NMR only revealed the presence of $Si(OSi)_4$ sites and Si(OH) defects with no indication of silica sites with tin atoms as nearest neighbors. ^{119}Sn static and MAS NMR studies were interpreted as tin atoms being part of the zeolite framework but mainly found in octahedral coordination, although some of them changed to tetrahedral environment upon sample dehydration. From this evidence, the authors suggested that at least a fraction of the tin atoms could be incorporated in the framework. Diffuse reflectance UV-Vis spectroscopy was also used to probe the tin local environment[57]. The UV-Vis spectra of completely dehydrated samples were compared to that of silicalite-1, SnO_2, and a tin-impregnated MFI sample. Sn-MFI samples with Si/Sn > 50

showed absorption at 205 nm while those with higher tin contents showed absorption at 205 nm and 285 nm. The absorption at 205 nm was assigned to tin atoms in a tetrahedral coordination and the one at 285 nm to SnO_2 impurities. However, it was also mentioned that upon hydration of the samples, the absorption band moved and two peaks at 221 nm and 255 nm attributed to penta coordinated and hexa coordinated tin were seen. Years after the work published by Mal, Janiszewska et al. reported on the synthesis of Sn-MFI zeolites containing either Sn(II) or Sn(IV)[58]. It was argued that incorporation of Sn(II) could lead to different material properties than those of zeolites containing Sn(IV) and efforts to accomplish the synthesis were made. Water glass, $SnCl_2$ and $SnCl_4 \cdot 5H_2O$ were respectively used as the source of silica, Sn^{+2} and Sn^{+4} ions in the presence of TPABr and NaOH. The synthesis pH was adjusted to 11 by addition of phosphoric acid. Na_2SO_3 or HCHO were used as reducing agents to prevent the oxidation of Sn(II) ions. The Sn-MFI zeolites exhibited tin contents that closely matched those used in the gels (Si/Sn = 100 to 20), although it was noticed that zeolites with Si/Sn < 40 exhibited major loss in crystallinity. The pore volume and surface area were reported to decrease with increasing tin contents in both types of zeolites. Several interesting differences were observed between the Sn(IV) and Sn(II) zeolites. First, the particle size of Sn(IV) MFI zeolites decreased with tin content, while this was not observed for Sn(II) MFI. Second, a main reduction of Sn(IV) to Sn(II) was observed for Sn(IV) zeolites while in Sn(II) MFI the major reduction was that of Sn(II) to Sn(O) as determined by TPR analysis. Third, the H-form of Sn(II) MFI zeolites exhibited a relatively large amount of weak acid sites capable of catalyzing the dehydration of

propan-2-ol while Sn(IV) MFI did not. Spectroscopic characterization using FT-IR and ^{29}Si MAS NMR was also performed leading to similar conclusions to those of Mal. A rather different synthesis approach in which Sn-MFI zeolites with Si/Sn > 50 were prepared by hydrothermal treatment of SiO_2-SnO_2 xerogels was reported by van Grieken et al[59]. The xerogels were prepared by hydrolyzing TEOS and $SnCl_4 \cdot 5H_2O$ in aqueous HCl, adding NH_4OH or TPAOH until the gel point was reached and drying at 110°C. Extensive characterization of the xerogels revealed that they contained tin in a tetrahedral coordination (UV-Vis) even at very high tin loadings (Si/Sn = 20) and that they retained higher amounts of NH_3 at higher temperatures (compared to SiO_2 xerogels) indicating some Lewis acidity. Conversion of the xerogels to Sn-MFI zeolites was only achieved from those made using TPAOH. Xerogels made with NH_4OH required much higher temperatures for crystallization and the resulting zeolites were found to have SnO_2 impurities. The Sn-MFI zeolites obtained by conversion of xerogels were compared to a Sn-MFI zeolite made following the synthesis reported by Mal. Important differences in the quality of the materials obtained through the two different routes were observed. The efficiency of tin uptake from the gels was found to be much higher through the xerogels route (33% versus 95%). In addition, characterization with UV-Vis and ^{119}Sn MAS NMR showed that Sn-MFI zeolites made from xerogels exhibited better properties in terms of tin coordination and phase purity than Sn-MFI made with the conventional route even with higher tin loadings.

1.4.1.2 Incorporation of tin in other frameworks

1.4.1.2.1 Sn-Beta

The synthesis of tin-containing zeolite Beta (*BEA) was reported by Corma et al[60]. The zeolite was exclusively prepared in fluoride media using gels with the following composition: SiO_2 : *x* SnO_2 : 0.54 TEAOH : 7.5 H_2O : 0.54 HF with Si/Sn > 100. TEOS and $SnCl_4 \cdot 5H_2O$ were used as silica and tin sources. The crystallization of the material required the use of long synthesis times ranging from 20 to 40 days and a rigid control of the water content. Extensive characterization of Sn-Beta using diverse techniques such as XRD, ICP, TEM, ^{119}Sn MAS NMR and EXAFS indicated that Sn-Beta was a highly crystalline zeolite that contained Sn^{+4} sites well distributed throughout the framework in a tetrahedral coordination (in dehydrated state) or octahedral coordination (in hydrated state)[60,61]. The stability of tin in the framework was found to be very sensitive to the calcination process. Calcination of small amounts of Sn-Beta (< 200 mg) using water saturated air at 560°C was necessary to retain the properties of the zeolite, while calcining large amounts of the material in air led to the formation of SnO_2 species within the zeolite[61]. Sn-Beta exhibits Lewis acidity due to the well-dispersed tin sites. The acidity of Sn-Beta has been probed using FT-IR spectroscopy and proven by its activity and selectivity in several Lewis acid catalyzed reactions[60,62-66]. In fact, the very unique behavior of Sn-Beta for those reactions makes it the most interesting tin-substituted zeolite reported so far.

1.4.1.2.2 Sn-MEL and Sn-MTW

The incorporation of tin in zeolites with MEL[67] and MTW[68] topologies was also reported by Mal and coworkers. The synthesis conditions used in both cases were very similar to that used for the synthesis of Sn-MFI in that gels containing TEOS, $SnCl_4 \cdot 5H_2O$, an OSDA and water were heated at 160°C for several days. The only difference was the use of other OSDAs to form the desired structure and somewhat different Si/Sn ratios. Tetrabutylammonium hydroxide (TBAOH) was used for MEL (with Si/Sn > 30) and 1,6-hexamethylene bis(benzyl dimethylammonium hydroxide) for MTW (with Si/Sn > 75). Characterization of the materials with the established techniques for tin-containing zeolites led the authors to claim that the zeolites were highly crystalline containing Sn^{+4} incorporated in the framework.

1.4.1.2.3 Mesoporous materials

Tin incorporation in several mesoporous materials has also been attempted. Das et al. made tin-containing MCM-41 (Sn-MCM-41) materials hydrothermally from gels containing fumed silica and $SnCl_4 \cdot 5H_2O$, along with CTMA and TMA as OSDAs at 110°C for several days[69,70]. The Sn-MCM-41 materials were reported to have Si/Sn ratios > 40 and exhibit slight increases in d-spacing and average pore diameter with increasing tin content. They were also reported to have Sn^{+4} ions in the framework mostly in a tetrahedral coordination (UV-Vis) and be active in reactions such as the hydroxylation of phenol and naphthol, and the epoxidation of norbornene. Corma et al. also prepared Sn-MCM-41 materials using similar hydrothermal synthesis procedures[71].

The materials were reported to catalyze the Baeyer-Villiger oxidation of bulky cyclic ketones with hydrogen peroxide with good activities and selectivities. In an effort to increase the accessibility of the tin sites present in Sn-MCM-41, the synthesis of these materials was also done by post synthesis grafting of Sn(IV) onto MCM-41 using different R_nSnCl_{4-n} precursors[72]. It was found that grafting was better achieved with precursors containing two or three chloro substituents and two or one alkyl substituents. These materials were also found to be active and selective for the Baeyer-Villiger oxidation of ketones but with slightly lower activities than those observed for Sn-MCM-41 prepared by direct hydrothermal synthesis. The grafting method on MCM-41 was also employed by Samuel et al[73]. In this case, comparisons between different alkyl groups in R_3SnCl were drawn. It was shown that the quality of the materials in terms of long range order, tin substitution and coordination, and catalytic activity for the MPV reduction of carbonyl compounds was superior in materials made using Me_3SnCl than in those made with Bu_3SnCl and Ph_3SnCl, possibly due to less steric hindrance of the smaller precursors in the MCM-41 channel walls. The incorporation of tin in SBA-15 (Sn-SBA-15) has also been claimed using different syntheses approaches[74,75].

1.4.1.3 Catalytic properties of tin-containing zeolites

Tin-containing zeolites have proven to catalyze several reactions of interest due to the ability of well-dispersed tin sites to change coordination and activate compounds. Sn-MFI was reported to catalyze the hydroxylation of phenol with hydrogen peroxide[55,57]. This reaction is practiced at industrial scale using TS-1 (Ti-MFI), which

exhibits remarkable activity. In a first communication, Mal et al. showed that one of the Sn-MFI zeolites they prepared hydrothermally (with Si/Sn = 50) was active with a phenol conversion of 20% (out of a maximum 33%) and that the selectivity of H_2O_2 towards the desired products, i.e. hydroquinone (HQ) and catechol (CAT), was 55% after 24 hours of reaction[55]. They reported that the CAT/HQ ratio after 24 hours was 3.3, and concluded that the reaction was most likely happening on tin sites well distributed on the external surface of the zeolites. However, in a later and more detailed publication they showed that Sn-MFI zeolites they made with Si/Sn = 96 to 28 were able to effectively catalyze the reaction with H_2O_2 selectivities of 50% – 70% after 24 hours (selectivity increasing with tin content)[57]. In this case, the CAT/HQ ratios were reported to be 1.6 – 1.8 under optimized conditions (lower than the previously reported value). In addition, they showed that water was a more suitable solvent than acetone, methanol or acetonitrile to carry out the reaction (in contrast to the TS-1 case). The active sites for this reaction were suggested to be well-dispersed framework Sn^{+4} sites that undergo hydrolysis to create tin sites with pending OH groups. In subsequent investigations, the same authors reported that the Sn-MEL and Sn-MTW they had also prepared were active for phenol hydroxylation with only small differences in activity and CAT/HQ ratios compared to those reported for Sn-MFI[67,68]. The activity of tin-containing zeolites was lower than that of TS-1 and reports from other research groups have not surfaced. The Sn(II) and Sn(IV) MFI zeolites prepared by Janiszewska also showed catalytic properties[58]. Sn(II) MFI catalyzed the dehydration of propan-2-ol while Sn(IV) MFI catalyzed the oxidation of cyclohexene to cyclohexanol. The different catalytic

activities (acid versus redox) were attributed to the different states of tin in the Sn(II) and Sn(IV) zeolites respectively. The synthesis of N-methylaniline by aniline alkylation with methanol has also been reported using Sn-MFI zeolites. An optimum aniline conversion of 55% and 60% selectivity towards N-methylaniline were obtained using a Sn-MFI zeolite with Si/Sn = 50[76]. Sn-Beta has been shown to catalyze the Baeyer-Villiger oxidation of saturated and unsaturated ketones with H_2O_2 to form lactones[60,62]. The activity, and more importantly, the selectivity of Sn-Beta towards the desired lactones (>98%) are remarkable, being far superior than that of other homogenous and heterogeneous catalysts developed for that reaction, and comparable to the activity of enzymes. The key to the remarkable selectivity of Sn-Beta is that the well-distributed Lewis acid tin sites are able to polarize the carbonyl compounds first, making them more reactive towards H_2O_2 attack, whereas other catalysts activate the H_2O_2 leading to reactions with the ketones and other functional groups. Sn-Beta has also been reported to catalyze the Merwein-Ponndorf-Verley and Oppenauer (MPVO) reactions for the reduction of carbonyl compounds and oxidation of alcohols[63,64]. The activity and selectivity of Sn-Beta in these reactions are very high due to a combination of shape-selectivity and appropriate Lewis acidity from the tin sites. In addition, Sn-Beta exhibits significantly better catalytic behavior for the MPVO reactions compared to that of other Lewis acid catalysts (Ti-Beta and Al-Beta). The better performance of Sn-Beta was thought to be related to a more adequate Lewis acidity of the tin sites[77,78]. The type of active Lewis acid tin sites present in Sn-Beta were extensively investigated by Corma et al. using a combination of theoretical (ONIOM and DFT) calculations and experimental

investigations that included FT-IR studies of adsorbed-desorbed deuterated acetonitrile and catalytic experiments using Sn-Beta zeolites calcined in different ways (under dry and wet air)[79]. It was concluded that two types of acid sites are present in Sn-Beta. A partially hydrolyzed framework tin site $(OSi)_3Sn(OH)$ and a fully framework coordinated tin site $Sn(OSi)_4$. It was also shown that the probe acetonitrile molecule coordinates more strongly to the partially hydrolyzed tin site suggesting that this type of site is more reactive for the Baeyer-Villiger reactions, something that was also reinforced from catalytic experiments done using catalysts treated with water saturated air. Sn-Beta has also been used as catalyst for a series of reactions involving biomass derived substrates. The isomerization of glucose to fructose in water was reported by Moliner at al[66]. Sn-Beta was able to catalyze this reaction in mixtures containing low (10 wt%) and high (45 wt%) glucose contents and also in highly acidic medium. The high activity of Sn-Beta was attributed to the combination of tin sites with the specific Beta structure since its activity was superior to that of Ti-Beta and Sn-MCM-41. The mechanism of the reaction was investigated using ^{1}H and ^{13}C NMR with isotopically labeled glucose indicating that in the presence of Sn-Beta, the glucose isomerization in water occurs via an intermolecular hydride shift[80]. The ability of Sn-Beta to carry out isomerizations in highly acidic medium was exploited to synthesize (hydroxymethyl)furfural (HMF) from carbohydrates such as glucose, starch and cellobiose in "one-pot" by coupling an acid catalyzed reaction (with HCl) with the isomerizations[81].

The Lewis acidity of tin-containing zeolites has been largely demonstrated in the literature, which has increased their interest among the catalysis community. However, not all tin-containing zeolites exhibit the same catalytic behavior. Sn-Beta zeolite is much more effective in catalyzing reactions involving carbonyl and biomass derived compounds than for example Sn-MFI and Sn-MCM-41. This clearly indicates that specific zeolite topology greatly affects the nature of the tin sites and also the possible pathways followed by the reactions.

1.4.2 Germanium

Germanium has long been considered a suitable candidate to replace silicon in the framework of zeolites due to the chemical similarities they share. Germanium is below silicon in the periodic table, and since it is also a tetravalent element, it can replace silicon without changing the framework charge. Germanates and silicates have common chemical and physical properties including polymorphism, structure types and chemical bonding. For example, GeO_2 and SiO_2 can crystallize in the rutile and quartz form[82,83]. However, bond lengths and bond angles are significantly different in GeO_2 and SiO_2 phases. The Si-O bond length for four-coordinated Si is usually between 1.6 and 1.63 Å, whereas the Ge-O distances vary from 1.7 to 1.8 Å. The Ge-O-Ge bond angle ranges from 120° – 130° while the Si-O-Si angle is typically 140° – 145°. These differences play an important role in diversifying the properties of zeolites that contain germanium in the framework.

The first attempt to incorporate germanium in zeolite synthesis was done by Barrer[3]. The initial objective was to completely replace silicon by germanium and obtain aluminogermanates with zeolite-like structures. Gels containing only aluminum and germanium precursors were utilized, but the resulting materials had significant amounts of silica derived from the glass reaction vessels used during the synthesis. The zeolites prepared were analogs of faujasite, zeolite A and harmotome containing silica, alumina and germanium. Subsequent investigations by other authors achieved the initial goal and led to the synthesis of many aluminogermanates with topologies known for zeolites such as NAT[84], CAN[85], ABW[86], ANA[87], JBW[88], MON[87], RHO[89], GIS[90] and FAU[91]. In addition, germanates with novel zeolite-like topologies were also discovered[92-97].

Even though germanates and aluminogermanates obtained have interesting adsorption properties and potential catalytic ones, they do not compare to zeolites in terms of stability, ease of synthesis and economy. Zeolites contain SiO_2 units that provide them with very high thermal and hydrothermal stability successful in many applications including catalysis. For this reason, many efforts have been devoted to the partial incorporation of germanium in zeolites, rather than the complete substitution of silica for germanium. These efforts have resulted in the modification of zeolites to obtain better properties and the discovery of many new zeolite topologies.

1.4.2.1 Incorporation of germanium in MFI zeolites

Incorporation of germanium in MFI zeolites has been the object of relatively few studies compared to other heteroatoms like aluminum, titanium, gallium and boron. However, some reports regarding the synthesis and characterization of germanium-containing MFI zeolites made in fluoride and hydroxide media have been published. Gabelica and Guth were the first to prepare Ge-MFI zeolites in fluoride media[98]. The materials were synthesized hydrothermally in the absence of alkali metal cations and using TPABr as structure directing agent. Gels containing large amounts of Ge (from $GeCl_4$) were heated at 60 – 220°C in the presence of MFI seeds with crystallization times that varied depending on temperature, pH and presence of fluoride ions. The resultant zeolites were rich in germanium with Si/Ge ≥ 2. The authors demonstrated that incorporation of germanium leads to an increase in the unit cell volume (5345 $Å^3$ for Si/Ge = ∞ and 5428 $Å^3$ for Si/Ge = 2) and an increase in the temperature of symmetry transition from monoclinic to orthorhombic in the calcined zeolites. The role of pH on the incorporation of germanium in the lattice was discussed. It was stated that in neutral or acidic media, non-framework oxides containing most of the germanium precipitate along with the MFI crystals, while in alkaline media, soluble germanates limit the introduction of germanium in the framework. In addition, it was mentioned that if alkali metal cations or ammonium hydroxide are included in alkaline media, formation of germanates that precipitate along with the MFI zeolites is observed, although no evidence was provided for this. The authors explained that formation of extra phases was avoided by adjusting the pH value to around 10 using short chain alkyl amines such

as CH_3NH_2. This synthesis work was continued with a study of the temperature of phase transition from monoclinic to orthorhombic in the calcined Ge-MFI zeolites using X-ray diffraction with a variable temperature chamber[99]. It was shown that the temperature increased with increasing germanium content in the zeolites (80°C for Si/Ge = ∞ and 238°C for Si/Ge = 2). This finding was in contrast to what had been generally observed for calcined MFI zeolites containing elements such as B, Ti, and even Al. For those zeolites, the temperature of transition actually lowers with increasing amount of heteroatoms leading to materials that exhibit orthorhombic symmetry at room temperature. A detailed investigation of the coordination state of germanium atoms in the Ge-MFI was later published[100]. Two Ge-MFI zeolites containing Si/Ge ratios of 10.5 and 5 in the as-made and calcined form were studied using X-ray absorption spectroscopy (XAS). The Ge-MFI samples were compared to a rutile-type GeO_2 (CN = 6) and a quartz-type GeO_2 (CN = 4). Data obtained from XANES and EXAFS analysis indicated that germanium was incorporated in the framework of the zeolites with tetrahedral coordination. The Ge-O bond distances in as-made samples were found to be very similar to the ones in quartz-type GeO_2 (~1.74 Å and 1.75 Å for each Ge-MFI zeolite). In addition, it was found that after calcination the Ge-O bond distances shorten and structural disorder around the germanium atom is reduced.

In a different investigation, Kosslick et al. reported the synthesis and characterization of Ge-MFI zeolites following basically the same preparation used by Gabelica and Guth[101]. Three Ge-MFI samples made from gels with Si/Ge = 11, 4 and 1.5 were studied using n-hexane adsorption, XRD, ^{29}Si MAS NMR, FT-IR and Raman

spectroscopy. The unit cell volume and a ^{29}Si MAS NMR resonance attributed to Si(1Ge) sites were shown to increase proportionally with germanium content for zeolites with Si/Ge > 11. However, in samples containing larger germanium contents, the unit cell volume did not continue to increase and the Si/Ge ratios in the framework (calculated from the ^{29}Si MAS NMR data) seemed to approach a limit of 6.5 (12.8 Ge/u.c.). Based on this experimental data, the authors concluded that the upper limit for germanium incorporation in MFI was about 12.8 atoms per unit cell. This number was rationalized by assuming that germanium replaces silicon only in energetically favored sites. Based on the ^{29}Si MAS NMR, FT-IR and Raman data, the authors suggested that the Ge-MFI framework was composed of Si(0Ge) and Si(1Ge) sites with Si-O-Si and Si-O-Ge bridges only, and that germanium does not replace silica in sites of large T-O-T angles. Even though there was a large incorporation of germanium in the MFI structure, only small changes in unit cell parameters and lattice vibration occurred, suggesting that T-T and T-O distances tend to remain unchanged. However, Raman indicated that the T-O-T angles slightly decrease in the MFI framework containing germanium and silica.

The incorporation of germanium along with aluminum in MFI zeolites has also been reported. A series of Ge-Al-MFI zeolites were synthesized and characterized by van de Water et al[102]. A parallel synthesis approach was used to find an appropriate method to simultaneously incorporate germanium and aluminum. Three synthetic routes were studied. The first one involved the use of GeO_2 and Al_2O_3 in hydroxide media (TPAOH as SDA). Poorly crystallized zeolites with GeO_2 impurities and no Al incorporation were obtained through this route. A second synthetic route involved the

use of Na_2GeO_3 and $NaAlO_2$ in fluoride media (TPABr as SDA) and led to zeolites with Ge and Al contents corresponding to those used in the gels, but with GeO_2 impurities and low crystallinity at high Ge contents. A third synthetic route was based on the preparation reported by Gabelica and Guth. This route involved $GeCl_4$ and $NaAlO_2$ in fluoride media (TPABr as SDA) and CH_3NH_2. The resulting zeolites were highly crystalline without GeO_2 impurities. Al and Ge were incorporated with efficiencies of 60 – 70% (Al) and 75 – 85% (Ge). Si/Ge ratios ranged from 25 to 6 (larger contents were not incorporated) and Si/Al ratios varied from 31 to 51. The incorporation of aluminum was probed by ^{27}Al MAS NMR and chemical analysis. Germanium incorporation was confirmed by changes in the properties of the Ge-Al-MFI materials. In general, upon germanium incorporation it was observed that the unit cell expands, the symmetry changes from monoclinic to orthorhombic at room temperature (contrary to findings by Gabelica and Guth) and that the amount of mesopores and the external surface area increases (particles formed by small rectangular crystals). The acidity of the Ge-Al-MFI zeolites was studied by NH_3-TPD and it was concluded that the acidity is not affected by germanium incorporation.

The investigations reviewed above showed that high germanium incorporation in MFI zeolites can be achieved through the use of fluoride media and $GeCl_4$. However, the use of HF is a major drawback for the potential commercial use of these materials. Investigations using hydroxide-mediated preparations are more suited for commercial applications but have received considerably less attention, at least in the open literature. Cheng et al. conducted an investigation of the synthesis and growth rates of Ge-MFI

zeolites from optically clear solutions in hydroxide media[103]. The clear solutions included TEOS, GeO_2 and $Ge(OC_2H_5)_4$ as silica and germanium precursors respectively with Si/Ge ratios from 100 to 5. TPAOH was used as structure directing agent and hydroxide source. The zeolites synthesized with this method were highly crystalline but germanium incorporation was rather low compared to what can be achieved in fluoride media. Approximately 50% (GeO_2) and 35% [$Ge(OC_2H_5)_4$] incorporation efficiencies were observed. The lower germanium incorporation was attributed to the different pH values used in the hydroxide-mediated preparations. Characterization of the materials revealed that no changes in unit cell volume, morphology or adsorption capacity were detectable with increasing germanium content. This is not surprising due to the low germanium content and the fact that changes in the physicochemical properties of Ge-MFI zeolites become detectable only at Si/Ge < 11 (as shown for the studies in fluoride media). In the same work, the growth rates of Ge-MFI zeolites from optically clear solutions were studied by in situ SAXS. It was shown that increasing amounts of germanium increase the growth rate and that, for solutions with Si/Ge < 25, reduce the induction period (6 hours to 4.5 hours). The nature of the germanium precursor also had an effect on Ge-MFI growth rates. Solutions containing GeO_2 exhibited larger growth rates than those containing $Ge(OC_2H_5)_4$ possibly due to solubility effects. This work was later expanded to study the synthesis and growth rates of Ge-Al-MFI zeolites from optically clear solutions in hydroxide media[104]. In this case, the authors demonstrated that aluminum decreased the rate of zeolite formation while germanium had the opposite effect. In addition, it was shown that large aluminum contents decreased the crystallinity

of the Ge-Al-MFI zeolites but had the opposite effect regarding the efficiency of incorporation of germanium.

1.4.2.2 Effect of germanium incorporation on catalytic properties

A first example on how the presence of germanium could affect the catalytic performance of zeolites was shown by Corma et al[105]. The condensation of benzaldehyde with ethyl cyanoacetate and ethyl malonate (to obtain intermediates for the production of dihydropyridines) was performed using two types of materials. The first one was a NaAlSi-X zeolite with Si/Al = 1.2. The second was a NaAlGe-X material (no silica) with Ge/Al = 1.03. Technically, the second material was not a zeolite since all the silica was replaced by germanium. However, its structure was that of faujasite. It was demonstrated that the activity of the NaAlGe-X material was much higher than that of the NaAlSi-X zeolite (turnover numbers 20 times higher). Since that particular condensation reaction requires the presence of basic sites, the higher activity was attributed to an increase in basicity by germanium incorporation. The reason for the increased basicity was not determined. However, it was argued that it was not related to an increase in negative charge of the framework oxygen atoms because the calculated average Sanderson's electronegativity was the same in both materials, but rather due to differences in T-O-T bond angles.

An important example in which germanium incorporation has proven to enhance the catalytic activity of zeolites was given in the patent literature[106]. Titanium-substituted zeolites and mesoporous silicas containing germanium (Si/Ge = 200 – 5)

were reported to be more effective in the epoxidation of olefins with hydrogen peroxide and other organic peroxides. For example, a TS-1 (Ti-MFI) zeolite containing germanium was reported to have better catalytic activity for the epoxidation of propylene with hydrogen peroxide than the TS-1 zeolite containing only titanium. Similar findings were later demonstrated with the activity of Ti-MCM-41 and Ti-Ge-MCM-41 materials for the epoxidation of cyclohexene with alkyl peroxides[107]. In this case, the MCM-41 surface was modified with Ge (using Bu_4Ge) prior the grafting of tetra coordinated Ti centers. Based on experimental data obtained from TEM, XAS and FT-IR experiments, the authors concluded that almost all the germanium reacts with titanium to form titanium centers that are attached to two silicons and one germanium. The catalytic performance of the Ti-Ge-MCM-41 materials was far superior to that of Ti-MCM-41 (80 – 140% higher activity). On these lines, the role of isomorphous substitution of germanium in titanium-containing zeolites (CHA and SOD as model structures) was study by Zicovich-Wilson et al. using theoretical models[108]. This work revealed that introduction of Ge close to Ti results in stabilization of the catalytic center due to the larger flexibility of GeO_4 units. In addition, it was noted that Ti centers are more influenced by structural changes created by the GeO_4 entities than by differences in electronegativity.

The catalytic activity of Ge-Al-MFI zeolites was investigated and compared to that of Al-MFI zeolites in a series of acid catalyzed test reactions[109]. It was observed that the catalytic stability was significantly improved upon germanium substitution. The deactivation of the catalysts at high temperatures occurred to a much lower extent when

germanium was present. The authors suggested that the reason for the increase in the catalyst stability was the increase in mesoporosity of the Ge-Al-MFI samples rather than changes in acid strength. The mesopores were believed to reduce the effects of pore blocking by coke formation. This experimental work was followed by a theoretical study using DFT calculations from which the authors concluded that germanium incorporation in Al-MFI zeolites only results in slight changes in the local acidity of the Brønsted acid sites but not in the whole material[110]. The catalytic improvement shown by those zeolites was rather better explained by other factors such as lattice defects or morphology changes than by changes in acid strength.

The previous examples show that germanium incorporation can lead to enhancement of the catalytic properties of some zeolites and therefore it is an area of interest for the catalysis community. Even though the incorporation of germanium does not create a particular active site, the positive catalytic effect seems to be a result of the stabilization of other active sites by increasing framework stability or by creating structural changes in the zeolites (unit cell expansion, mesoporosity) that can lead to better overall stability of the catalysts. In the present dissertation, investigations of Ge-Al-MFI and B-Ge-MFI zeolites prepared in hydroxide media are conducted with the aim to understand how different synthesis parameters affect the incorporation of germanium, boron and aluminum and the overall properties of the materials.

1.4.2.3 Structure directing effect of germanium

One of the most notable consequences of the use of germanium in the synthesis of zeolites is the stabilization of structures that contain double four-membered rings (D4MR). The average Si-O-Si bond angle in all-silica zeolites is approximately 148°. All-silica zeolites that contain D4MR tend to have lower average Si-O-Si bond angles (~145°) due the arrangement of Si atoms in the D4MR but the units are not energetically favored when only Si atoms are used. Since Ge-O-Ge and Si-O-Ge bond angles are smaller than Si-O-Si bond angles in zeolites, the incorporation of germanium in the framework results in the stabilization of D4MR. This was studied using ab initio calculations[111] and tested experimentally in the synthesis of ISV (a large pore, all-silica molecular sieve that contains D4MR) by Corma et al[112]. The inclusion of germanium resulted in a dramatic decrease of the nucleation time indicating the stabilization of the structure. The strong structure directing effect of germanium towards structures containing D4MR was subsequently demonstrated by the synthesis of polymorph C of beta (BEC) using different OSDAs. In the presence of germanium, polymorph C was always formed regardless of the type of OSDA used. When germanium was absent, different structures were obtained depending on the OSDA[113]. The introduction of germanium in zeolites synthesis has led to the discovery of many new zeolite topologies and recent years[113-118].

1.4.3 Boron

The incorporation of boron in zeolite frameworks has been a subject of study since the 1980s. The original motivation for incorporating boron, a trivalent element located above aluminum in the periodic table, was to explore the potential acid properties that boron-containing zeolites could exhibit and compare them to the well-known properties of aluminum-containing zeolites. Successful boron incorporation in many different zeolite frameworks has been accomplished over the years and convincing experimental evidence has been collected with spectroscopic characterization and catalytic testing. In general, it has been observed that the acidity of boron zeolites is considerable lower than that observed for aluminum zeolites, but sufficient to catalyzed some relevant reactions.

1.4.3.1 Incorporation of boron in MFI zeolites

In 1980, Taramasso et al. were the first to report the incorporation of boron in MFI type zeolites[119,120]. B-MFI (or BOR-C as named by the authors) was synthesized in hydroxide media from gels containing TEOS and H_3BO_3 as silica and boron sources with typical H_2O/Si and Si/B ratios of 25 – 40 and 0.5 – 2.5 respectively. Several different organic structure-directing agents (TEA, TPA, TPeA and En) were employed during the syntheses. In addition, no aluminum sources or alkali cations were included. The gels, which were reported to have pH values ranging between 8 and 11, were heated at 140°C – 175°C for 5 – 15 days yielding highly crystalline MFI materials with molar Si/B ratios ranging from 9 – 142. The experiments led to the conclusion that the upper limit for

boron incorporation in the framework was determined by the amount of OSDAs that could be accommodated in the zeolite pore system (i.e. charge compensating effects). Therefore, the use of cations with larger charge densities resulted in zeolites with higher boron incorporation. The boron incorporation in the framework of the zeolites was probed in different ways. XRD experiments confirmed the crystallinity and structure of the materials, while indicating a linear decrease of the unit cell volume and retention of orthorhombic symmetry in calcined zeolites with increasing boron contents. The linear decrease of the unit cell volume in zeolites containing boron was taken as clear indication of incorporation because such a change is expected when Si-O bonds are replaced with the shorter B-O ones. In addition, B-MFI zeolites were tested in the alkylation of benzene with ethylene and the dehydration of methanol. It was found that while both reactions are strongly catalyzed with aluminum containing zeolites, B-MFI was only active for the alkylation of benzene and not methanol dehydration. These results offered supporting evidence that boron was part of the zeolite framework and that significantly different acidities are exhibited by B-MFI zeolites. The synthesis of B-MFI zeolites was also claimed in the patent literature by Klotz at almost the same time[121]. In that case, B-MFI materials were made in alkaline media from gels containing Ludox AS-30 (silica source), H_3BO_3 (boron source), NaOH, and TPABr (OSDA). The materials, crystallized at 165°C for 7 days, were highly crystalline with Si/B ranging from 25 to 80, but were found to contain significant amounts of aluminum (570 ppm) and iron (290 ppm) due to impurities in the reagents. Following the initial works, many other investigations reported the synthesis of B-MFI zeolites and additional characterization

with other techniques. Gabelica et al. were the first to use ^{11}B MAS NMR to assess the incorporation of boron in zeolites[122]. They showed that BO_4 species have a different chemical shift when they are part of the zeolite framework than when they are found in amorphous materials. The authors found that tetrahedrally coordinated boron is characterized by a sharp single resonance in the NMR spectra, while trigonal species exhibit complex patterns characteristic of quadrupolar interactions. Following this work, Scholle et al. studied the coordination of boron in hydrated versus dehydrated B-MFI zeolites[123]. They found that in hydrated materials, framework boron is in tetrahedral coordination characterized by a single resonance due to the highly symmetric field imposed by the four oxygens coordinated to boron. However, they also found that upon dehydration of the materials, boron changes its coordination. The single resonance decreases and another resonance characterized by strong quadrupolar interactions appears, suggesting that boron adopts a trigonal coordination. The changes in boron coordination were found to be fully reversible upon hydration and dehydration cycles, and the authors concluded that trigonal boron (in dehydrated materials) was still part of the framework and was different from extra-framework trigonal species. In later synthetic investigations, Holderich et al. prepared B-MFI zeolites using HMD (hexamethylenediamine), PDA (1,2-diaminopropane) and TETA (triethylenetetramine) as OSDAs in the absence of alkali cations[124]. The materials, crystallized at 150°C – 170°C for 2 – 5 days, contained molar Si/B ~ 17 and were tested for the conversion of methanol to olefins. Howden et al. studied the synthesis of B-MFI zeolites in hydroxide media from gels containing colloidal silica, H_3BO_3, TPABr, and NaOH with Si/B ratios

from 1 – 75[125]. They reported that when using large amounts of H_3BO_3 (boron source) the pH of the gels dramatically decreased preventing crystallization. They suggested that pH values > 9.5 were preferred to allow crystallization in a few days. In addition, they made a few other important observations. First, they observed that boron incorporation was rather difficult and boron uptakes were generally below 20% of that present in the gels, meaning that large excess of boron needed to be used to achieve a target composition. The maximum Si/B ratio obtained was 36. Second, they noticed that even though the presence of sodium seemed to increase the overall boron content in the samples, it actually decreased the percent of boron that was actually incorporated in the framework, suggesting a negative effect of sodium for boron incorporation. Third, they also noticed that the thermal stability of B-MFI zeolites was considerably lower than that of Al-MFI zeolites (collapsed of the structure at 700°C versus 950°C). Several other reports on the synthesis of B-MFI zeolites in hydroxide media and their characterization with XRD, chemical analysis, FT-IR and NMR were also published[126,127]. Similar findings regarding the contraction of the unit cell with boron incorporation, the low boron uptakes and limits in substitution and the characteristic ^{11}B MAS NMR resonances for different boron coordination were reported. In a different investigation, de Ruiter et al. studied the incorporation mechanism of boron in MFI zeolites[128]. First, they noticed that the incorporation of boron required the presence of TPA cations, since mixtures containing only Na cations (no TPA) resulted in boron-free zeolites. Therefore, they suggested that the upper limit for boron incorporation in B-MFI zeolites made from mixtures containing TPA or TPA/Na cations was 4 atoms/u.c

(Si/B ~ 23), since only 4 TPA cations/u.c. are occluded in the MFI pore system. By looking at the $B(OH)_3/B(OH)_4$ equilibrium in the mixtures with the use of ^{11}B NMR, they showed that the concentration of $B(OH)_3$ species increased with increasing TPA in the mixtures while it decreased with increasing Na (for a given pH value). It was concluded that $B(OH)_3$ species are the most favorable for condensation and zeolite formation and a mechanism was proposed on that basis. The authors also showed that $B(OH)_3$ species were found in increasing concentrations with decreasing pH values, indicating that boron incorporation in zeolites should be favored at lower pH values.

The synthesis of B-MFI zeolites in fluoride media has also been studied. Guth et al. prepared a B-MFI zeolite with a Si/B ~ 30 from gels containing Aerosil 180, H_3BO_3, TPABr and NH_4F[129]. The gels were heated at 165°C for 14 days. Other syntheses in fluoride media followed[130,131]. Different silica sources and/or gel compositions, temperature and crystallization time were applied. It was demonstrated that boron could be incorporated into MFI zeolites following this route and that similar physicochemical characteristics to those materials made in hydroxide media were observed. Testa et al. demonstrated that it was possible to incorporated more than 4 B/u.c. by including alkali cations different from sodium (K and Cs)[132]. They prepared a series of B-MFI zeolites in fluoride media from mixtures containing fumed silica, H_3BO_3, TPABr, NH_4F and different fluoride salts (KF and CsF), leading to B-MFI zeolites with larger boron contents than previously achieved with TPA and TPA/Na.

From all the investigations made, it has become clear that boron can be successfully incorporated in the framework of MFI zeolites. X-ray diffraction (changes

in unit cell volume and symmetry), chemical analysis (boron content determination), and ^{11}B MAS NMR (tetrahedral/trigonal framework boron versus extra-framework species) are the techniques of preference to assess the incorporation. In addition, there is a good understanding about how many different OSDAs and alkali cations can affect the incorporation of boron in MFI zeolites. However, additional investigations describing in more detail how the pH and boron composition in synthesis gels affect the percent uptake of boron from the solutions are needed.

1.4.3.2 Catalytic properties of boron-containing zeolites

Initial catalytic reports of boron-containing zeolites were contradictory. Some authors claimed that B-MFI zeolites were able to catalyze a series of reactions that required strong acid sites (including methanol conversion to hydrocarbons, xylene isomerization, ethylbenzene dealkylation, propylene oligomerization and cracking and aromatization of olefins), while other authors reported that not being the case. The apparent contradiction was overcome when it was demonstrated that the catalytic activity of B-MFI zeolites in those and other reactions (*n*-hexane cracking, xylene isomerization, ethylbenzene dealkylation, cyclopropane isomerization, and methanol conversion to hydrocarbon) was entirely due to trace amounts of aluminum (80 – 580 ppm) found in the samples[133]. Therefore, the acidity of B-MFI zeolites is now understood to be much lower than that of Al-MFI zeolites from their catalytic behavior and acidity measurements. Nevertheless, some reactions have been carried out using B-MFI zeolites. Holderich showed that B-MFI can be used for the double-bond

isomerization in linear olefins without functional groups with the added advantage that the selectivity is not reduced by skeleton isomerization or olefin oligomerization[134]. Tarammasso et al. demonstrated that B-MFI zeolites were able do cracking of MTBE to methanol and isobutene with higher selectivities than Al-MFI due to their inability to dehydrate methanol to other compounds[119]. In the alkylation of aniline, it was shown that B-MFI zeolite were preferentially selective for the N-alkylation while Al-MFI zeolites catalyzed both the N-alkylation and C-alkylation. One of the most widely studied application of B-MFI zeolites is the vapor phase Beckmann rearrangement of cyclohexanone oxime[135]. It was shown that these materials exhibited very high activities and selectivities (>95%) for this reaction[136]. The active sites for this reactions were determined to be silanol nests and vicinal-bridged hydroxyl groups, but it was also observed that the presence of boron species in B-MFI zeolites (specially those in trigonal coordination) were very beneficial in terms of activity and stability[137].

1.5 Dissertation scope and organization

The introduction presented in this chapter shows that incorporation of elements like tin, germanium and boron in the framework of zeolites is a powerful tool to modify and diversify their catalytic properties. Boron incorporation can be used to modulate the acid strength of conventional aluminum-containing zeolites or to target applications that benefit from the weak acidity they posses. Tin incorporation offers great potential to target reactions that require the use of Lewis acid catalysts, while the incorporation of germanium has proven beneficial to improve the catalytic performance in some

applications by stabilizing specific catalytic centers or modifying physicochemical properties. The efforts made so far have provided a strong base to understand how incorporation of these elements can be achieved using various synthesis conditions and how those conditions affect the general physicochemical and catalytic characteristics of the zeolites. However, there is still need to investigate in more detail the incorporation of these elements under conditions that are more attractive for industrial implementation, since in cases such as germanium and tin, the zeolites with reported better characteristics have been mainly prepared using fluoride media. The general scope of this dissertation is to investigate the single and simultaneous incorporation of tin, boron, germanium and aluminum in MFI zeolites using synthesis conditions that are more in line with industrial preparations. These include the use of mixtures in hydroxide media with high concentration of solids and the use of less reactive reagents. Special attention is focused on describing how synthesis parameters like pH and gel composition affect incorporation of the elements and the overall properties of the zeolites.

More specifically, chapter III deals with the synthesis and characterization of a series of Ge-Al-MFI zeolites prepared in alkaline media and a detailed description of how gel composition and presence of sodium cations affect their properties. This is relevant because Ge-Al-MFI zeolites have been reported to be advantageous in several applications but have been almost exclusively made in fluoride media.

Chapter IV deals with the synthesis of B-Ge-MFI zeolites from alkaline mixtures and gives a detailed description of the properties of the materials prepared and how their composition can be tuned by modifying pH and element content in the mixtures. This is

relevant because it is the first reported synthesis of the simultaneous incorporation of boron and germanium in MFI zeolites, and because the incorporation of germanium could potentially offer different catalytic behavior than that observed in zeolites containing only boron.

Chapter V reports on the synthesis of Sn-MFI zeolites from mixtures in alkaline media and describes in detail the effect of sodium ions on the incorporation of tin and the purity of the materials. Chapter VI deals with the catalytic testing of the Sn-MFI zeolites on the hydroxylation of phenol.

Chapter II describes the experimental and analytical procedures used for the synthesis and characterization of the zeolites, in addition to a brief background on the theory and use of some relevant analytical techniques. Conclusions and recommendations for future investigations are given in Chapter VII.

CHAPTER II

EXPERIMENTAL METHODS

This chapter describes the experimental procedures used for zeolite synthesis and characterization, and a brief background of some of the analytical techniques employed. Materials used, zeolite synthesis procedures, analytical experiments and catalytic testing protocols are first described in the experimental section. Later, in the analytical methods section, a brief description of the theory and the use of powder X-ray diffraction, X-ray photoelectron spectroscopy and ultraviolet-visible spectroscopy for zeolite characterization is given.

2.1 Experimental

2.1.1 Materials

2.1.1.1 Zeolite synthesis

Ludox AS-40 (colloidal silica, 40 wt% in water) was obtained form Aldrich and used as the silica source unless noted otherwise. Tetraethyl orthosilicate (>99%) and fumed silica obtained from Aldrich were used as alternative silica sources in some syntheses. Sodium aluminate ($NaAlO_2 .xH_2O$) was obtained from EM Science and used as the aluminum source for Ge-Al-MFI zeolites. Germanium (IV) oxide (99.99%) obtained from Aldrich and Germanium (IV) oxide (99.98%) obtained from Alfa Aesar were used as the germanium source for Ge-Al-MFI and B-Ge-MFI zeolites respectively. Boric acid (99.5%) was obtained from BDH and used as the boron source for B-Ge-MFI

zeolites. Tin (IV) chloride pentahydrate (98%) was obtained from Acros Organics and used as the tin source for Sn-MFI zeolites. Tetrapropylammonium hydroxide (40 wt% in water) and tetrapropylammonium bromide (98%) were obtained from Alfa Aesar and used as organic structure directing agents. Sodium hydroxide (97%) and glacial acetic acid (99.7%) were obtained from BDH and EM Science respectively. All chemicals were used as received.

2.1.1.2 Catalytic testing

Phenol (99.5%) was obtained from Aldrich. Hydrogen peroxide (30%) was obtained from Aldrich and BDH. Ultrapure hydrogen peroxide (30% ULTREX) was obtained from J.T. Baker. Catechol (99%), hydroquinone (99%) and benzoquinone (98%) were obtained from Alfa Aesar and used to confirm the identity of the phenol hydroxylation reaction products. All chemicals were used as received.

2.1.2 Synthesis procedures

2.1.2.1 Ge-Al-MFI zeolites

Ge-MFI samples were synthesized from mixtures of molar composition x SiO_2: y GeO_2: 0.27 NaOH: 0.21 TPAOH: 15 H_2O, where Si + Ge = 1 and Si/Ge = 10, 25 and 50. Al-MFI samples were synthesized from mixtures of molar composition x SiO_2: z $NaAlO_2$: 0.27 NaOH: 0.21 TPAOH: 15 H_2O, where Si + Al = 1 and Si/Al = 50 and 100. Ge-Al-MFI samples were synthesized from mixtures of molar composition x SiO_2: y GeO_2: z $NaAlO_2$: 0.27 NaOH: 0.21 TPAOH: 15 H_2O, where Si + Al + Ge = 1, Si/Ge =

10, 25 and 50 and Si/Al = 50 and 100 for each Si/Ge. Mixtures were heated at 160°C for 3 days with rotation at 60 rpm. In all syntheses containing germanium, acetic acid (1.8 g AcOH in 5.4 ml H_2O) was added to the synthesis mixture to adjust the pH in the range of 8 to 11. For reference purposes, a silicalite-1 (Si-MFI) sample was synthesized from a mixture of composition SiO_2: 0.27 NaOH: 0.21 TPAOH: 15 H_2O.

As an example, for the synthesis of Ge-Al-MFI (Si/Al = 50, Si/Ge = 10), 0.93 g of NaOH were dissolved in 9 ml of deionized water followed by the addition of 0.805 g of GeO_2. The mixture was stirred for approximately 10 min until the GeO_2 appeared to dissolve. Then, 11.42 g of Ludox AS-40 were added and the mixture stirred for 15 min. A solution of 0.14 g of $NaAlO_2$ in 2.5 ml of deionized water was prepared and added to the synthesis mixture with further stirring for 10 min. To this solution, 8.0 g of TPAOH solution (40%) were added drop wise and the stirring continued for 1.5 h. A solution of 1.8 g of acetic acid in 5.4 ml of deionized was prepared and added drop wise to the synthesis mixture. The stirring was continued for another 10 min. The pH of the synthesis mixture at this point was measured to be approximately 10.5. The synthesis mixture was then transferred to a Teflon lined autoclave (internal volume 45 ml) and the autoclave fixed in a rotary oven. The hydrothermal synthesis was carried out with agitation (60 rpm) at 160°C for 3 days under autogeneous pressure. After this, the contents of the autoclave were centrifuged and washed 5 times, each time with 50 ml of deionized water. Then, the sample was rinsed with three portions of 30 ml of 0.1M NH_4OH solution, filtered and dried overnight at 100°C. The resulting material was

calcined in air at 300°C for 3 h, followed by 550°C for 6 h using a temperature ramp of 1°C/min.

The samples made with germanium were treated with $NaNO_3$ solutions. One gram of each sample was treated using 50 ml of a 0.5 M $NaNO_3$ solution at room temperature for 2 h. Then, the samples were filtered, washed with 250 ml of deionized water, and the entire procedure repeated two more times. After this, the samples were calcined in air at 280°C for 3 h using a temperature ramp of 1°C/min.

2.1.2.2 B-Ge-MFI zeolites

2.1.2.2.1 Syntheses with variable heteroatom content

Two sets of zeolites were made in this case. The first set included TPAOH as the only structure directing agent precursor to keep the gel pH above 13. The second set included a combination of TPAOH and TPABr to obtain gels with pH values below 12. The zeolites were made from gels of composition SiO_2: *x* H_3BO_3: *y* GeO_2, 0.21 TPAOH: 15 H_2O and SiO_2: *x* H_3BO_3: *y* GeO_2, 0.04 TPAOH: 0.17 TPABr: 15 H_2O respectively. In both cases, the boron and germanium contents were varied by making the molar Si/(B+Ge) = 100, 75, 50, 25 and 10, with molar B/Ge = 1. The gels were heated at 160°C for 3 days (first set) and 6 days (second set) with rotation at 60 rpm.

2.1.2.2.2 Syntheses with constant heteroatom content

A set of zeolites was made from gels with constant boron and germanium contents but variable TPAOH/TPABr ratios in order to study the pH effect in more detail

and in isolation. The gel compositions were SiO_2: 0.01 H_3BO_3: 0.01 GeO_2, *z* TPAOH: *w* TPABr: 15 H_2O, with molar TPA/Si = 0.21 and molar TPABr/TPAOH = 0, 0.4, 1.1, 2.5, 3.7 and 7.4. The initial pH of the gels was 13.22, 13.17, 12.99, 12.44, 11.72 and 10.40 respectively. Gels were heated at 160°C for 3 days with rotation at 60 rpm.

As an example, B-Ge-MFI made from a gel containing Si/B = Si/Ge = 50 and TPABr/TPAOH = 4.25 (TPA/Si = 0.21) was prepared as follows: 0.1 g of H_3BO_3 were dissolved in 5 g of deionized water and then 12.2 g of Ludox AS-40 were added. After stirring for 15 min, 1.65 g of TPAOH were added drop wise and stirred for additional 15 min. Then, 0.1699 g of GeO_2 were added and the stirring was continued for 20 min. Finally, a solution containing 3.75 g of TPABr in 8.61 g of deionized water was added and the final gel was stirred for 1.5 hours. The gel was transferred to a Teflon lined autoclave and heated at 160°C for 6 days with rotation of 60 rpm. After heating, the material was collected by centrifugation, washed with a total of 2 L of deionized water in several cycles, and dried at 100°C overnight. Calcination was done in air at 150°C for 3 hours, followed by 560°C for 3 hours, and using a heating rate of 5°C/min.

2.1.2.3 Sn-MFI zeolites

2.1.2.3.1 Syntheses in the presence of sodium

The materials were synthesized from gels of composition SiO_2: *x* $SnCl_4$: 0.21 TPAOH: 0.3 NaOH: 15 H_2O where the tin content was varied by making the molar Si/Sn = 150, 100, 50, 25 and 15. In order to study the pH effect, three sets of samples were made from gels with an adjusted pH of 10.6, 12.0 and 13.2 respectively. The pH was

adjusted by adding small quantities of glacial acetic acid (50 wt%), mixing for 5 minutes, and repeating the process until the desired pH was reached. Addition of acid to obtain gels with pH of 13.2 was not necessary since they already had the desired pH value.

As an example, for the synthesis of Sn-MFI (Si/Sn = 100 and pH = 12), 1 g of NaOH was dissolved in 9.33 g of deionized water while stirring for 10 minutes. Then, 0.29 g of $SnCl_4 \cdot 5H_2O$ were added and after 15 min of stirring, 12.2 g of Ludox AS-40 (40%) were added to the solution and the mixing was continued for 20 more minutes. 8.67 g of TPAOH solution (40%) were then added drop wise and the resulting gel was stirred for 1.5 hours. Finally, the pH was adjusted to 12 by adding approximately 5.45 g of acetic acid solution following the procedure described above. The synthesis gel was transferred to a Teflon lined autoclave and allowed to react for 3 days at 160°C and 60 rpm. After reaction, the material was collected by filtration, washed with 2 L of deionized water and dried at 100°C overnight. Calcination was carried out in air at 300°C for 3 h, followed by 550°C for 7 h using a heating rate of 1°C /min. Identical reaction, separation and calcination conditions were used for all the materials made in the presence of sodium hydroxide.

2.1.2.3.2 Syntheses in the absence of sodium

The materials were synthesized from gels of composition SiO_2: x $SnCl_4$: y TPAOH: 15 H_2O where the tin content was varied by making the molar Si/Sn = 150, 100, 75, 50 and 25. In order to obtain crystalline materials, the TPAOH content was

varied along with the tin content. For Si/Sn ratios of 150 and 100, the molar TPAOH/Si ratio was 0.21 and for Si/Sn ratios of 75, 50 and 25, TPAOH/Si was 0.3, 0.4 and 0.9 respectively. In this case, the pH of the gels was always higher than 13.2 and it was not adjusted by means of acid addition. The crystallization time also varied with the tin content. For Si/Sn ratios of 150 and 100, the reaction time used was 3 days, and for Si/Sn ratios of 75, 50 and 25, the reaction time used was 6, 7 and 21 days respectively.

As an example, for the synthesis of Sn-MFI (Si/Sn = 50), 0.5809 g of $SnCl_4 \cdot 5H_2O$ were dissolved in 4.55 g of deionized water while stirring for 15 minutes. Then, 12.2 g of Ludox AS-40 (40%) were added to the solution and after 20 min of stirring, 16.51 g of TPAOH solution (40%) were added drop wise. The resulting gel was stirred for 1.5 hours. The synthesis gel was transferred to a Teflon lined autoclave and allowed to react at 160°C and 60 rpm for 7 days. After reaction, the material was collected by centrifugation (6000 rpm), washed with a total of 2 L of deionized water in several cycles and dried at 100°C overnight. The calcination process was identical to the one described in the above. The reaction (temperature and rotation), centrifugation and calcination conditions just mentioned in the example were applied to all the materials made in the absence of sodium hydroxide.

2.1.2.3.3 Syntheses for catalytic testing

Sn-MFI zeolites were prepared from gels with the following composition: SiO_2: *x* $SnCl_4$: *y* TPAOH: 15 H_2O, with molar Si/Sn = 150, 100, 75 and 50. The TPAOH/Si molar ratio was increased with increasing tin content and was equal to 0.21, 0.3, 0.4 and

0.5 respectively. The gels were heated at 160°C with corresponding crystallization times of 4, 6, 8 and 12 days. A similar synthesis protocol to the one described above for syntheses in the absence of sodium was used. A few additional Sn-MFI zeolites were prepared using fumed silica and TEOS. For the fumed silica case, gels of identical compositions to those just described were employed. The Si/Sn ratios used were 150 and 50 with TPA/Si = 0.21 and 0.5 respectively. Materials made with TEOS were prepared following a synthesis protocol and gel composition with Si/Sn = 50 described elsewhere[55].

2.1.3 Analytical

2.1.3.1 Materials characterization

Powder X-ray diffraction (PXRD) was performed using a Bruker-AXS D8 Advance Bragg-Brentano X-ray powder diffractometer with Cu $K\alpha$ radiation over a 2θ range of 5 – 50°. Peak indexing and unit cell refinement were done using the Bruker-AXS software TOPAS. X-ray fluorescence spectroscopy (XRF) experiments were performed using a Rigaku ZSX100e instrument with a Rh target. X-ray photoelectron spectroscopy (XPS) experiments were performed using a Kratos Axis Ultra Imaging X-ray photoelectron spectrometer with a monochromatic Al $K\alpha$ source under UHV conditions ($< 5 \times 10^{-9}$ Torr). Inductively coupled plasma (ICP) was done by Galbraith Laboratories. Field emission scanning electron microscopy (FE-SEM) images and energy dispersive X-ray spectroscopy (EDS) line-scans were obtained with a JEOL JSM-7500F microscope equipped with a high brightness conical field emission gun

operating at 5kV and 9kV respectively. Diffuse reflectance UV-Vis spectra were recorded using a Hitachi U-4100 UV-Vis-NIR spectrometer in the range 200 – 1000 nm. Infrared spectroscopy experiments were performed using a Nexus 670 FT-IR spectrometer from Thermo Nicolet and KBr pellets. Raman spectra were obtained using a Horiba Jobin-Yvon LabRam IR system. ^{29}Si, ^{27}Al and ^{11}B MAS NMR experiments were performed using a Bruker Advance 400 spectrometer operating at 79.49, 104.26 and 128.37 MHz respectively. ^{27}Al MAS spectra were acquired using a 2.5 μs 15° pulse with a recycle delay of 5 s, and a spinning rate of 10 kHz. ^{29}Si MAS spectra (for Sn-MFI zeolites) were recorded with a 2.5 μs pulse, high power decoupling, 25 s recycle delay and spinning rate of 4 kHz. $^{29}Si\{^{1}H\}$ CP MAS NMR was performed on the calcined sample with a contact time of 6 ms, a recycle delay of 5 s and a spin rate of 4 kHz. ^{29}Si MAS spectra (for Ge-Al-MFI zeolites) were acquired using a 2 μs 45° pulse, high-power proton decoupling, 90 s recycle delay, and a spinning rate of 5 kHz. ^{11}B MAS spectra were recorded using a pulse length of 1.2 μs, recycle delay of 5 s, and spin rate of 10 kHz. Chemical shifts were referenced to tetramethylsilane, aqueous aluminum sulfate solution and $BF_3{\cdot}OEt_2$ for ^{29}Si, ^{27}Al and ^{11}B respectively. Nitrogen adsorption experiments were performed using a Micromeritics ASAP 2010 micropore system and approximately 0.06 g of sample. The samples were degassed under vacuum at 100°C for 2 h, and then at 300°C overnight before the analysis. Micropore volumes were determined using the α_s-method. Temperature-programmed desorption of ammonia was done using a Hiden HPR-20 Series Precision Gas Analysis System. 200 mg of sample were pre-treated at 500°C for 5 hours under a helium flow of 40 sccm. Then, the

temperature was lowered to 110°C and stabilized. Adsorption of ammonia was done using a 30 sccm flow of 10% NH_3 in nitrogen for 30 min. A helium flow of 40 sccm was then used for 1 h to flush the excess of ammonia in the system. Finally TPD was performed by ramping the sample from 110°C to 550°C with a heating rate of 10°C/min and using a helium flow of 20 sccm. Ammonia desorbed was detected using a mass spectrometer. For the EXAFS experiments, the powdered samples were pressed into rectangular wafers of about 0.1 mm thickness. The measurements were performed in transmission mode at the X18B beamline of the National Synchrotron Light Source in Brookhaven National Laboratory, NY. X-ray absorption spectra were collected using a double-crystal Si(111) monochromator. The energy range was from 200 eV below to 1520 eV above the Ge K-edge (11109 eV). The incident beam intensity was measured in a 30 cm long ionization chamber filled with N_2, while the transmitted beam intensity was measured in a 30 cm long chamber filled with a 1:2 Ar:He mixture. After subtracting the smooth atomic background from the measured X-ray absorption coefficients, the edge-step normalized EXAFS functions c(k) were obtained for each data set.

2.1.3.2 Catalytic testing

Sn-MFI zeolites were tested as catalysts for the hydroxylation of phenol with hydrogen peroxide. Reactions were carried out batchwise in round bottom glass flasks (25 ml capacity) equipped with a condenser and a magnetic stirrer. Water was used as solvent. Reaction mixtures were prepared by adding water (5.6 g), phenol (0.4687 g),

catalyst (0.1 g) and hydrogen peroxide (0.187 ml) in that order. The molar H_2O/phenol and phenol/H_2O_2 ratios were 63 and 3 respectively. Reaction mixtures were heated in an oil bath at the reaction temperature prior to H_2O_2 addition, which was done using a microsyringe over a period of four hours (equal amounts every hour). The reactions were carried out for 8 and 24 hours at 80°C. After reaction, the catalyst was separated from the reaction mixture using centrifugation. Reaction mixtures were analyzed using an 1120 Compact HPLC (Agilent Technologies) equipped with an Eclipse Plus C18 column and UV detector. Analysis was done with a mobile phase of 1.5 ml/min acetonitrile/water (33/67) and injection volume of 0.3 μl.

2.2 Analytical methods

2.2.1 Powder X-ray diffraction

Zeolites are crystalline materials. This means their atoms are arranged in a periodic manner that is effectively infinite on an atomic scale[138]. The unique properties of zeolites and their applications are linked to their crystalline nature, and therefore, determining their structure (arrangement of their atoms) is vital to understand their behavior and potential use. The diffraction of X-rays is the most powerful tool to obtain this information because X-ray radiation has a wavelength of the same order of magnitude as the distances between the atoms[4]. By recording the diffraction patterns that arise from the interaction of X-rays with the periodic array of atoms in zeolites, their topologies can be elucidated.

The use of large single crystals (typically ~ 0.1 – 0.5 mm) is generally preferred for X-ray diffraction experiments and full structure determination. In that case, a crystal mounted in a diffractometer is rotated at many different angles to record the diffraction pattern as a function of crystal orientation. However, in most cases it is difficult to obtain zeolite crystals that are large and pure enough for those studies, or smaller crystal sizes are preferred for certain applications. The use of powered materials (with many small crystals, ~ < 50 μm) for diffraction experiments is possible and, it is in fact, widely done. This technique, powder X-ray diffraction (PXRD), is used in this dissertation. In PXRD, samples are placed in flat sample holders that contain enough material to ensure the crystals have all possible orientations to expose all the array of atoms to the X-rays.

In routine powder X-ray diffraction experiments, the information collected is used to identify a material that has an already known structure. The powder diffraction pattern is used as a "fingerprint" that is compared to other patterns until the structure is identified. However, when the material has an unknown structure, a full analysis using advanced refinement techniques is necessary to obtain the structural model of the zeolite.

2.2.1.1 Basic concepts and diffraction theory

The atoms in a zeolite structure are periodic giving rise to a lattice such as shown in Figure 2.1. The lattice is an infinite array of imaginary points in which every point has identical surroundings (surrounding atoms look the same from each lattice point).

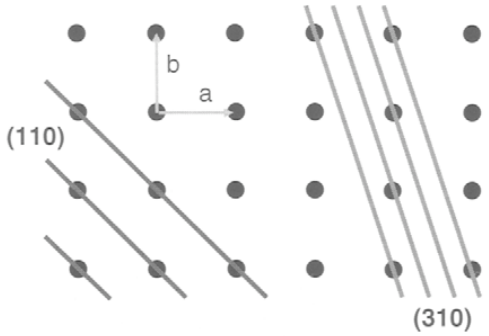

Figure 2.1 Representation of the lattice points that arise in crystalline materials and (110) and (310) set of lattice planes. The c direction is perpendicular to the page. Adapted from *Introduction to Zeolite Science and Practice*[4].

An atom may lie on a lattice point but this is not a requirement. Lattice points are usually chosen to be points of symmetry and can be related to one another by integral translations in the a, b and c directions[139]. The a, b and c vectors (with α, β and γ angles) form what it is called an unit cell. Some unit cells contain only one lattice point but others can contain two, three and four. The crystalline structure of zeolites is described by relating the atoms and their positions to the lattice points in a unit cell.

An important concept in diffraction is that lattice points in a given crystal structure form families of parallel planes with different inter planar distances (Figure 2.1). Each set of parallel planes is defined with the Miller indices *(hkl)*. The indices indicate how many times the unit cell is intersected by the planes. For example, the (110) planes intersect the a and b edges of the unit cell one time while the c edge of the unit cell is not intersected (plane is parallel to c). The (310) planes intersect the a and b edges of the unit cell three times and one time respectively while the c edge is not intersected. The importance of considering these planes is that the diffraction of X-rays

from atoms that lay on the planes is equivalent to the reflection from the planes[138]. This is defined by Bragg's law, which is explained in Figure 2.2.

When X-ray radiation of wavelength λ strikes the parallel planes at an angle θ, constructive interference (diffracted beams are in phase) will occur when the lower beam travels an extra distance AB+BC that is equal to an integer multiple of λ. Since AB+BC = $2d \sin\theta$, the wavelength λ can be related to the angle θ by the following equation.

$$n\lambda = 2d\sin\theta \tag{2.1}$$

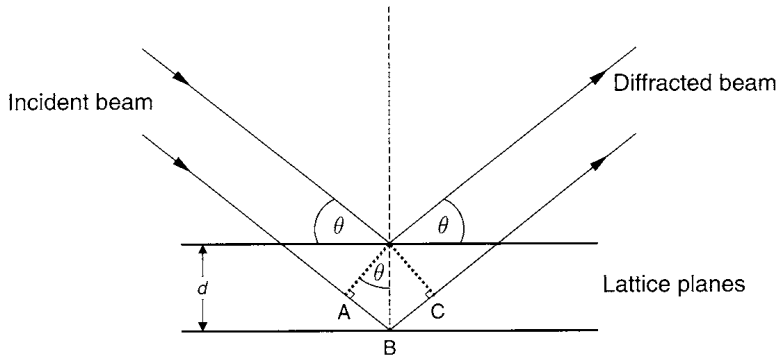

Figure 2.2 Reflection of radiation from two lattice planes. The perpendicular distance between two planes is d. Adapted from *Introduction to Zeolite Science and Practice*[4].

This indicates that when X-rays interact with a crystal, a large number of lattice planes will reflect the radiation producing constructive interference (and therefore producing a diffraction peak) only when Bragg's law is satisfied. The importance of this is that for a given radiation wavelength, the position of the diffraction peak only depends on the distance d between the planes, which is related to the size and shape of the lattice, and therefore, the size and shape of the unit cell. By obtaining the position of the

diffraction peaks from a crystal, one can determine the type and shape of the unit cell (unit cell parameters).

Even though knowing the type and shape of the unit cell is a good start, it does not entirely describe the structure of zeolites. In order to complete the description of the structure, one must also determine the type and location of the atoms inside the unit cell. This information can be extracted from the intensity of the diffraction peaks.

2.2.1.2 Intensity data from X-ray diffraction

Information about the type and number of atoms and their position in a particular plane is given by a quantity called structure factor or $\boldsymbol{F}(hkl)$. The structure factor is a vector containing an amplitude $F(hkl)$ and a phase $\phi(hkl)$. The structure factor for hkl planes is given by equation 2.2.

$$F(hkl) = \sum_{j=1}^{N} f_j \exp 2\pi i(hx_j + ky_j + lz_j) \tag{2.2}$$

In the equation, the term f_j is the scattering factor of a j atom, which describes how much a given atom scatters X-rays and therefore contains information about the type of atom and its electronic density[4]. The x_j, y_j, z_j terms define the position of the j atom in the plane while N is the number of atoms found in the plane. In mathematical terms, the structure factor is the Fourier transform of the electron density, which is given by equation 2.3 (where V is the volume of the unit cell).

$$\rho(xyz) = \frac{1}{V}\sum_{hkl} F(hkl)\exp[-2\pi i(hx + ky + lz)] \tag{2.3}$$

This is a key equation because if one can measure the structure factors amplitudes and phases for all *hkl* planes, the electron density at every point *xyz* can be determined, and with it, the location of the atoms. The intensity of an *hkl* reflection (intensity of a diffraction peak) is related to the corresponding structure factor amplitude by the following equation.

$$I(hkl) = KLp(\theta)\left|F(hkl)\right|^2 \tag{2.4}$$

In this equation, K and $Lp(\theta)$ are constants that dependent on the geometry and the diffractometer and include polarization of the X-rays used. As it can be seen, using the intensity of the diffraction peaks, the amplitude of the structure factors for all planes can be calculated. The remaining issue is to determine the phase of the structure factors, which is not straight forward because the intensity does not contain information about the phase. In order to obtain the phase of the structure factors, there are several statistical relationships that can be used. In zeolites, the most common procedure used is called direct methods. Direct methods are basically a trial-an-error procedure that requires complex computing. In essence, in direct methods, the strongest diffraction peaks are selected, the most probable phase relationships between them are set up, and then various sets of phases are tested until the best solution is found. In general, from direct methods, a few sets of phases can be found first and used to find a few atomic coordinates. From that, the remaining coordinates are usually found by using a refining method.

It has been shown so far that X-ray diffraction is a powerful technique to determine the structure of zeolites. The position of the diffraction peaks determines the

size and shape of the unit cell while the intensity contains information about the type and location of the atoms in a unit cell. The complete procedure for structure determination is fairly complex and the details will not be described here because they are out of the scope of this dissertation. In this dissertation, the zeolites made had an already known structure and their PXRD patterns were only used to confirm the phase of the materials made, check the phase purity, and determine the unit cell parameters and symmetry in order to follow changes that might be caused by the incorporation of heteroatoms in the zeolite framework. The following sections will describe how the PXRD data was collected and used to determine the information needed.

2.2.1.3 Collection of PXRD data

PXRD patterns are frequently collected using a diffractometer with Bragg-Brentano geometry (Figure 2.3). In essence, the X-rays are directed to the sample at an angle θ while a detector records the intensity of the diffracted radiation. Two types of configurations are common. In a θ/θ configuration (Figure 2.3a), the source of X-rays and the detector are moved as θ, while the sample is kept fixed. In a $\theta/2\theta$ configuration, the X-rays source is fixed while the sample and detector are moved as θ and 2θ respectively.

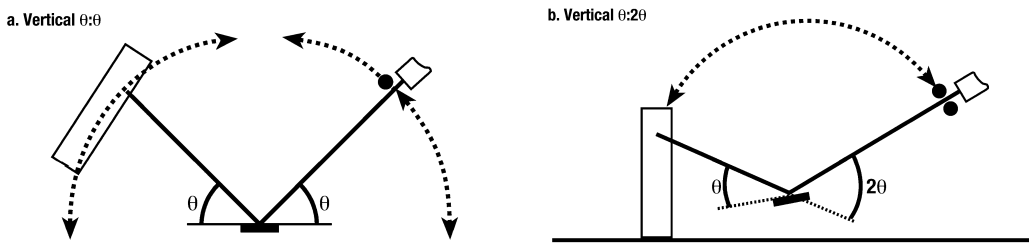

Figure 2.3 Configurations of the Bragg-Brentano diffractometer. A θ/θ configuration (a) and a $\theta/2\theta$ configuration (b). Adapted from *Zeolite Characterization and Catalysis: A Tutorial*[139].

Two of the most used types of radiation for PXRD experiments are CuKα (λ = 1.5419 Å) and MoKα (λ = 0.7107 Å) radiation. The reason why X-rays are suitable for zeolite structure determination is explained from Bragg's law (equation 2.1). From the equation it can be seen that since $\sin\theta \leq 1$, the minimum detectable *d* spacing is equal to λ/2. This is (for X-rays) in the same order of magnitude as the unit cell parameters of most zeolites, which typically vary from 5 – 80 Å.

The way diffraction patterns are recorded in powder X-ray diffraction experiments is different than in single crystal X-ray diffraction, even though X-rays interact in the same way with both types of samples. The main difference is that while diffraction from a given plane *hkl* in a single crystal is recorded as a single point; the same diffraction from a powdered material is recorded as a ring of points[138]. This is shown in Figure 2.4.

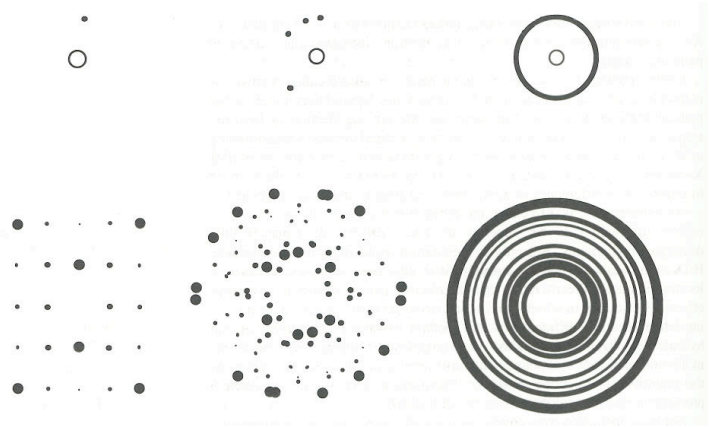

Figure 2.4 Relationship between single crystal and powder diffraction. Effect from an individual reflection (top). One reflection from a single crystal (left), four crystals with different orientations (middle) and a large number of crystals (right). Effect from a complete simple pattern (bottom). Pattern from a single crystal (left), four crystals with different orientation (middle), a large number of crystals (right). Adapted from *Crystal Structure Determination*[138].

When using a single crystal, the diffraction from a given set of planes is a single point because the given planes are all oriented in the same direction (crystal is oriented in one way at a time). However, in a powdered material, there are crystals covering all possible orientations at the same time. This means that the diffraction from each small crystal has a different orientation and therefore contributes to form the ring of points. When different angles are used, other planes will diffract the radiation producing additional rings. In the end, the PXRD pattern from a sample will basically be a series of concentric rings with different intensities (Figure 2.4).

In the diffractometer with Bragg-Brentano configuration, the detector records the intensity from each of the rings, and expresses it as a series of relative intensity peaks at different 2θ positions, resulting in diffraction patterns similar to the one shown in Figure 2.5.

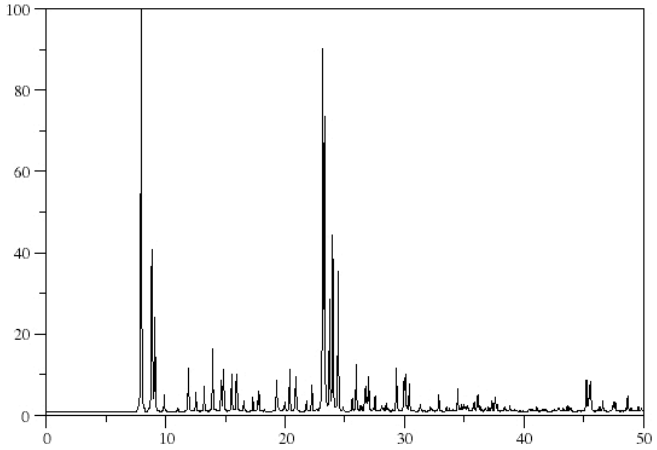

Figure 2.5 Powder diffraction pattern of a MFI zeolite (ZSM-5 in as-made form). Adapted from the International Zeolite Association, *Database of Zeolite Structures*. http://www.iza-structure.org/databases/ (accessed September 2012).

2.2.1.4 Analysis of the PXRD data

The PXRD patterns of the zeolites made in this dissertation were collected using a Bragg-Brentano diffractometer with CuKα radiation. The patterns were used to confirm that the zeolites made had in fact the MFI structure expected, and, in addition, check their crystallinity and phase purity and determine the unit cell parameters, as they can be indicative of heteroatom incorporation.

Identification of the structure was done by comparing the experimentally obtained PXRD patterns with the pattern reported by the International Zeolite Association for the MFI structure (ZSM-5 material, pattern shown in Figure 2.5) in terms of the position of the diffraction peaks (2θ) and their relative intensity.

Once the structure was confirmed, a qualitative assessment of the crystallinity was done by comparing the intensity of the diffraction peaks of the MFI zeolites

containing different heteroatoms with those of an all-silica MFI zeolite. The intensity of the diffraction peaks in reality is affected by many factors as can be seen in equation 2.5.

$$I(hkl) = \frac{N^2 e^4 \lambda^3 \nu}{2m^2 c^4} |F(hkl)|^2 \frac{T(Lp)}{A} \tag{2.5}$$

In the equation, N is the number of unit cells per unit volume, V is the volume of the crystal, and e, λ, m and c are electron charge, radiation wavelength, electron mass and speed of light respectively. $F(hkl)$ is the structure factor amplitude, (Lp) is the Lorenz and polarization factor, T is the temperature factor and A is the absorption factor. The structure factor (and therefore the type of atoms in the plane), the crystal size (N and V) and the absorption factor (A) can be particularly important when comparing two zeolites with the same structure. It is expected that by incorporating heteroatoms that have an electron density different than silica (e.g. B, Al, Ge and Sn for this dissertation) changes in the intensities of the diffraction patterns could occur. The reason for this is that heteroatoms scatter radiation differently because they don't contain the same number of electrons as the pure silica materials. In addition, heavier atoms can absorb more radiation, which leads to a decrease in the intensity of the diffraction patterns. In any case, all these factors were considered when attempting the qualitative assessment of zeolite crystallinity.

The PXRD patterns were also used to check the phase purity of the zeolites. In this case, the patterns were examined to make sure additional diffraction peaks (resulting from the presence of crystalline impurities) were not present in the patterns. Unit cell parameters were determined from the PXRD patterns. This is possible because, as

described before, the position (2θ) of the diffraction peaks is directly related to the distances between lattice points and therefore to the unit cell parameters. Since the structure of the zeolites made is known, the exact determination of the unit cell parameters is relatively straightforward because the diffraction peaks are already indexed (associated with the corresponding *hkl* indexes) and unit cell parameters reported in the literature can be used as initial estimations for determining actual values.

Determination of the unit cell parameters is performed as follows. First, the main diffraction peaks were identified and assigned the corresponding *hkl* indexes. Then, Bragg's law (equation 2.1) was used to determine the inter planar distance d_{hkl} from the 2θ position of each peak. The inter planar distance was also independently calculated from the equations that relate the distance with unit cell parameters and miller indexes. Two equations were used in this dissertation since the MFI structure is known to have either an orthorhombic unit cell or a monoclinic unit cell (equations 2.6 and 2.7 respectively).

$$d_{hkl} = \left[\frac{h^2}{a^2} + \frac{k^2}{b^2} + \frac{l^2}{c^2} \right]^{-1/2} \tag{2.6}$$

$$d_{hkl} = \left[\frac{\frac{h^2}{a^2} + \frac{l^2}{c^2} - \frac{2hl\cos\beta}{ac}}{\sin^2\beta} + \frac{k^2}{b^2} \right]^{-1/2} \tag{2.7}$$

In these equations, the unit cell parameters (a, b, c and β) were taken, as a first estimation, to be equal to unit cell parameters for a MFI material reported by the International Zeolite Association. Once the d_{hkl} distances were calculated from the

experimental data (d_{exp}) and from the equations (d_{cal}) for each series of planes, refinement of the unit cell parameters was done by least squares. In that case, the unit cell parameters are optimized in order to minimize the difference $[d_{exp} - d_{cal}]^2$. Both symmetries (orthorhombic versus monoclinic) were considered in all cases in order to determine the real symmetry exhibited by the zeolites.

In practice, the unit cell parameters determination was done using the Bruker program TOPAS, which uses sophisticated algorithms in order to extract the information needed by refining the PXRD patterns in a very fast and efficient manner.

2.2.2 X-ray photoelectron spectroscopy

X-ray photoelectron spectroscopy (XPS) is an analytical technique based on the photoelectric effect and is useful to determine the element and chemical composition of the surface of solids. In the case of zeolites, the use of XPS is advantageous because, since it is surface sensitive, it can be used to assess the element distribution across a zeolite particle and also to detect the presence of impurities that can be deposited on the outer surface. The latter point is particularly important when synthesizing zeolites with different heteroatoms (as it is the case in this dissertation) because they tend to form additional phases during synthesis if the conditions are not carefully controlled. In this dissertation, the chemical composition determined by XPS (surface composition) was compared to the chemical composition in the bulk of the zeolites in order to assess the presence of possible impurities.

2.2.2.1 Basic theory

XPS is based on the photoelectric effect, which occurs when photons of high energy interact with matter causing electrons to be ejected from it. In order to eject an electron, the energy of the photon ($h\nu$) must be larger than the binding energy of the electron (E_B). During the photoelectric effect, the energy of the photon that is not used to eject the electron is converted to kinetic energy expressed as

$$E_K = h\nu - E_B \tag{2.8}$$

where,

h = Plank's constant

ν = frequency of light source

E_K = kinetic energy of the emitted electron

E_B = binding energy of the emitted electron

Figure 2.6 is a representation of the photoelectric effect. The binding energy (E_B) is the energy required to eject an electron from an atomic orbital to the vacuum level. The binding energy is an intrinsic property and identifies the electron specifically with a parent element and an atomic orbital, thus providing a bridge for chemical identification.

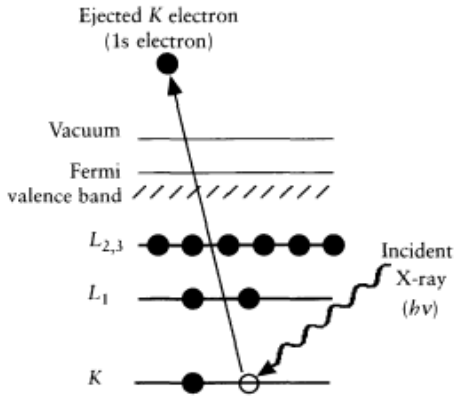

Figure 2.6 Schematic representation of the photoelectric effect showing the ejection of an electron located in a K orbital (1s orbital). Adapted from *An Introduction to Surface Analysis by XPS and AES*[140].

In XPS, the kinetic energy of electrons ejected from a given sample is measured experimentally, and then, used to calculate the binding energy of the electrons (equation 2.8) to identify the elements present in the sample. The types of electrons that are targeted in XPS experiments are core electrons, because, since they are closer to the nucleus, they "feel" the nuclear charge more strongly leading to binding energies that are specific to the parent element. Valence electrons are not suitable for chemical identification because they are relatively far from the nucleus, and are often shared through chemical bonding leading to loss in element specificity. In order to eject core electrons from a sample, photons with energies in the range of X-rays are required. The most commonly used radiations for XPS experiments are AlKα and MgKα with photon energies of 1486.6 eV and 1253.6 eV respectively.

A consequence of using photons with high enough energy to remove core electrons is that electrons located in lower energy orbitals are also ejected and recorded

in XPS experiments. Therefore, the photoelectron spectrum accurately reproduces the electronic structure of an element (Figure 2.7).

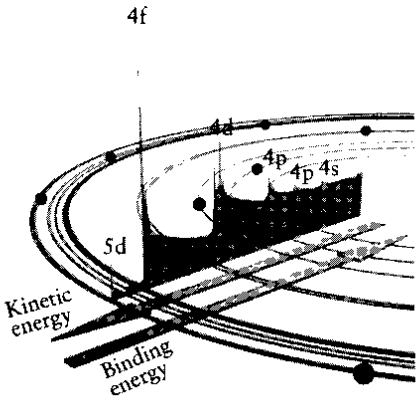

Figure 2.7 Photoelectron spectrum of lead showing how the electronic structure of an element is reproduced as a series of intensity peaks generated by the electrons ejected from each orbital. Adapted from *An Introduction to Surface Analysis by XPS and AES*[140].

The main characteristic of XPS is that it is surface sensitive. The surface sensitivity arises from the fact that only electrons located on the top layers of a solid sample are able to leave without significant loss of kinetic energy, while electrons in the bulk, due to the longer path they need to travel, undergo inelastic scattering by collision with other atoms and lose energy. The electrons from the bulk only contribute to the background of the photoelectron spectrum. The depth of analysis with XPS is in the range of a few nanometers and it is determined by a quantity known as the attenuation length (λ), which varies with the energy of the electron. In general, the depth of analysis varies with the type of sample (composition), the energy of the X-rays and the angle at which the electrons are ejected.

2.2.2.2 Collection of XPS data

During an XPS experiment, monochromatic X-rays are irradiated over a solid sample while the electrons ejected from it are passed through an analyzer to a detector. Figure 2.8 shows a schematic representation of an analysis chamber. There are several reasons for using a monochromator (which basically reduces the X-ray line width by using diffraction in a crystal lattice). Since the X-ray line widths are reduced, narrower XPS peaks are produced allowing for better chemical state analysis. In addition, the X-ray beam can be focused in a small area of the sample allowing the loading of several samples at the time, without the risk of the X-rays interfering with them while they await analysis.

Collection of XPS data needs to be carried out under ultra high vacuum (UHV) conditions to avoid the adsorption of gas molecules on the surface of the samples which can interfere with the measurements, and also to avoid losses of signals by scattering from residual gas molecules.

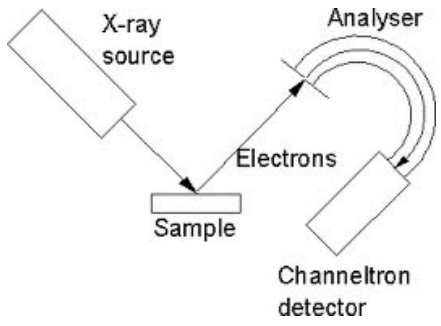

Figure 2.8 Schematic representation of a typical XPS analysis configuration.

The analyzer used in XPS experiments is called hemispherical sector analyzer (HSA). It consists of a pair of concentric hemispherical electrodes with a middle gap where the electrons pass (Figure 2.9). The analyzer is used to moderate the kinetic energy of the electrons because the energy they carry, when ejected from the sample, is too large to allow sufficient resolution.

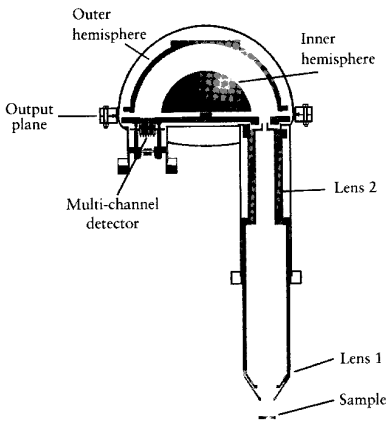

Figure 2.9 Schematic diagram of a modern hemispherical sector analyzer. Adapted from *An Introduction to Surface Analysis by XPS and AES*[140].

A potential difference is applied across the two hemispheres and the electrons only reach the detector if they have an energy given by equation 2.9, where E is the kinetic energy of the electrons, e is the charge of the electron, ΔV is the potential difference between the hemispheres and R_1 and R_2 are the radii of the hemispheres.

$$E = e\Delta V\left(\frac{R_1 R_2}{R_2^2 - R_1^2}\right) \tag{2.9}$$

During analysis, electrons with energy similar to that given by the equation will go through the analyzer and reach the detector. The voltage on the hemispheres is

scanned in a wide range to account all possible energies. The data recorded during an XPS experiment is translated into a spectrum that contains a series of intensity peaks at different binding energies (Figure 2.10). The position of the peaks (binding energy) corresponds to the binding energy of the electrons ejected from an specific orbital in an given element, while the intensity corresponds to the number of electrons ejected, which is in turn related to the concentration of the element in the samples.

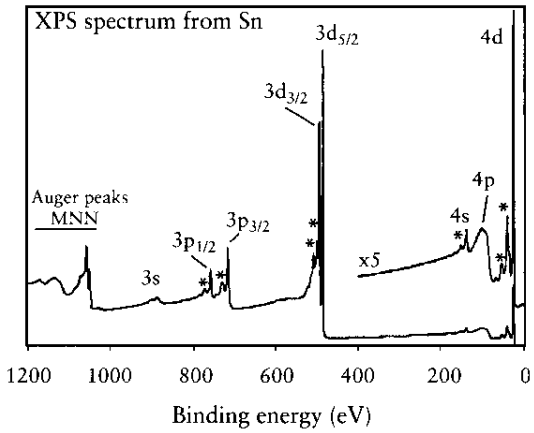

Figure 2.10 Spectrum from tin showing the XPS transitions accessible using AlKα radiation. Adapted from *An Introduction to Surface Analysis by XPS and AES*[140].

2.2.2.3 Analysis of XPS data

Once the spectrum is obtained, several types of analysis can be done. First, the binding energies of the peaks present in the spectrum are used to identify the elements present in the sample. Each binding energy corresponds to electrons ejected from a determined orbital in an element and by comparing the experimental values with tabulated ones, identification of the elements present can be done. Second, a quantitative determination of the relative concentration of elements is also possible.

This can be done using equation 2.10, where x_i is the molar fraction of a given element i in the sample, A_i is the integrated area of a given peak, F_i is the sensitivity factor for the orbital and element giving rise to the peak i (values are tabulated) and A_j and F_j are the integrated areas and sensitivity factors of all the elements present in the sample.

$$x_i = \frac{A_i / F_i}{\sum_j A_j / F_j} \tag{2.10}$$

In this dissertation, both types of analysis (identification of all elements, along with quantification of molar fractions) were performed.

2.2.3 Ultraviolet-visible spectroscopy

Ultraviolet-visible spectroscopy (UV-Vis spectroscopy) is an analytical technique that is most widely used to quantitatively determine the concentration of known compounds in solutions. UV-Vis spectroscopy is based on the absorption of radiation in the range of 200 – 800 nm (near UV and Visible range). When molecules absorb radiation in the UV-Vis range, they undergo electronic transitions from different molecular energy levels (e.g. π to π*, n to π* orbital transitions). The energy absorbed to promote electrons from their ground state orbitals to higher energy, excited state orbitals or antibonding orbitals is what it is measured in UV-Vis spectroscopy.

The Beer-Lambert Law is the mathematical basis of radiation-absorption measurements in the UV-Vis region. The law states that the concentration of a compound in solution is directly proportional to the absorbance A of the solution and the

pathlength (provided that the chemical state of the substance does not change with concentration)

$$A = k \cdot C \cdot d \tag{2.11}$$

where,

A is the absorbance

k is a constant

C is the concentration of the compound

d is the path length of the sample (width of a cell containing the solution)

The absorbance A is related to the transmittance T, which is the ratio between the intensity of the transmitted radiation and the intensity of the incident radiation I/I_0 (equation 2.12).

$$A = \log_{10}\left(\frac{I_0}{I}\right) = \log_{10}\left(\frac{100}{T}\right) = k \cdot C \cdot d \tag{2.12}$$

In UV-Vis experiments, the transmittance (and therefore the absorbance) of a solution is measured experimentally and recorded as a function of the radiation wavelength. In general, if a compound undergoes transition in the UV-Vis range, a band of absorbance will be detected at a given range of wavelengths. If the pathlength is known, the concentration of a given compound can be determined from it. The absorption bands are usually broad because not only electronic transitions are recorded, but changes in vibrational states, that require lower energy for transition, also occur.

The frequency and intensity of the absorption bands are characteristic of molecular structure, and therefore, characteristic of specific compounds.

Even though UV-Vis is in majority used for analysis of solutions containing transition metals or organic compounds, solid samples can also be analyzed with this technique. The difference of using solid samples versus solutions is that light cannot penetrate the (opaque) solids, so instead of being transmitted through the samples it is reflected from the top layers of it. Figure 2.11 shows the difference between transmission and reflection. The reflectance *R* is, in the reflection case, the ratio of the intensity of the reflected radiation and the intensity of the incident radiation I/I_0.

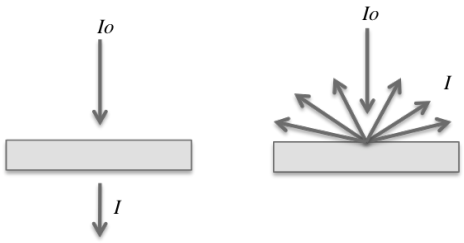

Figure 2.11 Representation of transmission (left) and reflection (right) of light.

Reflection of UV-Vis radiation from solids that contain small particles (as in the case of powdered zeolites) occurs in many directions as represented in Figure 2.11. Reflection of light in many directions (instead of perpendicular with respect to the incident beam) is referred to as diffuse reflection. Therefore, the study of the diffuse reflection of UV-Vis light is called diffuse reflectance UV-Vis spectroscopy. Diffuse reflectance UV-Vis spectroscopy is not a common analytical technique for characterization of zeolites. However, it has been increasingly used for the assessment

of the coordination environment of metals such as titanium, iron and tin when present in zeolites frameworks.

Spectra obtained from diffuse reflectance UV-Vis experiments for zeolites containing metal heteroatoms such as titanium and tin are generally useful to differentiate between metal coordination environments (i.e. tetrahedral versus octahedral coordination with oxygen atoms or various molecules). This can be done because absorption of UV-Vis radiation promotes different electronic transitions depending on the coordination in which the metals are encountered. The different electronic transitions can be identified by their corresponding absorption wavelengths in a UV-Vis spectrum. Determination of the coordination environment of metal heteroatoms in zeolites is important because it provides insights into whether a heteroatom is being successfully incorporated in the framework of if it is rather present as an impurity. In addition, the coordination environment determines in many cases the catalytic behavior of the metal in the zeolite and therefore the catalytic application of the zeolite. In this dissertation, diffuse reflectance UV-Vis was employed in order to study the coordination environment of tin in Sn-MFI zeolites made.

CHAPTER III

SYNTHESIS AND CHARACTERIZATION OF MFI ZEOLITES WITH SIMULTANEOUS INCORPORATION OF ALUMINUM AND GERMANIUM[*]

3.1 Introduction

As mentioned in Chapter I, the incorporation of germanium in aluminum-containing MFI zeolites has been previously studied. A series of Ge-Al-MFI zeolites with various germanium and aluminum contents were prepared and tested in a series of acid catalyzed reactions for which it was reported that catalysts containing germanium exhibited better catalytic stability than those containing only aluminum. Even though the potential for improving the properties of aluminum MFI zeolites by incorporation of germanium was shown, the materials were prepared using fluoride mediated preparations and highly reactive reagents. The use of these conditions is a major drawback for the potential use of this type of zeolites at industrial scale. On the other hand, the synthesis of Ge-Al-MFI zeolites in hydroxide media has not been studied or at least not reported in detail in the open literature.

This chapter deals with the synthesis of Ge-Al-MFI zeolites from concentrated alkaline mixtures containing less reactive reagents such as Ludox AS-40 and germanium oxide in the presence of sodium hydroxide. Extensive characterization is performed to

[*] Reproduced with permission from Ghosh, A., Garcia Vargas, N., Mitchell, S.F., Stevenson, S., Shantz, D.F. *The Journal of Physical Chemistry C* **2009**, 113, 12252-12259. Copyright © 2009 American Chemical Society.

assess the incorporation of the heteroatoms and the physicochemical properties of the final zeolites, and to describe how they are affected by mixture composition.

3.2 Experimental

Syntheses were performed to obtain of Ge-MFI, Al-MFI (ZSM-5), and Ge-Al-MFI (Ge-ZSM-5) samples. Ge-MFI samples were synthesized from mixtures of composition x SiO_2: y GeO_2: 0.27 NaOH: 0.21 TPAOH: 15 H_2O, where $x + y = 1$; and x/y = 10, 25 and 50. Al-MFI samples were synthesized from mixtures of composition x SiO_2: z $NaAlO_2$: 0.27 NaOH: 0.21 TPAOH: 15 H_2O, where $x + z = 1$; and x/z = 50 and 100. Ge-Al-MFI samples were synthesized from mixtures of composition x SiO_2: y GeO_2: z $NaAlO_2$: 0.27 NaOH: 0.21 TPAOH: 15 H_2O, where $x + y + z = 1$; x/y = 10, 25 and 50; and x/z = 50 and 100 for each x/y. Details of synthesis protocols and analytical methods are given in chapter II.

3.3 Results and discussion

3.3.1 pH considerations

Figure 3.1 shows the pH of a synthesis gel used to prepare a Ge-Al-MFI zeolite (measured 10 minutes after AcOH addition) as a function of the acetic acid to silica ratio. As the acetic acid content increases, the pH decreases as expected. Since Al-MFI zeolites readily form above a pH value of 8.5 (below this pH value it is more difficult to synthesize crystalline Al-MFI materials), the discussion below will focus on samples

made with an acetic acid to silica ratio in the synthesis mixture of AcOH/Si = 0.375 (pH range between 8 to 11).

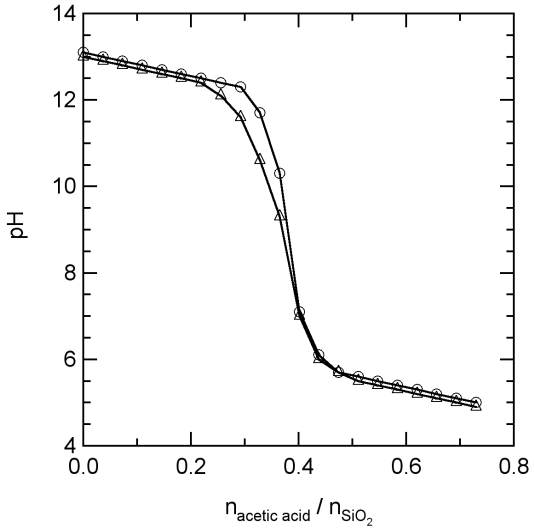

Figure 3.1 pH of a synthesis mixture (Si/Ge = 10, Si/Al = 50) as a function of molar acetic acid/silica ratio. Acetic acid was added as a 33 wt% solution. Two experimental measurements are shown.

3.3.2 Basic phase characterization

Figure 3.2 compares the powder X-ray diffraction (PXRD) patterns of silicalite-1 and MFI zeolites made with Al, Ge and Al/Ge in their calcined form. Based on the PXRD results, all materials have the expected MFI structure with no observable amorphous or crystalline impurities. The lattice constants are relatively insensitive to the zeolite composition, which is consistent with the low heteroatom content in the materials.

Thermogravimetric experiments on as-made materials revealed a weight loss between 12 – 13% due to decomposition of TPA, consistent with approximately four TPA cations per unit cell.

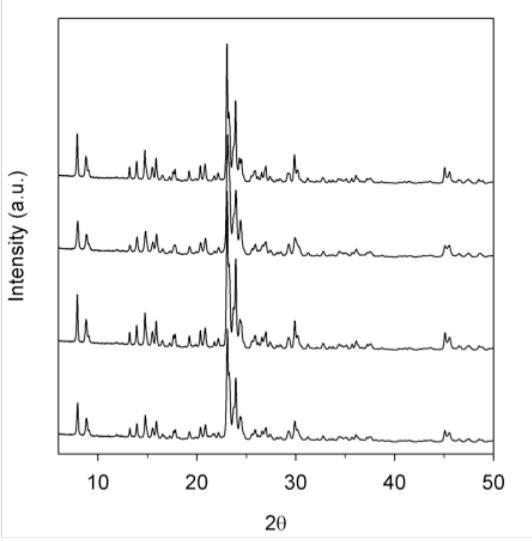

Figure 3.2 PXRD patterns of calcined (from top to bottom) silicalite-1, Al-MFI, Ge-MFI and Ge-Al-MFI.

Figure 3.3 shows representative FE-SEM images of a Ge-MFI and a Ge-Al-MFI sample. The crystals of both samples possess the typical twinned, coffin-type morphology observed for MFI materials and are relatively large (10 – 30 μm). It was generally observed in samples containing Ge and Ge/Al that the particle size tends to increase at lower pH values. The FE-SEM images clearly show the presence of an impurity located on the particles surface. The impurity is suspected to be germanium-rich since it is not observed in materials made in the absence of germanium. Ion-exchange experiments with $NaNO_3$ solutions were done to attempt the removal of the impurity.

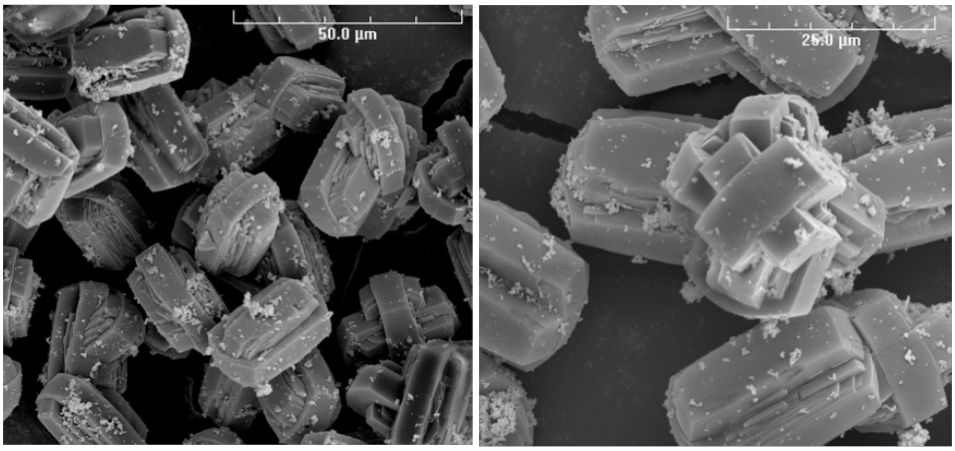

Figure 3.3 FE-SEM images of calcined Ge-MFI (left) and calcined Ge-Al-MFI (right), made with gel Si/Ge = 10 and Si/Ge = 10, Si/Al = 50 respectively.

Figure 3.4 shows FE-SEM images of Ge-MFI and Ge-Al-MFI samples after the ion-exchange process. The images show that the $NaNO_3$ treatment successfully removes the impurity. The chemical nature of the impurity will be discussed in more detail below.

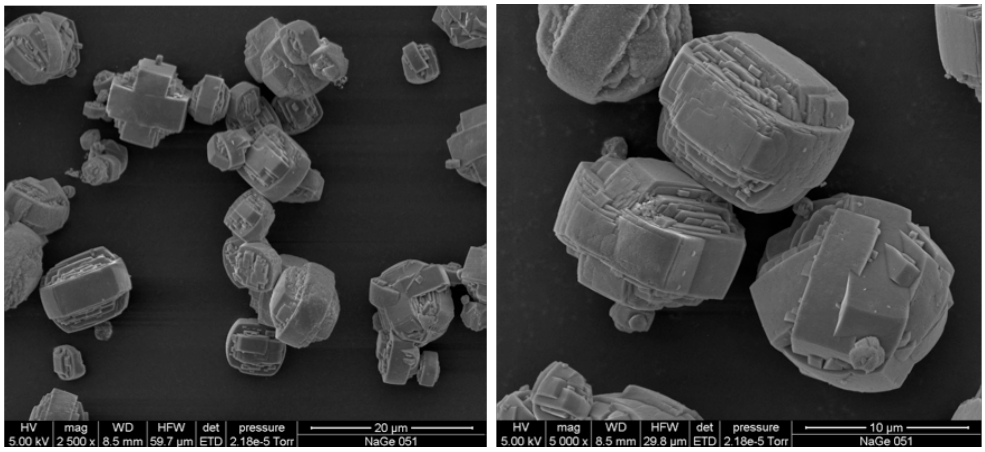

Figure 3.4 FE-SEM images of calcined Ge-MFI (left) and calcined Ge-Al-MFI (right), made with gel Si/Ge = 10 and Si/Ge = 10, Si/Al = 50 respectively after treatment with $NaNO_3$ solutions.

Figure 3.5 shows the nitrogen adsorption isotherms of a Ge-ZSM-5 sample (gel Si/Ge = 10, Si/Al = 50) before and after ion exchange. The micropore volumes, determined by the α_s-method, are found to be 0.082 and 0.149 cm^3/g, respectively. These results indicate that the samples have less accessible microporosity before ion exchange. One possible reason for the decreased porosity is the germanium-rich surface impurity, which is not observed in the PXRD results but is apparent from the SEM data. It is also possible that residual species are occluded in the micropores before ion exchange. Based on the information at hand we cannot rule out one possibility over the other. The significant reduction in the accessibility of the micropore volume before ion exchange would likely lead to deleterious effects in catalysis.

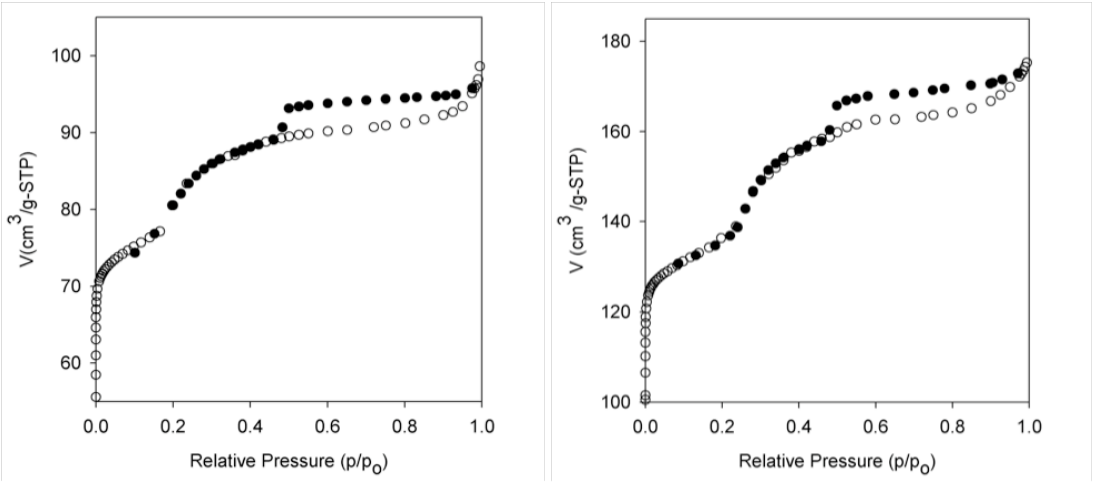

Figure 3.5 Nitrogen adsorption isotherms of Ge-Al-MFI before (left) and after (right) ion exchange. Open and closed circles denote adsorption and desorption loops respectively.

The Ge-MFI and Ge-Al-MFI materials are highly crystalline but seem to have a small amount of impurity not detected by PXRD but evident from FE-SEM and nitrogen

adsorption. The impurity is likely germanium-rich since it is only observed in materials made with germanium. It is possible that under alkaline conditions, other germanium oxide species form. In order to study the nature of the impurity and if any germanium and aluminum is being incorporated in the zeolites characterization with XRF and XPS was performed.

3.3.3 Bulk and surface composition

XRF and XPS were used to analyze the respective bulk and surface composition before and after ion exchange. Table 3.1 shows the results of this characterization. The synthesis mixture values are also listed for comparison. The table shows that the Si/Al in the final samples determined by XRF corresponds well with that of the mixture. This indicates that the aluminum uptake is close to 100% in all samples and not affected by the presence of germanium. The aluminum content was also found to be unaffected by the ion exchange process (data not shown). The XRF Si/Al ratios after the ion exchange were, within experimental error, the same to those before the exchange. Aluminum was only detected by XPS in those samples with bulk Si/Al ratios of 10, indicating that aluminum is not generally found in the surface of the materials unless the concentration is very high.

Table 3.1 Bulk (XRF) and surface (XPS) germanium and aluminum content in zeolites.

Si/Ge mixture	Si/Al mixture	Si/Al, XRF before IE	Si/Ge, XRF before IE	Si/Ge, XRF after IE	Si/Ge, XPS before IE	Si/Ge, XPS after IE
10	50	51.0	16.0	21.4	2.5	13.2
25	50	49.5	34.4	59.9	9.6	23.5
50	50	51.4	152.3	152.5	135.1	239.2
10	∞	∞	12.1	23.1	3.0	22.0
25	∞	∞	30.4	34.6	10.8	42.9
50	∞	∞	70.3	72.6	61.3	177.9
10	100	95.9	15.2	24.3	2.9	23.4
25	100	102.2	40.2	44.9	11.8	34.8
50	100	99.2	100.7	105.9	68.1	140.1

Germanium uptake, on the other hand, varies with the germanium and aluminum content in the gel and also with the ion exchange process. It can be seen in the table that the Si/Ge ratios in the final product determined by XRF do not correspond to those of the gels, indicating that not all germanium goes into the zeolites. In addition, it can be seen that for a given germanium content in the gel, the XRF Si/Ge ratio of the final samples depends on the amount of aluminum used. This indicates that the presence of aluminum affects the incorporation of germanium. In order to see how the germanium and aluminum content (and also the ion exchange process) affect the incorporation of germanium, the percent uptake of germanium (germanium in product/germanium in gel %) was calculated and plotted versus germanium and aluminum content for samples before and after ion exchange. Figure 3.6 shows the percent uptake of germanium as a function of germanium content in the gel. The first observation is that germanium uptakes are lower after the ion exchange process (left versus right figures), indicating that the ion exchange process removes a considerable amount of germanium from the samples (most likely germanium present as the impurity). The reduction is more

pronounced for samples containing increasing amounts of germanium. This could indicate that as more germanium is used, a larger percent becomes a part of the surface impurity.

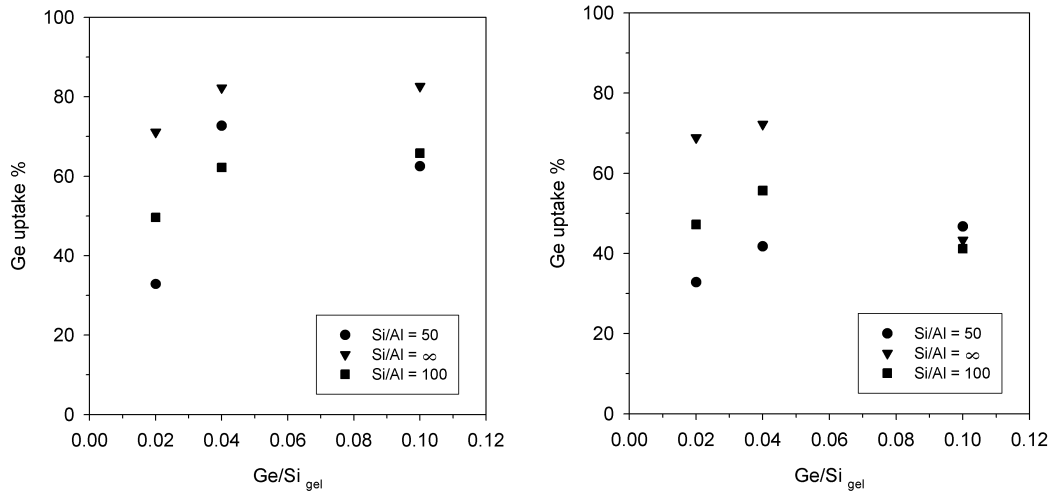

Figure 3.6 Percent uptake of germanium as a function of germanium content in the gels for Ge-Al-MFI samples before (left) and after (right) ion exchange.

The second observation is that the germanium content in the gel has an effect on the uptake. For a given aluminum content, germanium uptake seems to initially increase with germanium content (up to Ge/Si = 0.04) and then either level off or decrease. The third observation is related to the effect of aluminum. The uptake of germanium clearly decreases with increasing aluminum content in the samples. This is better observed for the samples after ion exchange (figure on the right). For the lower germanium contents, the uptakes continuously decrease with aluminum. When no aluminum is used, the uptakes are generally around 70%, but they decrease to 35 – 40% when the highest amount of aluminum is used. Aluminum does not seem to have much of an effect on the

samples made with the largest amount of germanium (Ge/Si = 0.1). In that case germanium uptakes are between 41-46%. The effect of aluminum is also represented in Figure 3.7.

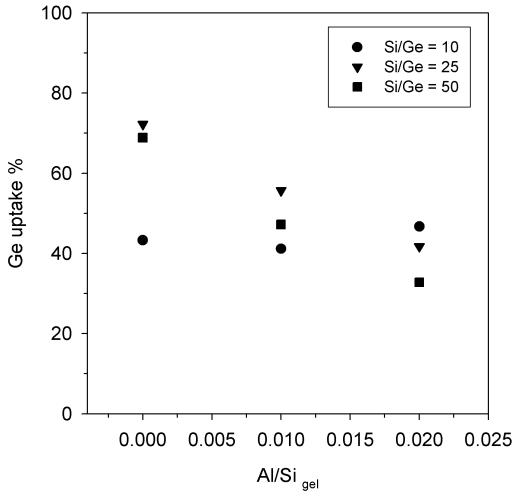

Figure 3.7 Percent uptake of germanium as a function of aluminum content in the gels for Ge-Al-MFI samples after ion exchange.

An interesting observation is made when considering the Si/Ge ratios determined by XPS (surface composition). It can be seen in Table 3.1 that the surface Si/Ge in samples before ion exchange is considerably lower than the bulk, indicating that there is enrichment of germanium on the surface. However, it can also be seen that after the ion exchange process, the surface Si/Ge increases and is in better agreement with the bulk Si/Ge ratios. This is in agreement with the view that the surface impurity observed in the surface of the materials before ion exchange is germanium rich, and it is effectively removed with the ion exchange treatment.

Note that no germanium oxide/sodium germanate phases were observed in the PXRD patterns. The detailed nature of the surface phases (e.g. crystallinity) is unclear. Attempts to analyze the samples with STEM were unsuccessful; however the SEM images along with the XPS data above show that the ion exchange removes the surface impurity, suggesting that the phase is likely amorphous.

Field Emission Scanning Electron Microscopy (FE-SEM) with EDS was used to try and ascertain the heteroatom profile in the crystals. Figure 3.8 shows EDS data consistent with the XRF/XPS results.

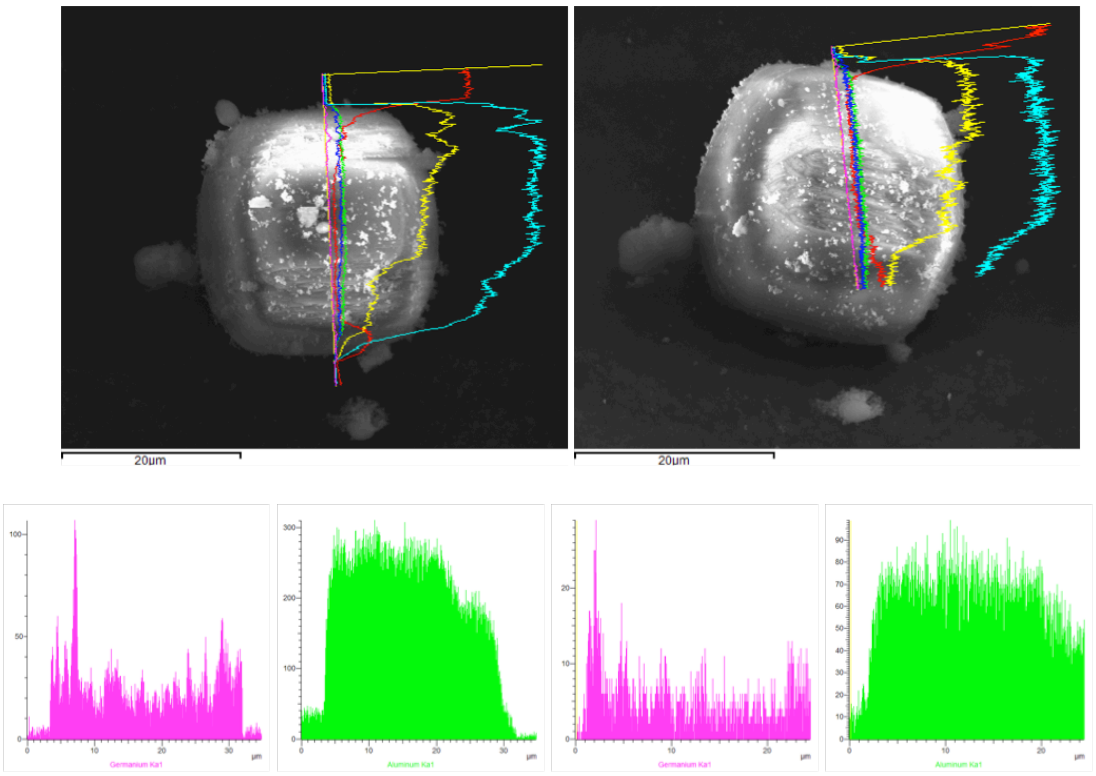

Figure 3.8 FE-SEM images of single crystals (top) and EDS results (bottom) showing the germanium (pink) and aluminum (green) concentration across the crystal.

There is more germanium at the outer surface of the crystal, and the aluminum distribution is uniform over most of the crystal surface but is depleted near the surface. Note that these samples have been ion exchanged, and thus the gradient detected and shown in Figure 3.8 are due to germanium and aluminum in the zeolite lattice.

3.3.4 Heteroatom coordination environment

Figure 3.9 shows the ^{27}Al MAS and ^{29}Si MAS NMR spectrum of the calcined Ge-Al-MFI sample prepared with Si/Ge = 10 and Si/Al = 50. A single resonance at 53 ppm in the ^{27}Al NMR is observed consistent with tetrahedral aluminum. The ^{29}Si MAS NMR spectrum of the calcined Ge-Al-MFI has mainly Q^4 groups at -113 ppm attributed to $Si[0Si]_4$ groups. This is consistent with the relatively low loading of germanium found in these materials.

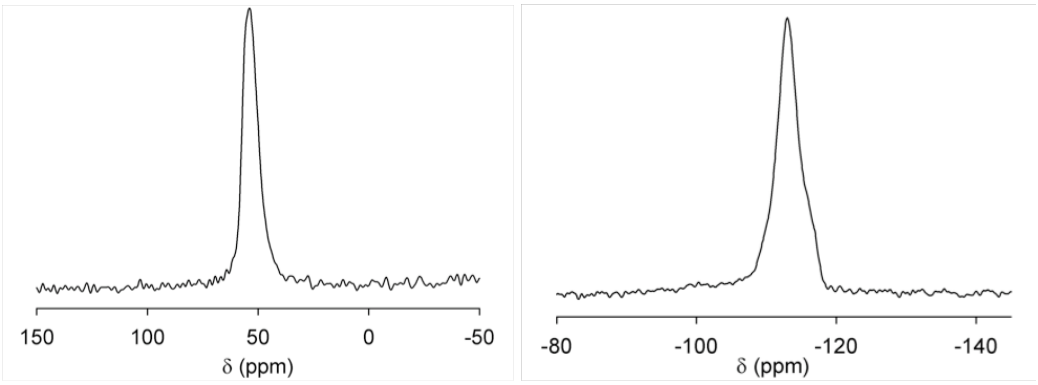

Figure 3.9 ^{27}Al MAS NMR (left) and ^{29}Si MAS NMR (right) of Ge-Al-MFI with a target composition of Si/Ge = 10 and Si/Al = 50.

All the information given so far describes the formation of the zeolites and some of their characteristics, but it does not provide any information about the coordination

environment of the germanium. To show that the germanium is indeed in the framework, X-ray absorption spectroscopy (XAS) was used. Figure 3.10 shows the XANES data of a reference GeO_2 sample and three Ge-MFI samples. The trend in the peak intensity can be interpreted as due to the change in the unoccupied p-density of states in germanium, since the peak is due to the 1s-4p transition. The peak intensity qualitatively correlates with the density of unoccupied states. Thus, the changes are due to the charge transfer between germanium and oxygen. It is not clear whether it has to do with an aluminum effect, a germanium concentration effect, or the presence of a GeO_2 impurity. However it should be noted the samples shown in Figure 3.10 have been ion exchanged, and thus, it is highly unlikely that an impurity GeO_2 phase is present.

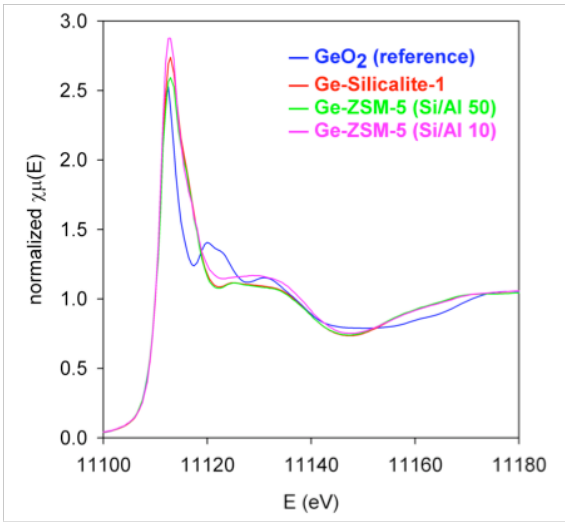

Figure 3.10 X-ray absorption near edge spectra of reference GeO_2, Ge-Silicalite-1 and Ge-ZSM-5 samples having Si/Al 50 and Si/Al 10, respectively.

Figure 3.11 shows the k^2-weighted EXAFS data of the samples shown in Figure 3.10. This data indicates that there is no obvious mixture of GeO_2 in the sample.

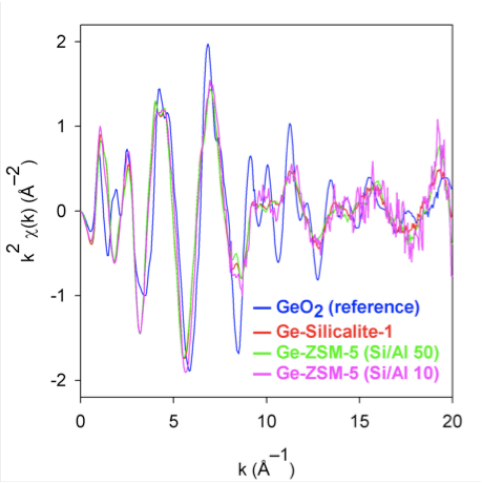

Figure 3.11 k^2 weighted EXAFS data of standard GeO_2, Ge-MFI and Ge-Al-MFI samples having Si/Al = 50 and Si/Al = 10, respectively.

In the Fourier transform magnitudes of k^2-weighted EXAFS in the samples and the reference GeO_2 (Figure 3.12), the difference in intensity between GeO_2, Ge-MFI and Ge-Al-MFI (Si/Al=50) is consistent with germanium substituting tetrahedrally for silicon in zeolite framework and thus having four Ge-O bonds. In the GeO_2 structure, there are six Ge-O bonds, which is why the signal in the first shell in GeO_2 is much stronger than in the zeolites, due to the coordination number effect. In the Ge-Al-MFI (Si/Al = 10) sample, the peak intensity is larger than in other zeolites. One possible explanation for this is that the Ge-O bond is the strongest in that sample compared to other zeolites. This would make the σ^2 the smallest for this sample and thus the peak intensity is the greatest. That model correlates with the XANES measurements that show charge transfer between germanium and oxygen in this sample is the strongest.

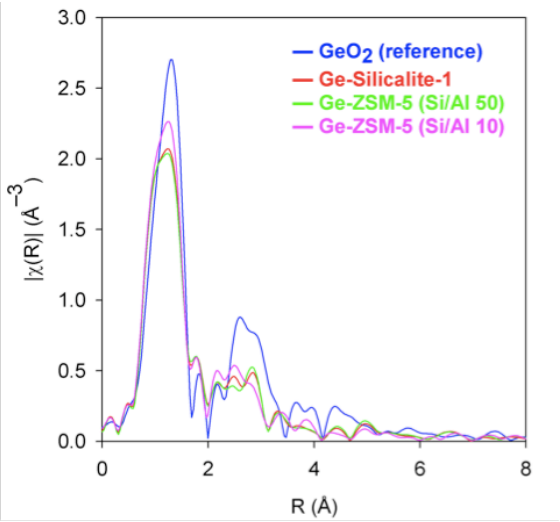

Figure 3.12 Fourier transform magnitudes of k^2-weighted EXAFS of reference GeO_2, Ge-MFI and Ge-Al-MFI samples having Si/Al=50 and Si/Al=10, respectively.

3.3.5 Surface impurity formation

The results shown above indicate that part of the germanium present in the zeolites forms a residual germanium-rich surface impurity that is removed during the ion exchange process. It is noteworthy to point out that rinsing with deionized water does not lead to removal of this overlayer. We currently believe that this overlayer is removed due to the mildly acidic nature (pH = 4 – 5) of the $NaNO_3$ solutions used in the ion exchanges. To try and understand in more detail the reason for this overlayer, two sets of experiments were performed. The first was to vary the synthesis period of a Ge-Al-MFI zeolite (Si/Ge = 10, Si/Al = 50) between 6 and 72 hours. These materials were analyzed by diffraction and XRF/XPS before and after ion exchange. The second was to determine the surface Si/Ge ratio as a function of the number of ion exchanges. The first set of experiments show that Ge-Al-MFI crystallizes rapidly, even after only six hours, and that the Si/Ge ratio of the as-made samples as determined by XPS (before

calcination and ion exchange) decreases with increasing heating time as can be seen in Figure 3.13. These results seem to indicate that the zeolite crystallizes rapidly, and that the aluminum is incorporated more rapidly than the germanium.

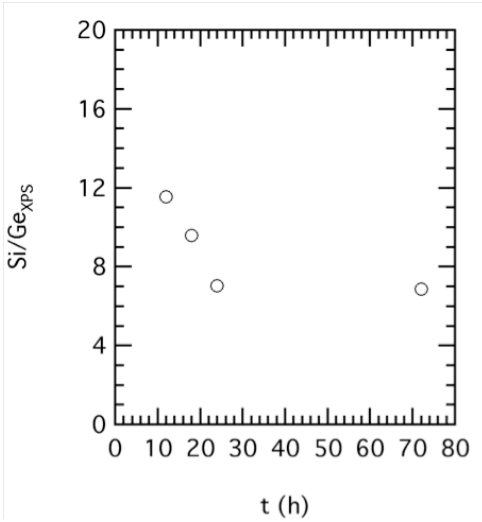

Figure 3.13 XPS Si/Ge ratio of as-made Ge-Al-MFI sample as a function of the heating (synthesis) time.

We believe this is due to a solubility effect of the germanium. In previous work employing clear solution syntheses at high pH, we observed that the presence of germanium enhances growth, but that as the pH increases, germanium incorporation decreases. In mixtures containing both aluminum and germanium, we observed that aluminum hindered growth and germanium enhanced growth, and that high aluminum and low germanium incorporation were observed. The results reported here are in line with those observations. However, here it is also observed that if the fully crystallized (by PXRD) zeolite mixture remains at elevated temperatures, germanium, likely in the form of sodium germanate based on XPS results, deposits on the surface of the

crystallized zeolite. The Si/Na ratio of these materials by XPS decreases from 17.9 for the sample heated for 12 hours to 14.0 for the sample heated for 72 hours.

The Si/Ge ratio at the surface (determined by XPS) was used to follow the presence of the surface impurity after several ion exchanges. This data is shown in Figure 3.14. It can be seen that the first ion exchange leads to a significant increase in the Si/Ge ratio as determined by XPS. Thus, the first ion exchange leads to the removal of the majority of the overlayer. On the basis of this data, it seems reasonable to speculate that the overlayer is amorphous, as one would not expect a polycrystalline solid to dissolve so rapidly. It is worth noting that the bulk XRF Si/Ge ratio for the sample shown in Figure 3.14 is 66 after three ion exchanges, whereas its Si/Ge ratio by XPS is 82. Thus the first exchange leads to a surface composition that is within 10% of the bulk composition.

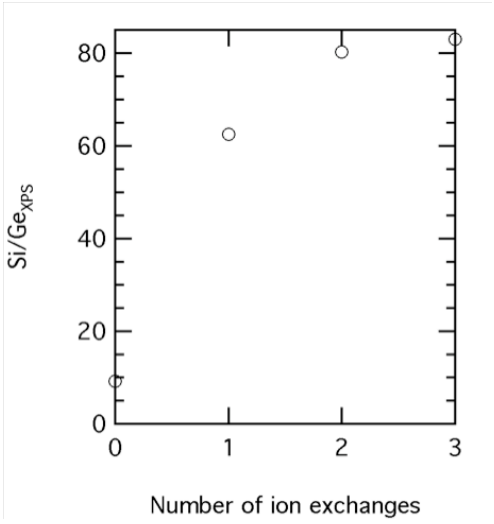

Figure 3.14 Surface Si/Ge determined by XPS as a function of the number of ion exchanges performed on a Ge-Al-MFI sample crystallized for 72 hours.

Thus we believe the picture that emerges is as follows. Ge-Al-MFI zeolites crystallize rapidly. XRF analysis of these samples indicates that nearly all of the aluminum is incorporated and that only a fraction (between 50-80%) of the germanium is incorporated. This would seem to indicate that aluminum is preferentially incorporated into the zeolite lattice as compared to germanium. Two simple explanations for this would be the solubility of germanium is different than aluminum, and that since germanium is larger than aluminum its uptake in the framework is more limited. There is a considerable enrichment of germanium on the outer surface, that increases with synthesis time (and depends also on germanium content), suggesting that residual germanium that did not enter the zeolite during crystallization, accumulates on the surface as an impurity. After ion exchange, it is observed that the Si/Al ratio is unchanged, while the surface and bulk germanium contents become closer in value (which typically indicates a germanium incorporation level of 30 – 50%).

3.4 Conclusions

A series of Ge-Al-MFI samples, made under industrially relevant conditions, have been synthesized and characterized using numerous analytical methods. The results highlight some of the challenges in preparing homogeneous samples containing multiple heteroatoms in alkaline media. A portion of the germanium present in the samples is found to form a surface germanium-rich impurity that can be effectively removed by treatment with sodium nitrate. While diffraction is insensitive to the surface germanium impurity, nitrogen adsorption and X-ray photoelectron spectroscopy are very

sensitive to its presence. Through a combination of control experiments, the formation of the impurity is attributed to the higher solubility of germanium in alkaline media than aluminum. This, coupled with the differences in the cation sizes (i.e. Al^{+3} versus Ge^{+4}), leads to aluminum being preferentially incorporated as compared to germanium. Given that the zeolites crystallize rapidly (less than six hours), longer heating durations lead to the slow precipitation of germanium species onto the surfaces of the zeolite crystals. Ge-Al-MFI zeolites that are treated with sodium nitrate do not exhibit the impurity and contain germanium and aluminum with incorporation efficiencies of 30 – 50% and ~100% respectively. X-ray absorption spectroscopy shows that the germanium present in those samples is tetrahedrally coordinated in the zeolite framework. EDS depth profiling coupled with FE-SEM shows that the aluminum content is uniform across the bulk of the crystal.

CHAPTER IV

SYNTHESIS AND CHARACTERIZATION OF MFI ZEOLITES WITH SIMULTANEOUS INCORPORATION OF BORON AND GERMANIUM[*]

4.1 Introduction

The incorporation of boron in MFI zeolites has been relatively well studied. As shown in chapter I, numerous investigations describing the synthesis of B-MFI zeolites using various silica and boron sources in hydroxide or fluoride media, and how different synthesis parameters (e.g. structure directing agent used, alkali cations, gel composition) affect the quality of the materials obtained are published. B-MFI zeolites are able to catalyze a number of reactions, including the Beckmann rearrangement of cyclohexanone oxime and the double bond shift isomerization of linear olefins. However, their use in many other acid catalyzed reactions has been limited because they exhibit lower acidity compared to Al-MFI zeolites due to the tendency of boron atoms to adopt a trigonal coordination in calcined zeolites. As was also shown in chapter I, incorporation of germanium in zeolites can potentially improve their catalytic behavior in some reactions due to the intrinsic structural changes that occurs when germanium is part of the framework or the stabilization of a particular active center adjacent to germanium atoms. The synthesis of MFI zeolites with simultaneous isomorphous substitution of boron and germanium has not been previously reported, even though they

[*] Reproduced with permission from Garcia Vargas, N.; Stevenson, S.; Shantz, D.F. *Microporous and Mesoporous Materials*, submitted for publication. Copyright © 2012 Elsevier.

could potentially exhibit different catalytic behavior in some of the reactions mentioned above. This chapter deals with the synthesis of MFI zeolites containing boron and germanium simultaneously incorporated in the framework. A description of how heteroatom incorporation is affected by gel composition and pH as well as a detailed characterization of the materials is given.

4.2 Experimental

4.2.1 Syntheses with variable heteroatom content

Two sets of B-Ge-MFI were made in this case. The first set included TPAOH as the only SDA precursor to keep the gel pH above 13. The second set included a combination of TPAOH and TPABr to keep the gel pH below 12. Gels of compositions were SiO_2: *x* H_3BO_3: *y* GeO_2, 0.21 TPAOH: 15 H_2O and SiO_2: *x* H_3BO_3: *y* GeO_2, 0.04 TPAOH: 0.17 TPABr: 15 H_2O respectively. In both cases, the molar Si/(B+Ge) ratio was 100, 75, 50, 25 and 10, with molar B/Ge = 1.

4.2.2 Syntheses with constant heteroatom content

A set of B-Ge-MFI was made in this case with constant boron and germanium contents but variable TPAOH/TPABr (variable pH). Gels composition were SiO_2: 0.01 H_3BO_3: 0.01 GeO_2, *z* TPAOH: *w* TPABr: 15 H_2O, with molar TPA/Si ratio equal to 0.21 and TPABr/TPAOH molar ratios of 0, 0.4, 1.1, 2.5, 3.7 and 7.4. The initial pH of the gels was 13.22, 13.17, 12.99, 12.44, 11.72 and 10.40 respectively. Details of synthesis protocols and analytical methods are given in chapter II.

4.3 Results and discussion

A summary of selected synthesis conditions and properties of the B-Ge-MFI zeolites made are shown in Table 4.1. It can be seen that the initial pH of the synthesis gels decreases with increasing boron and germanium content. The reason for the drop in pH is the increasing concentration of boric acid (boron source) in the gel. The drop in pH is more pronounced for gels containing TPAOH and TPABr (11.8 to 9.4) than for gels containing TPAOH only (13.3 to 13.1). This is to be expected because when TPAOH is used as the only SDA precursor, the concentration of OH^- is high enough to maintain the pH at high levels. However, once TPABr is introduced along TPAOH (maintaining the TPA/Si ratio), the OH^- concentration is at a level where any increase in acid concentration produces a significant pH change. The yield of solids from the syntheses is typically between 88 to 95%.

Table 4.1 Summary of selected synthesis parameters and properties of as-made zeolites.

Gel Si/(B+Ge)	Initial pH	Final pH	Yield %	Crystallinity %	Unit cell volume Å^3	Crystal size µm
TPA/Si = 0.21 and TPABr/TPAOH = 0						
100	13.26	11.85	94	98	5366.1	7.5
75	13.26	11.84	95	99	5364.2	8.5
50	13.22	11.81	92	99	5357.1	9
25	13.11	11.57	92	98	5346.8	12
10	13.06	11.00	88	100	5333.7	20
TPA/Si = 0.21 and TPABr/TPAOH = 4.25						
75	11.84	9.64	88	98	5363.6	40.5
50	11.43	9.74	93	98	5349.6	9.5
25	10.53	9.55	91	100	5328.3	16
10	9.38	9.01	91	99	5316.6	25

4.3.1 Structure and crystallinity

The structure and crystallinity of all the materials were assessed using powder X-ray diffraction (PXRD). Figure 4.1 shows the diffraction patterns of the as-made B-Ge-MFI samples made using TPAOH as the only SDA precursor (pH > 13). It can be seen that the materials have the expected MFI structure and no additional crystalline phases or impurities are observable. All the as-made samples exhibit orthorhombic symmetry.

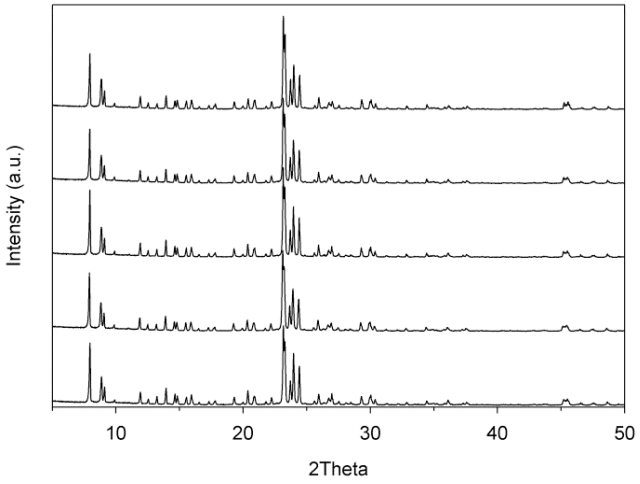

Figure 4.1 PXRD patterns of as-made B-Ge-MFI zeolites made at pH > 13. From bottom to top, gel Si/(B+Ge) = 100, 75, 50, 25 and 10. In all cases B/Ge = 1.

The PXRD patterns of the as-made B-Ge-MFI samples made at lower pH values (pH < 12) have the same characteristics and are shown in Figure 4.2. The crystallinity, obtained by comparing the intensity of the diffraction peaks of the as-made B-Ge-MFI zeolites with respect to a well-crystallized silicalite-1 sample, is shown in Table 4.1. All as-made B-Ge-MFI zeolites are highly crystalline regardless of the boron and germanium content and the pH of the synthesis gels.

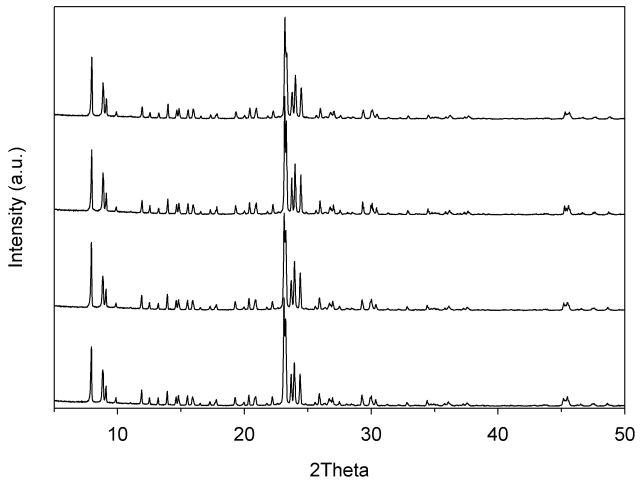

Figure 4.2 PXRD patterns of as-made B-Ge-MFI zeolites made at pH < 12. From bottom to top, gel Si/(B+Ge) = 75, 50, 25 and 10. In all cases B/Ge = 1.

Figure 4.3 shows the diffraction patterns of selected B-Ge-MFI samples after calcination in air. All B-Ge-MFI samples retain the MFI structure and high crystallinity after removal of the SDA. Upon calcination, all the B-Ge-MFI samples made can be refined using an orthorhombic unit cell, indicating that they retain the same symmetry observed in the as-made samples. This is contrary to the all-silica MFI sample (silicalite-1), which changes the unit cell symmetry from orthorhombic to monoclinic after calcination (diffraction peaks at $2\theta = 24.4°$ and 29.3° split in Figure 4.3). The retention of orthorhombic symmetry after calcination has been observed in other MFI zeolites containing boron, titanium, germanium and tin substituted in the framework and it is generally taken as evidence of heteroatom isomorphous substitution[102,119,141,142].

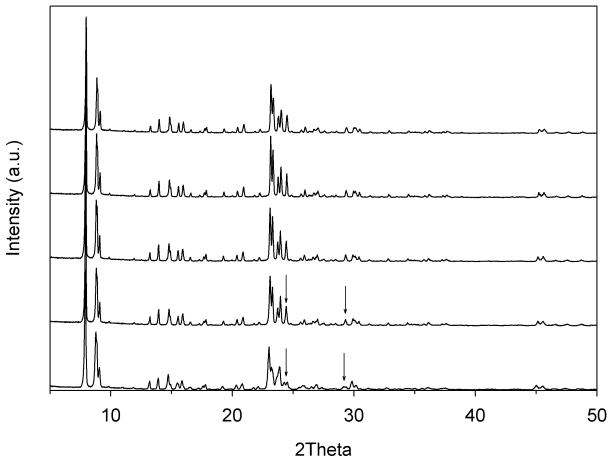

Figure 4.3 PXRD patterns of silicalite-1 and selected B-Ge-MFI zeolites in calcined form. From bottom to top: silicalite-1, B-Ge-MFI with Si/(B+Ge) = 100 made at pH > 13, and B-Ge-MFI with Si/(B+Ge) = 50, 25 and 10 made at pH < 12.

4.3.2 Chemical composition and heteroatom uptake

Germanium, silica and aluminium contents in all B-Ge-MFI zeolites were assessed using X-ray fluorescence spectroscopy (XRF). Boron contents were determined by inductively coupled plasma optical emission spectroscopy (ICP-OES). In all zeolites prepared, the aluminium content was between 0.01 – 0.03 wt% (100-300 ppm). Figures 4.4a and 4.4b show the Si/X (X = B, Ge) molar ratios of the zeolites prepared at high pH (>13) and low pH (<12) respectively. They are shown as a function of the Si/X molar ratios in the synthesis gels. It can be seen in Figure 4.4a and 4.4b that in both cases the germanium content in the zeolites increases with increasing germanium content in the synthesis gels. However, the Si/Ge ratios in the zeolites made at high pH value (>13) are in all cases considerably larger than the Si/Ge ratios in the gel (Figure 4.4a). This indicates that there is a small percent uptake of germanium from the solution at that pH level. The percent uptake (germanium in zeolite/germanium in gel %) for

those samples is shown in Figure 4.4c as a function of Si/Ge (and Si/B) in the gel. It can be seen that the percent uptake of germanium from the solution is approximately 37% and it does not vary with Si/Ge (and Si/B) content in the gel. A simple explanation for this is that the pH is controlling the uptake of germanium from the solution, i.e. it is partitioning between the zeolite product and solution species. The zeolites made at lower pH values (<12) have Si/Ge ratios equal to the Si/Ge ratios in the gel (Figure 4.4b), indicating that all the germanium added in the gels goes into the zeolites. Indeed, the percent uptake of germanium from the solution (Figure 4.4d) for samples made at pH < 12 is close to 100% and does not vary with the Si/Ge (and Si/B) ratio. It is clear that the percent uptake of germanium from solution is a function of the pH, and increases with decreasing pH values.

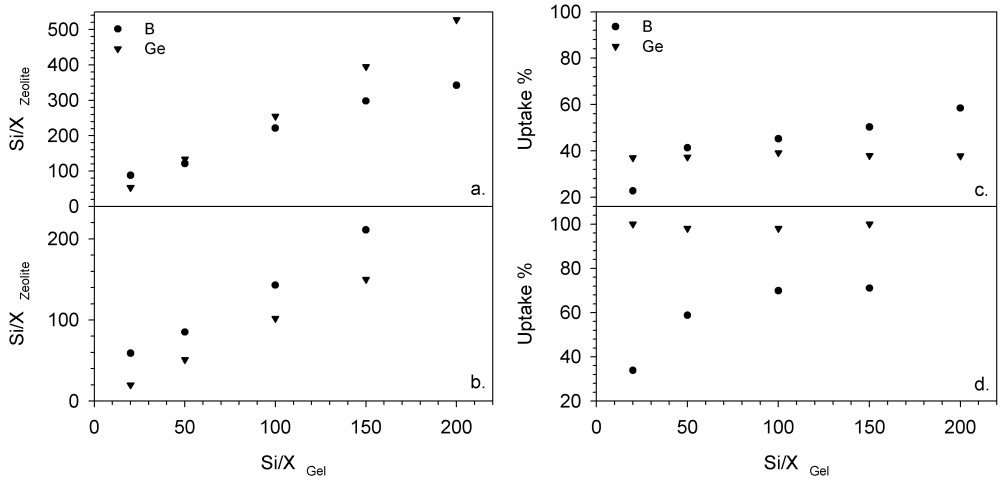

Figure 4.4 a. Si/B and Si/Ge molar ratios of as-made B-Ge-MFI made at pH > 13. b. Si/B and Si/Ge molar ratios of as-made B-Ge-MFI made at pH < 12. c. Percent uptake of boron and germanium from the gel for as-made B-Ge-MFI made at pH >13. d. Percent uptake of boron and germanium from the gel for as-made B-Ge-MFI made at pH < 12. All plots are as a function of Si/Ge (and Si/B) in the respective synthesis gel.

The behavior of boron is more complicated. For both sets of B-Ge-MFI zeolites made at high (>13) and low (<12) pH values, the boron content in the zeolite increases with increasing boron content in the synthesis gels (Figures 4.4a and 4.4b respectively). It can also be seen that the Si/B ratios in the zeolites are larger than the Si/B ratios in the gels, indicating that not all boron present in the gel goes into the zeolite. The percent uptake of boron from the solution for the zeolites made at high and low pH and its variation with Si/B (and Si/Ge) content in the gel can be seen in Figure 4.4c and 4.4d respectively. The percent uptake of boron from the gels is between 23% and 58% for samples made at pH > 13, and between 34% and 71% for samples made at pH < 12. In both cases, the percent uptake of boron decreases significantly with increasing heteroatom content, in contrast to germanium where the percent uptake remains constant with heteroatom content. This indicates that the percent uptake of boron from the solution is very sensitive to the boron content in the gels. In general, an increasing excess of boron is needed to achieve higher boron contents, which is in agreement with prior reports of boron-containing zeolites[125,143].

Since the pH and boron content in the synthesis gels are inversely related, one might think that the decrease in percent uptake of boron from the solution with increasing boron content is a consequence of the pH drop rather than the increasing boron concentration. In order to understand that, one can take a look at the samples made using TPAOH as the only SDA precursor (Figure 4.4c). In that case, when going from Si/B = 200 to Si/B = 20, the pH only goes from 13.3 to 13.1 (Table 4.1), which can be considered constant. For those samples, the percent uptake of boron from the

solution still decreases with increasing boron content (from 58% to 23%), indicating that pH is not the factor responsible for that decrease. In fact, as it will be shown below, the pH has the opposite effect.

The other possible factor that could be decreasing the uptake of boron from the solution is the increasing amounts of germanium with increasing boron contents used during the synthesis. However, we find that this is most likely not the case, since B-MFI samples made w/out germanium (in the same compositional and pH range) show the same behavior. The percent uptake of boron from the solution decreases with increasing boron content in the same way whether or not germanium is present. This is shown in Figure 4.5.

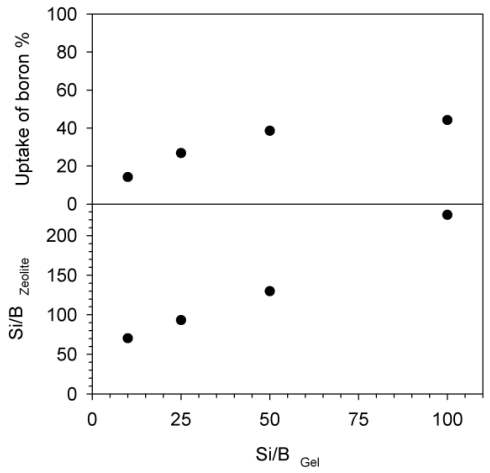

Figure 4.5 Percent uptake of boron from the gel (top) and Si/B molar ratios (bottom) for as-made B-MFI samples made without germanium at pH > 13.

X-ray photoelectron spectroscopy (XPS) studies were performed to determine the chemical composition of the zeolite outer surface. XPS studies revealed that there is surface depletion of boron and germanium in all samples. Only silica and oxygen were

detected to be present in the outer surface, indicating that boron and germanium are located in the bulk of the zeolites.

4.3.3 pH effect on heteroatom uptake

In order to study the pH effect in isolation, a series of B-Ge-MFI samples with constant boron and germanium content (Si/(B+Ge) = 50 and B/Ge = 1) were prepared at different pH values. The gel pH was adjusted by varying the TPABr/TPAOH ratios. Figure 4.6 shows the percent uptake of boron and germanium from the solution as a function of pH. It can be seen that lower pH values favor the incorporation of both boron and germanium in the zeolite. In the case of germanium, the percent uptake from the solution is always 95+% when the pH is 12 or lower. Once the pH is increased beyond that point, the percent uptake of germanium from the solution decreases rapidly and it goes as low as 30%when a pH > 13 is used.

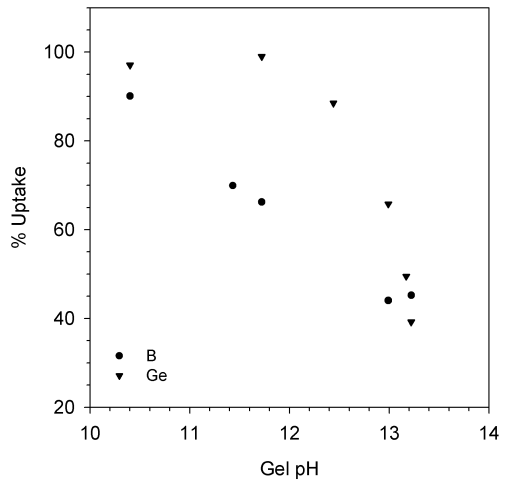

Figure 4.6 Percent uptake of heteroatoms from the solution in as-made B-Ge-MFI as a function of synthesis gel pH.

The percent uptake of boron from the solution increases linearly with decreasing pH (in the pH range studied). The percent uptake of boron varies from 45% to 90% when lowering the gel pH from 13.2 to 10.4 for this particular boron and germanium gel composition. This finding is in line with previous work by R. de Ruiter et al[128]. They showed that in aqueous boric acid/borate solutions, only $B(OH)_4^-$ species are found at pH > 11 at room temperature, but the concentration of $B(OH)_3$ species starts to increase at pH < 11 and becomes much larger with lower pH values. In general, the trend is that $B(OH)_3$ species are more stable at lower pH values. In addition, they also found that TPA cations stabilize $B(OH)_3$ species, and $B(OH)_3$ concentration can significantly increase with increasing TPA content at a given pH value (case studied was with pH ~ 11). Since $B(OH)_3$ are the units that are most likely to condense and form $B(OSi)_4$ in zeolites[128], higher boron uptakes at lower pH values for gels containing high concentrations of TPA cations can be understood.

So far, we have shown that one can increase the boron and germanium content in B-Ge-MFI zeolites by increasing the boron and germanium content in the synthesis gels. However, the uptake of germanium from the solution is primarily determined by the pH of the gel, while the percent uptake of boron from the solution is determined by the pH and the concentration of heteroatoms in the gel. It is worth mentioning that these statements are valid for the compositional range studied here and they might be little different for much higher heteroatom contents. The synthesis gels studied here have Si/Ge and Si/B contents from 200 to 20, leading to zeolites with 0.05 – 0.24 wt% boron, and 0.2 – 4.9 wt% germanium.

4.3.4 Framework composition

Boron incorporation leads to unit cell contraction due to the shorter B-O bond lengths (1.46 Å) compared to the Si-O bond lengths (1.61 Å). This contraction of the unit cell has been widely documented in the literature[119,125,127,143]. The unit cell contraction is taken as an indication that boron is isomorphically substituted in the zeolite framework. Figure 4.7 shows the unit cell volume of all B-Ge-MFI zeolites (made at high and low pH) as a function of the amount of boron atoms per unit cell. The amount of boron atoms per unit cell was calculated from the XRF and ICP compositional data for the zeolites, and taking the sum of Si, B and Ge atoms in a unit cell equal to 96. It can be seen that the unit cell volume of the B-Ge-MFI samples decreases with increasing boron content, indicating that boron is isomorphically substituted in the framework. The degree of contraction of the unit cell volumes reported in Figure 4.7 is in good agreement with reports of boron-containing MFI zeolites in the literature[119,127].

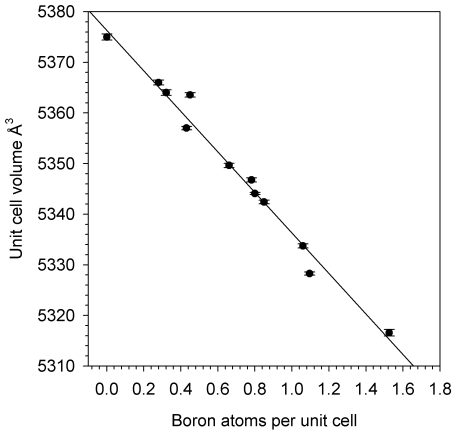

Figure 4.7 Unit cell volume of as-made B-Ge-MFI samples as a function of boron atoms per unit cell.

The incorporation of germanium in the framework of zeolites, on the other hand, leads to an increase on the unit cell volume as has been reported in the literature[98,101,102]. However, the change in unit cell volume when germanium is incorporated is not as large as would be expected for the larger size ion[101]. According to investigations reported in the literature for Ge-MFI zeolites, the changes in the unit cell volume of these type of zeolites become evident only in samples containing Si/Ge ratios of 11 or less[101]. The data in Figure 4.7 does not indicate that an increase in unit cell volume due to germanium incorporation is taking place, which is expected if one considers that the Si/Ge ratios used in this work are considerably higher than 11. The lowest Si/Ge ratio used in this case was 20. Additional evidence suggesting that germanium is incorporated in the framework is given by ^{11}B NMR studies and it is shown below.

4.3.5 ^{11}B nuclear magnetic resonance

^{11}B MAS NMR has been widely used to assess the framework incorporation and coordination environment of boron atoms in boron-containing zeolites. Figures 4.8a and 4.8b show the ^{11}B MAS NMR spectra of selected as-made B-Ge-MFI zeolites made at high (>13) and low (<12) pH values respectively. It can be seen in Figure 4.8 that the most intense resonance in all samples is found at approximately -4.1 ppm. This resonance has been attributed to framework boron tetrahedrally coordinated [$B(OSi)_4$ site][127,132,144]. The intensity of this resonance increases with decreasing Si/B ratio in the gels, indicating that increasing boron concentration in the gel leads to zeolites with increasing boron contents incorporated in the framework (something also evidenced by

chemical analysis). The intensity of the -4.1 ppm resonance, for samples made with comparable Si/B ratio in the gel, is larger when made at low pH values (Figure 4.8b) than at high pH values (Figure 4.8a). This indicates that there is higher uptake of boron from the solution (and incorporation in the framework) with decreasing pH. This is also in good agreement with what was concluded from the chemical analysis.

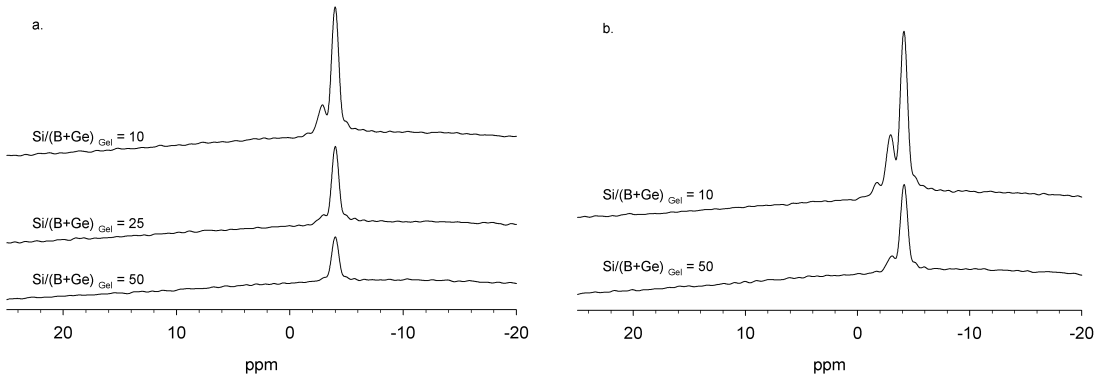

Figure 4.8 a. ^{11}B MAS NMR spectra of as-made B-Ge-MFI samples made at pH > 13. b. ^{11}B MAS NMR spectra of as-made B-Ge-MFI samples made at pH < 12. In all cases, gel B/Ge = 1. Chemical shifts are referenced to $BF_3 \cdot Oet_2$.

A second resonance at -2.9 ppm starts to develop in samples with increasing germanium and boron content (samples with Si/B < 121 and Si/Ge < 134 in final solid). This resonance is likely to correspond to tetrahedral framework boron with a different coordination environment, since it has been shown in the literature that the resonance for tetrahedral framework boron in zeolites can vary from -1.3 ppm to -4.5 ppm depending on the type of zeolite structure and the nature of the coordination environment[145-148]. Two possible assignments for this peak could be boron with three silicon and one germanium atom as nearest neighbors [$(GeO)B(OSi)_3$], or $B(OSi)_4$ sites in different

crystallographic positions. The absence of a resonance at -2.9 ppm in B-MFI samples made without germanium allows us to exclude the latter (Figure 4.9). The fact that this resonance is not visible for B-MFI samples with similar or higher boron contents and that the intensity of the resonance at -2.9 ppm increases with increasing germanium content in the zeolites, suggests that it most likely corresponds to boron atoms with three silicons and one germanium as nearest neighbors.

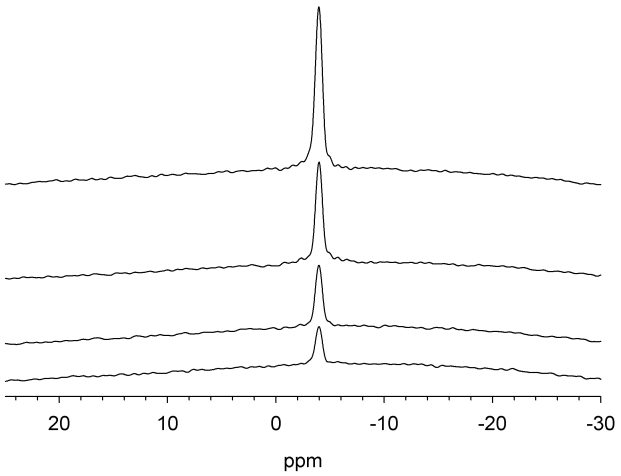

Figure 4.9 ^{11}B MAS NMR spectra of as-made B-MFI samples made without germanium at pH > 13. From bottom to top, the Si/B in the final zeolite is 226.2, 130, 93.2 and 70.4.

This type of site has not been seen in MFI zeolites since B-Ge-MFI has not been reported in the open literature. However, a recent paper on the incorporation of boron in a germanosilicate zeolite with UTL structure reported splitting (in four) of the tetrahedral framework boron resonance as well[149]. Two of the resonances were assigned to boron in different crystallographic positions but with a completely silica environment. The other two resonances were assigned to $(GeO)B(OSi)_3$ sites. A third resonance at approximately -1.7 ppm is present in the spectra of the B-Ge-MFI sample with the

highest boron and germanium content made (Figure 4.8b). Chemical analysis for this sample reports Si/B = 34 and Si/Ge = 20. Again, this resonance could be associated with a $(GeO)B(OSi)_3$ site in a different crystallographic position or even with a $(GeO)_2B(OSi)_2$ site.

Figure 4.10 shows the ^{11}B MAS NMR spectra of B-Ge-MFI samples made at pH > 13 in as-made and calcined form. The resonance for tetrahedral framework boron with only silicon atoms as nearest neighbors shifts from -4.1 ppm to -3.7 ppm after calcination. The resonance assigned to tetrahedral framework boron with three silicons and one germanium atom as nearest neighbors also shifts from -2.9 ppm to -2.7 ppm. In addition, the intensity of the resonances decreases after the calcination treatment. This could indicate that a small amount of deboronation is occurring due to the thermal treatment, which is something that has been reported to happen in boron-containing MFI zeolites[150].

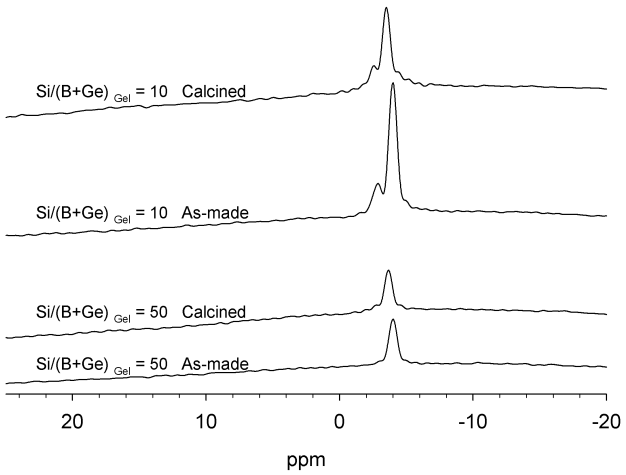

Figure 4.10 ^{11}B MAS NMR spectra of as-made and calcined B-Ge-MFI samples made at pH > 13. In all cases, gel B/Ge = 1. Chemical shifts are referenced to $BF_3 \cdot Oet_2$.

Framework boron in trigonal coordination is not observed in the ^{11}B MAS NMR spectra of the calcined B-Ge-MFI samples. It has been shown in the literature that framework boron reversibly changes from tetrahedral to trigonal coordination in calcined samples that are completely dehydrated and contain protons as the only charge balancing cations[123,146,151]. The chemical shift for framework boron trigonally coordinated is reported to be between 5 – 10 ppm with a strong quadrupolar interaction[131,151]. Since the calcined B-Ge-MFI samples were not dehydrated prior NMR characterization they are expected to have boron only in a tetrahedral coordination environment. Extra-framework boron species are not observed in the ^{11}B MAS NMR spectra of B-Ge-MFI samples either. This type of species has been reported to have a resonance between 15 – 18 ppm with strong quadrupolar interactions[132,150,151].

4.3.6 Crystal size and morphology

The size and morphology of all B-Ge-MFI samples were studied using field-emission scanning electron microscopy (FE-SEM). In general, all B-Ge-MFI samples have well-formed and uniform coffin-type crystals of relatively large sizes (7.5 to 40.5 μm). Figure 4.11 shows FE-SEM images of selected B-Ge-MFI zeolites made at high (>13) and low (<12) pH values. It can be seen that for a given heteroatom composition in the gel, samples made with lower pH values have crystals with larger sizes and more elongated in one direction.

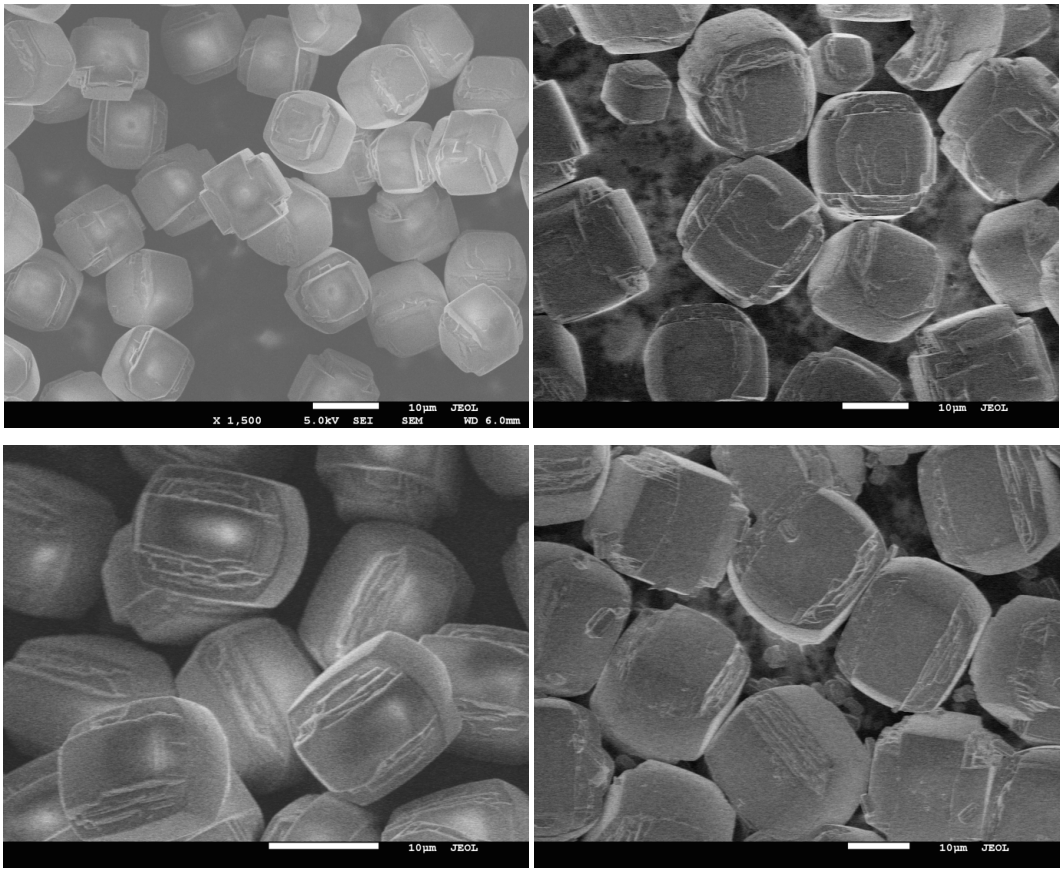

Figure 4.11 FE-SEM images of selected as-made B-Ge-MFI samples. Top images: B-Ge-MFI made at pH > 13 with gel Si/(B+Ge) = 25 (left) and 10 (right). Bottom images: B-Ge-MFI made at pH < 12 with gel Si/(B+Ge) = 25 (left) and 10 (right). The scale bar in all images is 10 μm.

The pH effect on the size and morphology of B-Ge-MFI samples is very evident when studying the B-Ge-MFI samples made at constant boron and germanium composition but variable pH values. FE-SEM images of these materials are shown in Figure 4.12. Decreasing the pH leads to larger and more rectangular coffin-type crystals.

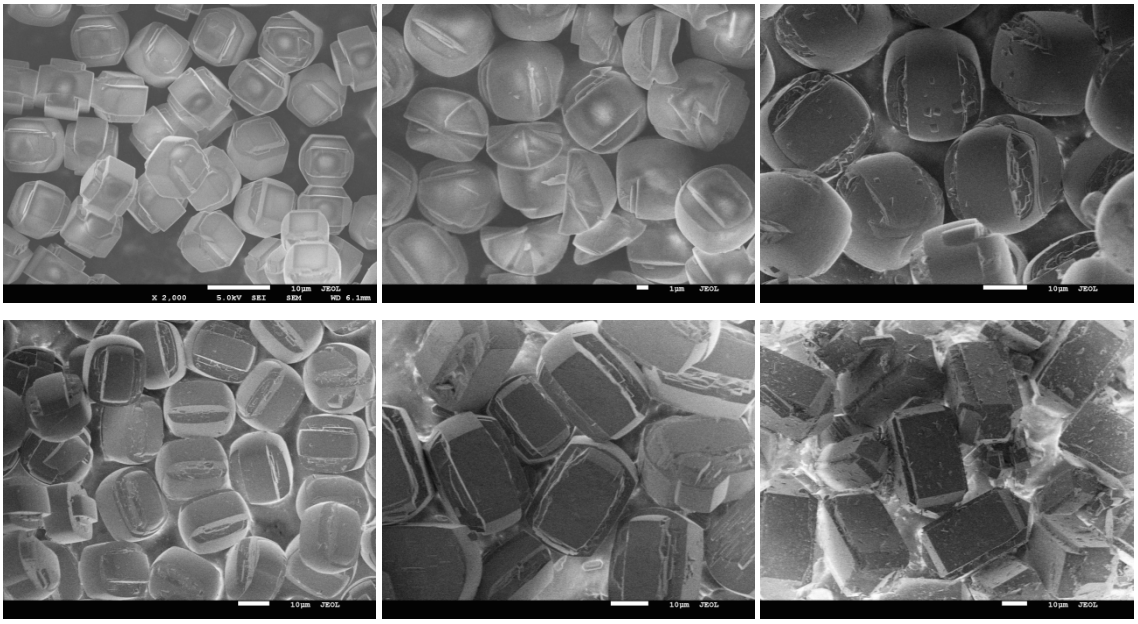

Figure 4.12 FE-SEM images of as-made B-Ge-MFI samples made with constant boron and germanium content but variable pH. From left to right, initial pH = 13.22, 13.17, 12.99, 12.44, 11.72 and 10.4.

4.3.7 Thermogravimetric analysis

Thermogravimetric analysis (TGA) was performed in order to determine the quantity and temperature of decomposition of the tetrapropylammonium cations present in the B-Ge-MFI zeolites. It is generally accepted that TPA cations present in zeolites can be found in different forms. They can be found as $SiO^{-}TPA^{+}$ ion pairs when TPA cations counterbalance the charge of siloxy groups present within the zeolite pores or on the external surface. They can also be found as lone TPA cations counterbalancing the negative charge created when trivalent atoms (Al^{+3}, B^{+3}) are substituted in the zeolite framework. The temperature of decomposition of the TPA cations has been reported to change depending on the state of the cations, and therefore, this parameter can be useful to gain insights about heteroatom substitution in the framework and framework defects.

In general, TPA cations associated with siloxy groups on the external surface are believed to decompose at lower temperatures than TPA cations associated with siloxy groups within the pore system. TPA cations associated with framework trivalent elements are believed to decompose at higher temperatures since they are bound by stronger interactions.

Figure 4.13 shows decomposition curves for B-Ge-MFI zeolites made at pH > 13 (Figure 4.13a) and pH < 12 (Figure 4.13b) with different heteroatom contents. For comparison purposes, the Si/B ratios in the zeolites selected are shown in the figure, as well as the decomposition curve for the all-silica MFI. The TG curve of the all-silica MFI sample exhibits three regions of weight loss. The first region corresponds to a weight loss of 0.68% (0.21 TPA cations) at temperatures below 320°C. This initial weight loss is assigned to TPA associated with siloxy groups on the outer surface of the zeolites. The second region corresponds to a weight loss of 11.09% (3.86 TPA cations) at temperatures between 320°C and 480°C, which is due to the decomposition of TPA associated with siloxy groups within the zeolite pore system. The last region corresponds to a weight loss of 1.62% at temperatures between 480°C and 760°C. This last weight loss is attributed to water lost during dehydroxylation of Si-OH groups. Figure 4.13 shows that TG curves for the B-Ge-MFI samples exhibit similar characteristics (three regions of weight loss) but the temperature at which the main weight loss occurs (decomposition of TPA within the pore system) increases significantly with increasing boron (and germanium) content.

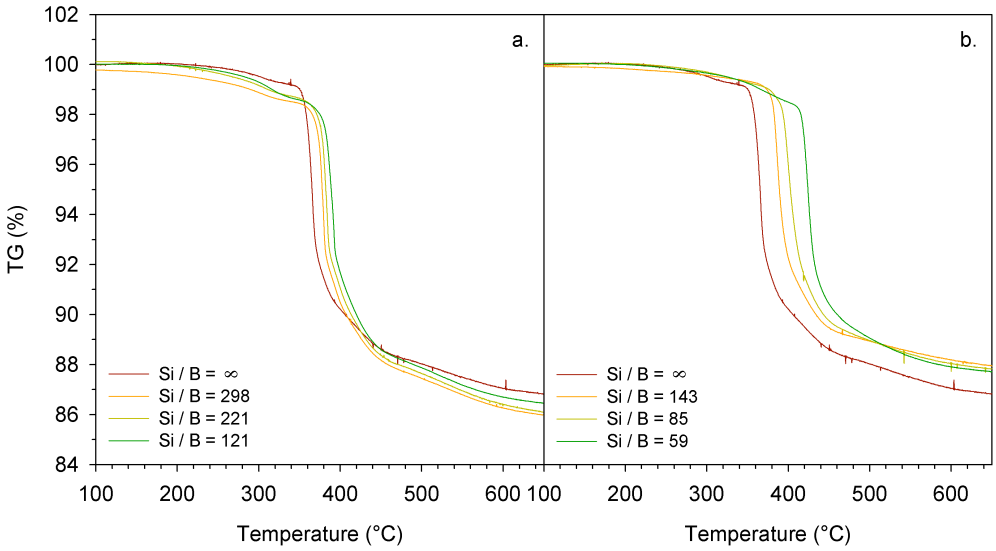

Figure 4.13 Thermogravimetric curves for selected B-Ge-MFI samples made at pH > 13 (a) and pH < 12 (b)

Table 4.2 shows the temperature of decomposition of TPA cations and the weight loss in each of the regions for all of the B-Ge-MFI samples. The continuous increase in the temperature of TPA decomposition in the pore system (T* in Table 4.2) indicates that TPA is more strongly attracted to frameworks with increasing boron contents and offers supporting evidence that the incorporation is taken place. It has been reported that TPA cations within the pore system of B-MFI zeolites (TPA cations in range II) decompose at two different temperatures, one for TPA associated with siloxy groups and another for TPA associated with framework boron sites[152,153]. In those reports, two peaks are observed in the DTA curves. In our case, only one feature is observed and all TPA cations within the zeolite seem to decompose at the same temperature, even though not all of them are associated with boron sites. It is possible that TPA molecules associated with siloxy groups still feel stronger electrostatic interactions with the framework

leading them to decompose at higher temperatures. This phenomenon combined with the possibility that they cannot easily diffuse out of the pores offers an explanation of why they seem to decompose at the same temperature as TPA cations associated with boron sites. In any case, the fact that the temperature of decomposition increases significantly with increasing boron content points to framework incorporation of boron.

Table 4.2 Thermogravimetric analysis of B-Ge-MFI samples.

B/ u.c.	Ge/ u.c.	Region I			Region II				Region III	
		T (°C)	Δ*m* (wt%)	TPA/ u.c	T (°C)	T* (°C)	Δ*m* (wt%)	TPA/ u.c	T (°C)	Δ*m* (wt%)
pH > 13										
0	0	< 320	0.68	0.21	320 – 480	365	11.09	3.86	> 480	1.62
0.28	0.18	< 331	1.23	0.39	331 – 491	376	11.12	3.87	> 491	1.98
0.32	0.24	< 333	1.23	0.39	333 – 493	378	11.01	3.83	> 493	2.03
0.43	0.37	< 337	1.37	0.43	337 – 497	382	11.07	3.85	> 497	2.04
0.78	0.71	< 345	1.39	0.44	345 – 505	390	10.81	3.75	> 505	1.67
1.05	1.73	< 360	1.77	0.56	360 – 520	405	10.81	3.75	> 520	1.51
pH < 12										
0.45	0.63	< 333	0.51	0.16	333 – 493	378	10.88	3.78	> 493	1.33
0.66	0.93	< 341	0.55	0.17	341 – 501	386	10.46	3.61	> 501	1.27
1.10	1.82	< 355	0.73	0.23	355 – 515	400	10.44	3.61	> 515	1.27
1.53	4.46	< 378	1.23	0.39	378 – 538	423	10.35	3.57	> 538	1.11

The presence of germanium, in contrast, does not seem to significantly affect the temperature of decomposition of TPA. B-MFI samples made without germanium show the same increase in temperature of decomposition with increasing boron content, indicating that the increase in temperature of decomposition seen in the B-Ge-MFI samples is not due to germanium. If anything, the presence of germanium seems to result in a minor decrease in the temperature of decomposition. When comparing samples containing very similar boron content (B/u.c. = 0.43 versus 0.45 and B/u.c. = 1.05 versus 1.10) but different germanium content (Ge/u.c. = 0.37 versus 0.63 and

Ge/u.c. = 1.73 versus 1.82) the temperature of decomposition is found to be 4 – 5°C lower in the samples containing more germanium.

Another observation from Figure 4.13 and Table 4.2 is related to the presence of defects in the zeolites. In range I, samples made at high pH lose more weight (1.23 – 1.77 wt%) than samples made at low pH values (0.51 – 1.23 wt%). The weight loss in that region is assigned to TPA cations associated with defect sites on the surface of the zeolites because they are known to decompose at lower temperatures. This suggests that samples made at higher pH values tend to have more defect sites on the outer surface and therefore more TPA cations are found there. In addition, the weight loss in region III is also larger for samples made at high pH. This also indicates that samples made at higher pH have more defect sites leading to larger water loss after dehydroxylation.

4.3.8 Acidity

The temperature-programmed desorption of ammonia (NH_3-TPA) profiles for selected B-MFI and B-Ge-MFI samples are shown in Figure 4.14. The amount of ammonia adsorbed increases with increasing boron content, indicating that increasing amounts of boron lead to higher number of acid sites. The temperature of maximum desorption of ammonia is generally taken as a qualitative indicative of the strength of the acid sites. This temperature ranges from 219°C to 254°C for the samples analyzed. Desorption of ammonia at that temperature range has been attributed to acid sites of medium strength. Similar findings have been reported for other boron-containing zeolites in the literature. The temperature of maximum ammonia desorption slightly

changes depending on the boron and germanium content in the samples analyzed. An interesting observation is that the B-MFI sample (containing boron and silica only) has a slightly lower temperature of maximum desorption compared to the B-Ge-MFI sample that has considerable lower boron content (black versus green profiles). The difference in temperature is about 5°C. This could indicate that the presence of germanium in boron-containing zeolites could result in a slight increase in the strength of the acid sites. The B-Ge-MFI sample made with the highest boron and germanium contents (red profile) has an even higher temperature of maximum desorption (254°C versus < 224°C for the other samples).

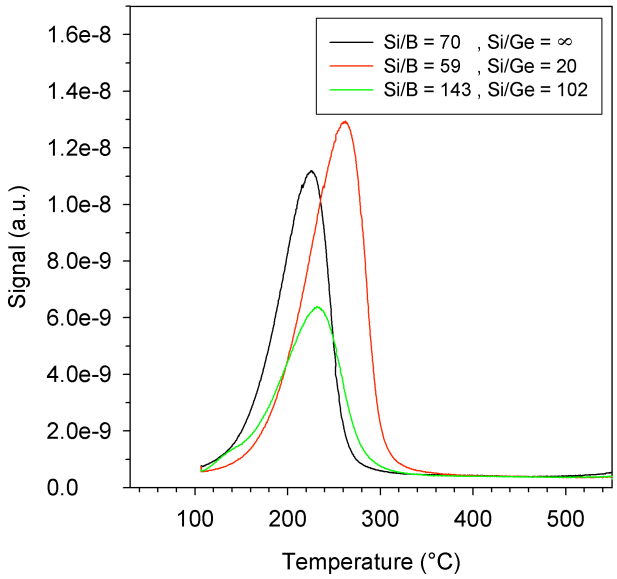

Figure 4.14 NH_3-TPD profiles of selected B-MFI and B-Ge-MFI samples.

4.4 Conclusions

Highly crystalline MFI zeolites containing both boron and germanium simultaneously incorporated in the framework were successfully synthesized and characterized. The framework incorporation of both heteroatoms is heavily influenced by synthesis pH. At pH values below 12, germanium uptake is found to be above 95% regardless of gel composition. Boron uptake is, in addition to pH, influenced by boron content in the gel. High uptake of boron is achieved when both parameters decrease. The successful framework incorporation of the heteroatoms and its impact on the properties of the zeolites was manifested in several ways. A linear decrease of the unit cell volume with boron content in the zeolite was observed. ^{11}B MAS NMR studies showed that boron was incorporated in the zeolite framework in a tetrahedral coordination, and the possible existence of sites comprised of boron atoms surrounded by three framework silicon atoms and one framework germanium atom as nearest neighbors along with boron sites with all-silica environment. Incorporation of increasing amounts of boron lead to a significant increase in the decomposition temperature of TPA due to their stronger attraction to the increasingly negatively charged framework. NH_3-TPD results suggested that incorporation of germanium could lead to a slight strengthening of the acid sites present in B-Ge-MFI samples although more investigations need to be done to confirm this.

CHAPTER V

SYNTHESIS AND CHARACTERIZATION OF SN-MFI ZEOLITES: SODIUM INHIBITS THE SYNTHESIS OF PHASE PURE MATERIALS[*]

5.1 Introduction

As mentioned in chapter I, tin-containing zeolites have attracted the attention of the catalysis community due their ability to catalyze a number of reactions involving carbonyl compounds and biomass-derived substrates with remarkable activities and selectivities. It is believed that tin-containing zeolites can act as Lewis acid catalysts and are therefore of high interest for non-traditional applications.

The incorporation of tin in MFI zeolites is important because of the unique catalytic features of the MFI structure and its commercial importance. Currently, there are only a few preparations describing the hydrothermal synthesis of Sn-MFI zeolites and they generally use tetraethyl orthosilicate (TEOS) as the silica source with gels free of alkali cations. Therefore, alternative preparations that include conditions that can be of more commercial interest (i.e. alternative silica sources, use of alkali cations and alkali hydroxides, low water content gels) are needed.

This chapter deals with the synthesis of Sn-MFI zeolites from highly alkaline and concentrated gels containing the less reactive Ludox AS-40. A detailed investigation of the effect of sodium ions in the synthesis of Sn-MFI zeolites is carried out by preparing the zeolites in the presence and absence of sodium from gels with different compositions

[*] Reproduced with permission from Garcia Vargas, N.; Stevenson, S.; Shantz, D.F. *Microporous and Mesoporous Materials* **2012**, *151*, 37-49. Copyright © 2012 Elsevier.

and pH values, and following out with extensive characterization to understand how the different synthesis parameters affect the physicochemical properties of the zeolites.

5.2 Experimental

5.2.1 Syntheses in the presence of sodium

Sn-MFI zeolites were made from gels of composition SiO_2: *x* $SnCl_4$: 0.21 TPAOH: 0.3 NaOH: 15 H_2O, with Si/Sn = 150, 100, 50, 25 and 15. In order to study the pH effect, three sets of samples were made from gels with an adjusted pH of 10.6, 12.0 and 13.2 respectively.

5.2.2 Syntheses in the absence of sodium

In this case, Sn-MFI zeolite were made from gels of composition SiO_2: *x* $SnCl_4$: *y* TPAOH: 15 H_2O, with Si/Sn = 150, 100, 75, 50 and 25. For Si/Sn ratios of 150 and 100, the molar TPAOH/Si ratio was 0.21 and for Si/Sn ratios of 75, 50 and 25, TPAOH/Si was 0.3, 0.4 and 0.9 respectively. In this case, the pH of the gels was always higher than 13.2. Details of synthesis protocols and analytical methods are given in chapter II.

The materials will be described in the results section using the following notation: Sn-MFI-*c*-*p*, where *c* is the Si/Sn molar ratio of the synthesis gel and *p* is the pH of the gel. Samples made in the absence of sodium hydroxide are denoted as Sn-MFI-*c*-*NS*, where *NS* denotes no sodium.

5.3 Results and discussion

The Sn-MFI zeolites synthesized were characterized using a battery of methods to ascertain how tin content, pH, and presence/absence of sodium ions in the synthesis gels impacted the properties of the materials formed. The results will be described below in the following sequence. First, the effect of tin content and synthesis pH will be discussed for samples made in the presence of sodium ions. These materials will be compared/contrasted in terms of their crystallinity/phase purity, composition, morphology and porosity. Second, the effect of sodium ions will be analyzed using a similar structure.

5.3.1 Syntheses in the presence of sodium

5.3.1.1 X-ray diffraction

Figure 5.1 shows the powder X-ray diffraction (PXRD) patterns of the as-made and calcined samples made with pH of 12 (i.e. the Sn-MFI-*c*-12 samples, where *c* is the silica to tin molar ratio). Based on PXRD, these materials have the MFI crystal structure expected and no crystalline impurities such as SnO_2 are observable. The crystallinity of the samples decreases at high tin contents (i.e. Si/Sn≤25) based on the lower intensity of the peaks and the absence of a flat base line in the 2θ region of 20 – 30°. The same trend was observed for the materials made at different pH values (i.e. pH of 10.6 and 13.2) as it is shown in Figure 5.2.

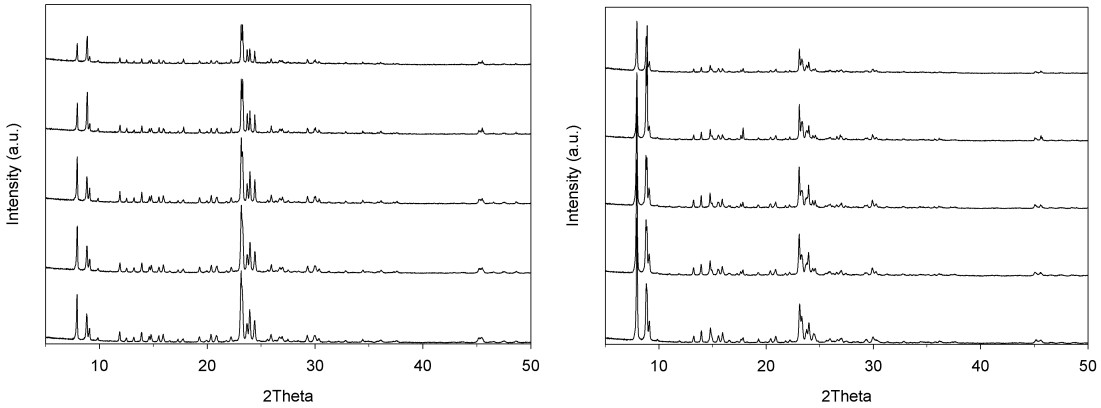

Figure 5.1 PXRD patterns of as-made (left) and calcined (right) Sn-MFI-*c*-12 samples, where from top to bottom c = 15, 25, 50, 100 and 150.

The only amorphous material obtained under the conditions used was Sn-MFI-15-10.6. Preferred orientation effects are also observed at high tin contents (i.e. Si/Sn ≤25) suggesting differences in the particle size and shape when different tin contents are used. All as-made Sn-MFI materials made in the presence of sodium ions could be indexed using an orthorhombic unit cell, while the same samples upon calcination appear to be best described by a monoclinic unit cell. This change in symmetry is also observed in silicalite-1 and in vanadium and titanium containing MFI zeolites when very low or no substitution of the heteroatoms is believed to occur[154].

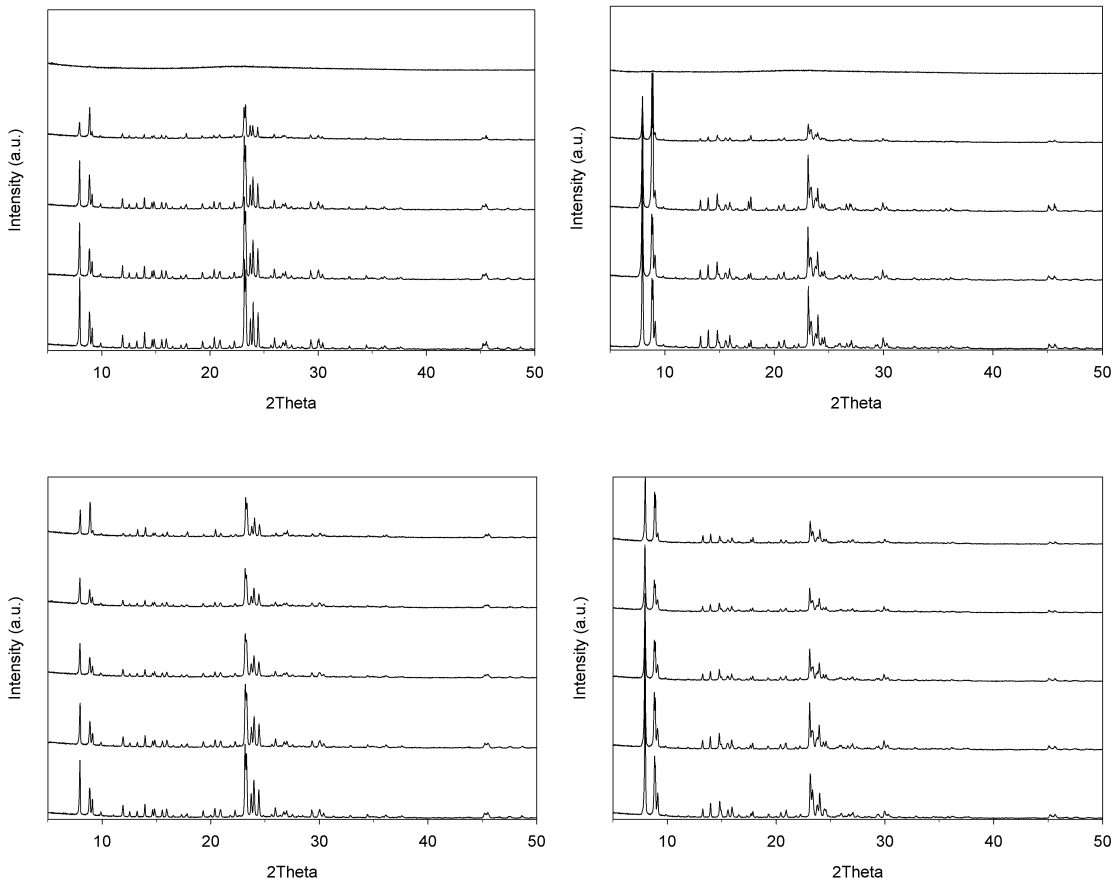

Figure 5.2 PXRD patterns of as-made (left) and calcined (right) Sn-MFI-*c*-10.6 (top) and Sn-MFI-*c*-13.2 (bottom) samples, where from top to bottom *c* = 15, 25, 50, 100 and 150.

A qualitative means of estimating the degree of tin incorporation in the framework of the zeolites is to compare the changes in the unit cell volume as a function of the tin content. The results of this analysis are shown graphically in Figure 5.3, and a summary of the numerical values is given in Table 5.1. As can be seen, the trends observed are pH dependent. In the case of the samples made with the highest pH, there is a consistent decrease in the unit cell volume as the tin content in the gel increases. For the materials made at pH of 12, a decrease in the unit cell volume with tin content is

observed for Si/Sn ratios of 50 and higher. The higher tin content materials in this series show either none or small increase in the unit cell volume compared to silicalite-1. Materials made at the lowest pH (i.e. 10.6) follow a similar trend. A smaller unit cell volume, compared with the pure silicalite-1, is observed up to a Si/Sn ratio of 100 and for the higher tin content samples very little change is observed.

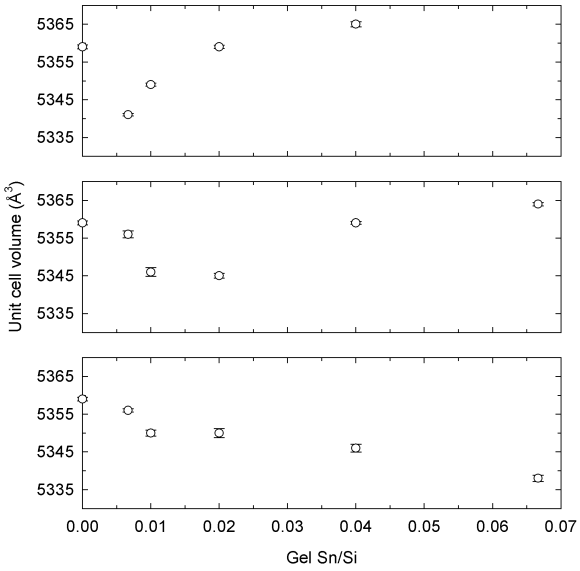

Figure 5.3 Unit cell volume of as-made Sn-MFI samples as a function of the gel Sn/Si ratio, where from top to bottom gel pH = 10.6, 12.0 and 13.2.

These results indicate that for the materials made at the highest pH content there is a rather unexpected contraction of the unit cell volume as the tin content increases. The same observation is true for the low tin content samples made at lower pH values, but in those cases the trends seen at high tin contents are not easily explainable and the additional characterization shown below is needed to rationalize the results. The fact that there is a contraction of the unit cell volume in most of the Sn-MFI samples is

counterintuitive. It is commonly accepted that substitution of Si^{+4} by larger ions in the framework of zeolites should lead to an expansion of the unit cell volume due to the larger bond lengths. This has been observed in titanium and vanadium-containing MFI[43,142,154]. In the case of tin-containing MFI zeolites there is one report in the literature in which an expansion of the unit cell as tin content increases was observed[55], but there is also one report in which the opposite trend was seen and there was a contraction in the unit cell volume[155]. Other works on tin-substituted MFI zeolites in the literature did not refer to changes in the unit cell volume[58,59,156]. It is clear that the unit cell volume is a function not only of Si-O/T-O bond lengths but also of Si-O-Si/Si-O-T bond angles and more in depth investigation is needed to rationalize the trends seen. In any case, the changes observed are less than 1%. This contraction of the unit cell upon tin uptake will be revisited for the syntheses performed without sodium (*vide infra*).

Table 5.1 Unit cell volume of as-made Sn-MFI materials given in cubic angstroms.

C	**Sn-MFI-*c*-10.6**	**Sn-MFI-*c*-12**	**Sn-MFI-*c*-13.2**
∞	5359 ± 0.502	5359 ± 0.502	5359 ± 0.502
100	5349 ± 0.372	5346 ± 1.162	5350 ± 0.815
75	-	-	-
50	5359 ± 0.418	5345 ± 0.642	5350 ± 1.212
25	5365 ± 0.683	5359 ± 0.367	5346 ± 1.014
15	Amorphous	5364 ± 0.452	5338 ± 0.839

5.3.1.2 FE-SEM

In addition to the unit cell volume and crystallinity, properties such as particle size/shape and phase purity vary significantly with the tin content and the pH of the synthesis gel. Figure 5.4 shows FE-SEM images of the Sn-MFI-*c*-12 samples as a

function of tin content in the gel. Increasing the tin content correlates with the appearance and increase of an additional phase on the surface of the zeolite particles and an increase in the particle size. A similar trend is also observed for the materials made at different pH (i.e. pH of 10.6 and 13.2) but the amount of additional phase formed is more pronounced at 10.6 and less pronounced at 13.2.

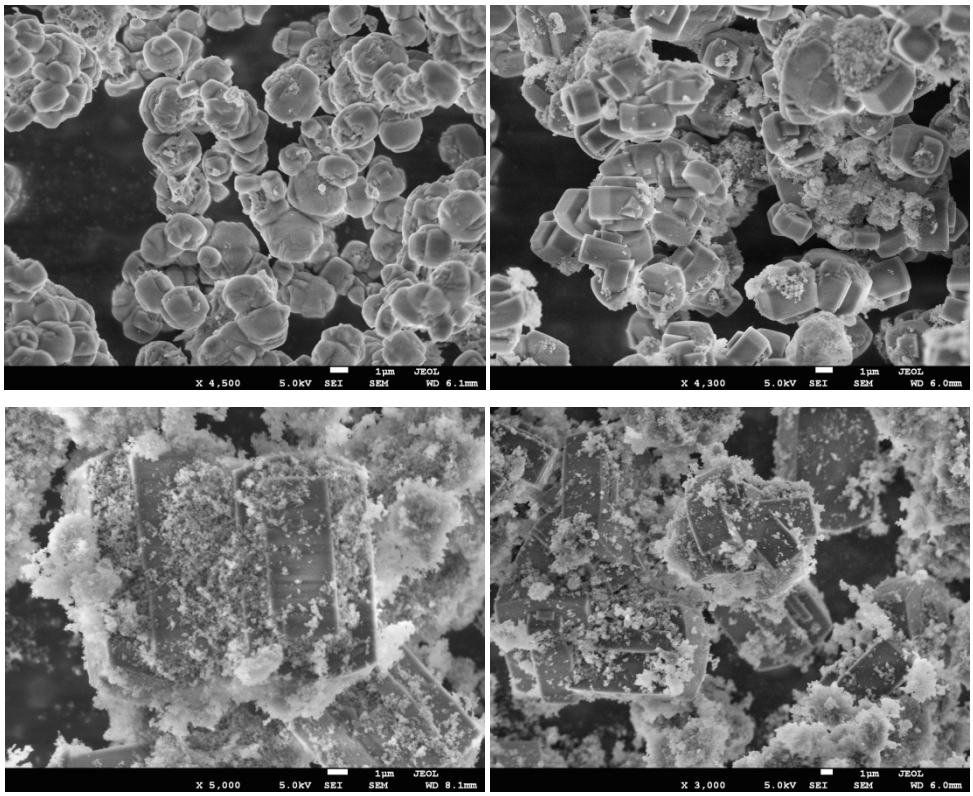

Figure 5.4 FE-SEM images of calcined Sn-MFI-*c*-12 samples, where clockwise from top left $c = 100, 50, 25$ and 15. The scale bar in all images is 1 μm.

These images correlate with the PXRD data that show a decrease in the crystallinity (and slight preferred orientation) for the samples made with very high tin contents (i.e. Si/Sn≤25). Given the absence of a second crystalline phase in the PXRD

spectra, it is tempting to assume that the additional phase (particulates on the surface of the zeolite crystals) is amorphous in nature.

It is important to note that the pH changes during the reaction time and in most cases the pH recorded after the crystallization of the material was different from the initial pH. The pH variations observed are shown in Figure 5.5 as a function of the tin content in the gel. For syntheses with a Si/Sn ratio of 50 and higher, the changes observed in pH are independent of tin content. In that compositional region, gels with an initial pH of 13.2 tend to have lower final pH values while gels with an initial pH of 12 and 10.6 tend to maintain and slightly increase their pH values respectively. However, at very high tin contents (i.e. Si/Sn≤25) there is a significant drop in the pH of the gels irrespective of the initial pH. This significant drop in the pH is likely a consequence of the formation of hydrochloric acid upon hydrolysis of the tin chloride.

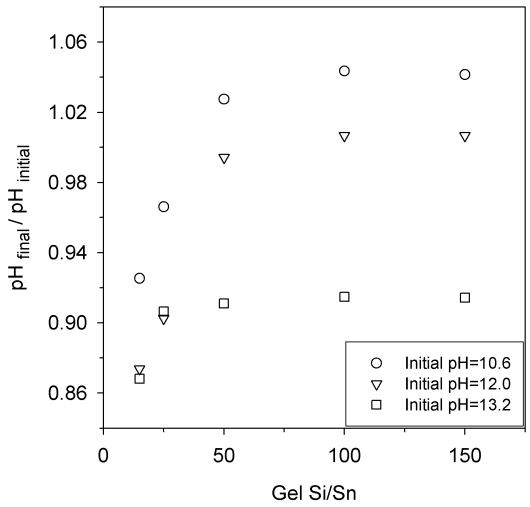

Figure 5.5 Variation in the pH of the synthesis gels after formation of Sn-MFI materials as a function of their tin content.

The results in Figure 5.5 raise a few important questions. For instance, is it the increase in tin content or the lowered pH that leads to the additional phase observed in Figure 5.4 and the reduced crystallinity observed in Figure 5.1? In order to observe the pH effect in isolation, one can compare samples made with the same tin content but different pH values. This comparison is shown in Figure 5.6. For a constant tin content, gels with an initial pH of 12 yield particles with smaller size (~1-3 μm), more rounded shaped and with less amount of particulates on the surface than gels with pH of 10.6 (~6-8 μm). At the same time, gels with pH of 13.2 yield materials that seem to be an inter-growth of very small crystals with no visible extra phase.

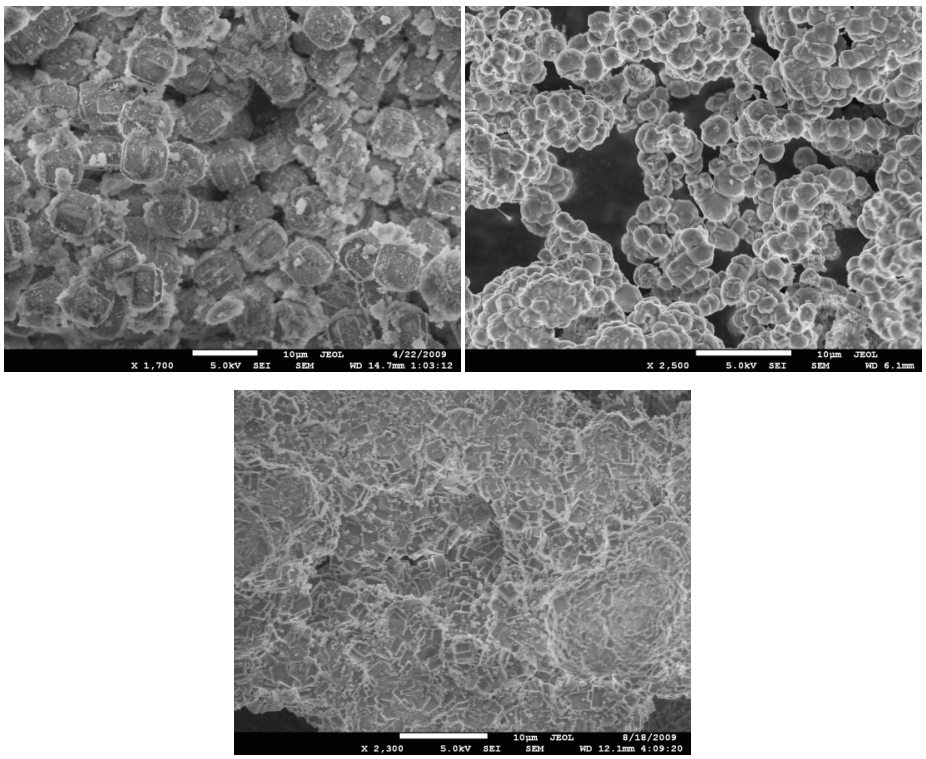

Figure 5.6 FE-SEM images of calcined Sn-MFI-100-*p* samples, where clockwise from top left *pH* = 10.6 (final pH = 11), *pH* = 12 (final pH = 12) and *pH* = 13.2 (final pH=12). The scale bar in all images is 10 μm.

It is clear that the formation of the additional phase is favoured at lower pH values and therefore one route to minimizing its formation is through pH. At low tin contents (i.e. Si/Sn≥50) the formation of the additional phase can be prevented by keeping the pH of the gels higher than 12. However, at high tin contents (Si/Sn≤25), formation of the additional phase is observed at all pH values investigated.

5.3.1.3 Bulk and surface composition

In order to determine the uptake of tin and also to obtain more insights on the nature of the additional phase that forms when high tin contents or low pH values are used, XRF and XPS were employed. Figure 5.7 shows the results of those measurements. Several conclusions can be made from the results. First, the uptake of tin is very high in all the materials as their Si/Sn ratios via XPS and XRF are lower than the Si/Sn ratios of the gel. Given that the yield of the syntheses is quite high (usually higher than 90%), the results in Figure 5.7 imply that all of the tin in the gel is associated with the final solid. Second, most of the samples appear to have significantly lower surface Si/Sn values than Si/Sn bulk values, indicating that there is enrichment of tin near the surface of the particles. Also, the disparity between the XPS and XRF values increases as the pH decreases and also as the tin content in the gel increases. This is consistent with FE-SEM images that show more small particulates (additional phase) on the zeolite surface as the Si/Sn ratio and pH decreased and leads to the conclusion that the additional phase is tin rich.

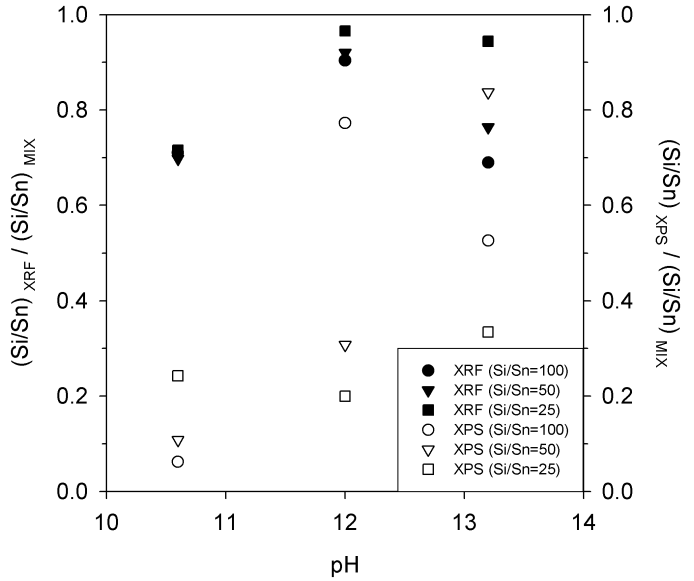

Figure 5.7 Si/Sn ratios via XRF (solid symbols) and XPS (hollow symbols) normalized by the gel Si/Sn ratio of calcined Sn-MFI samples as function of pH.

These results also correlate with the PXRD data that show relatively little change in the unit cell volume for the materials made at lower pH values (i.e. pH of 10.6 and 12) and high tin contents (i.e. Si/Sn<50). Since in those cases most of the tin is either enriched in the outer layers of the particles or most likely as part of the amorphous additional phase on their surface, one would not expect to have significant substitution of tin in the framework of the zeolites and consequently see changes in the unit cell volume. For the remainder of this chapter, we will refer to the tin on the outer surface of these materials as a surface phase. While this may not be exactly correct, it captures the key observation that there is significant enrichment of tin in the outer surface of the zeolite crystals as part of an extra phase.

Related to the nature of the tin overlayer, XPS also shows a very strong correlation between the concentration of sodium and tin on the surface of the crystals.

Figure 5.8 shows the surface Na/Si ratio determined via XPS as a function of the Sn/Si ratio in the gel. It can be seen that as the tin content in the gel increases (and therefore the tin concentration on the surface), the sodium concentration on the surface of the materials increases as well. For materials made at pH of 10.6, the concentration of sodium on the surface is always very high, which matches well with high concentration of tin due to the surface enrichment at low pH values. In the case of materials made at pH of 12 and 13.2, when the tin content in the gel is low, the concentration of sodium on the surface is low. However, when the tin content is high, there is always enrichment of tin on the surface and the concentration of sodium is high.

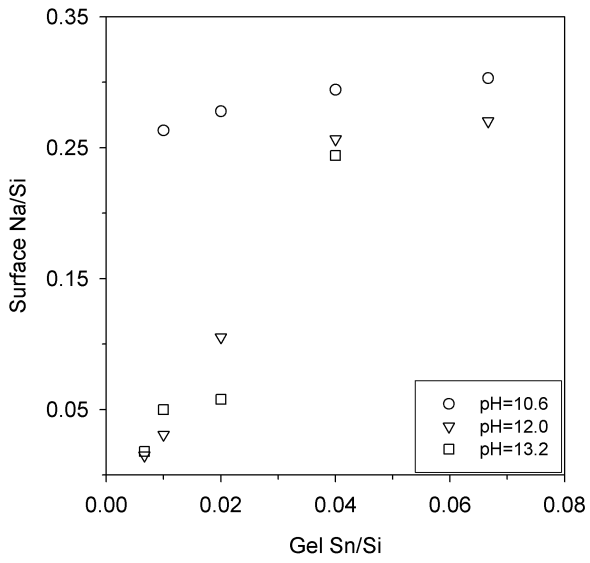

Figure 5.8 Concentration of sodium on the surface of calcined Sn-MFI samples as a function of the Sn/Si ratio in the gel.

These observations suggest that the tin overlayer might be a sodium stannate phase and could be forming due to the interaction of tin with sodium ions present in the

gel. In an attempt to remove the additional phase, the materials were treated with different aqueous solutions. Sodium nitrate (pH=5), acetic acid (pH=2.5), and ammonium hydroxide solutions (pH=10.4) were used. In each case, 50 ml of solution were mixed with 1 g of zeolite for 2 hours. None of these treatments resulted in a decrease of tin concentration in the surface (XPS Si/Sn ratios before and after treatment remained the same). The additional phase was also still visible by SEM.

In order to tie together the XPS, XRF and SEM more unambiguously, FE-SEM images were taken in conjunction with EDS line scans performed on samples. Figure 5.9 shows a representative example.

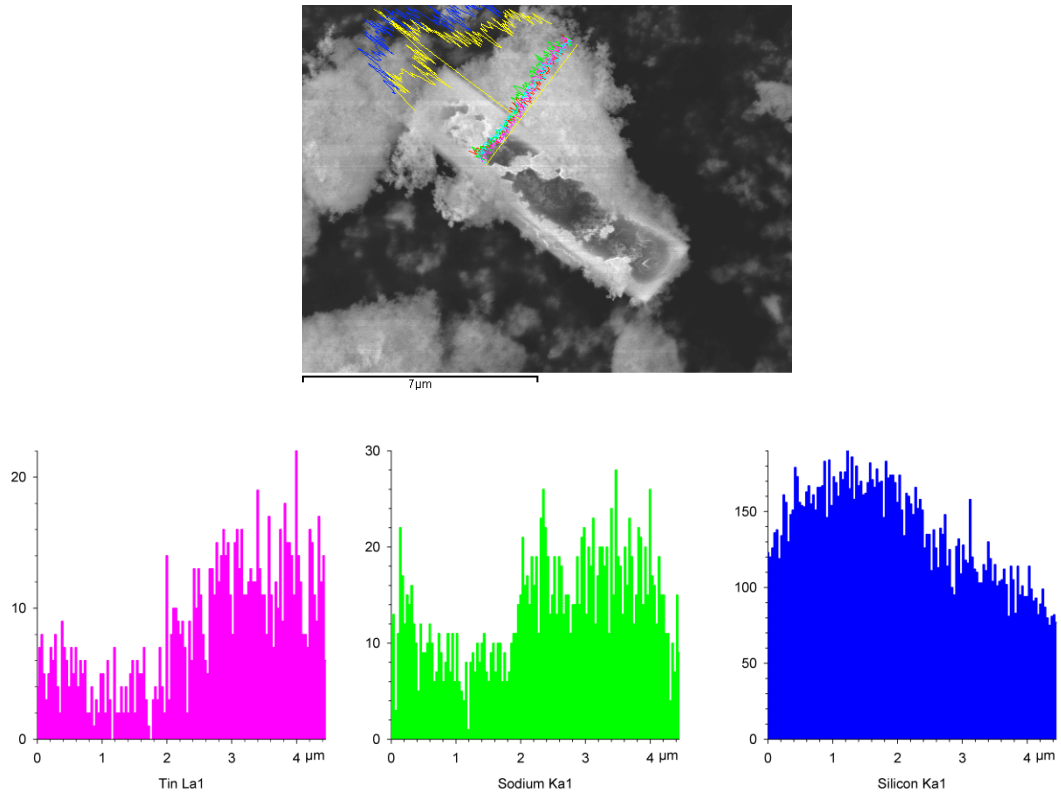

Figure 5.9 FE-SEM (top) and EDS line scan profiles of tin (left), sodium (center), and silicon (right) of Sn-MFI-50-10.6 sample.

As can be seen in the figure, the tin and sodium signals observed in the surface region (where a considerable amount of additional phase is present) are greatly enhanced, consistent with the XPS and XRF data. It is also noteworthy that this region has an appreciable silicon signal. On whole, the SEM, EDS, XPS, and XRF provide a self-consistent picture of this surface impurity phase being significantly enriched in sodium and tin as compared to the bulk of the zeolite crystals.

5.3.1.4 Porosimetry and spectroscopy

Other properties of these materials are now described. Figure 5.10 shows adsorption isotherms for the series of Sn-MFI-*c*-12 samples. As can be seen, these materials appear to possess both microporosity and a small amount of mesopores. The micropore volume of these materials as determined by the α_s-method systematically decreases from 0.13 cm^3/g to 0.12 cm^3/g to 0.10 cm^3/g as the Si/Sn ratio decreases from 100 to 50 to 25.

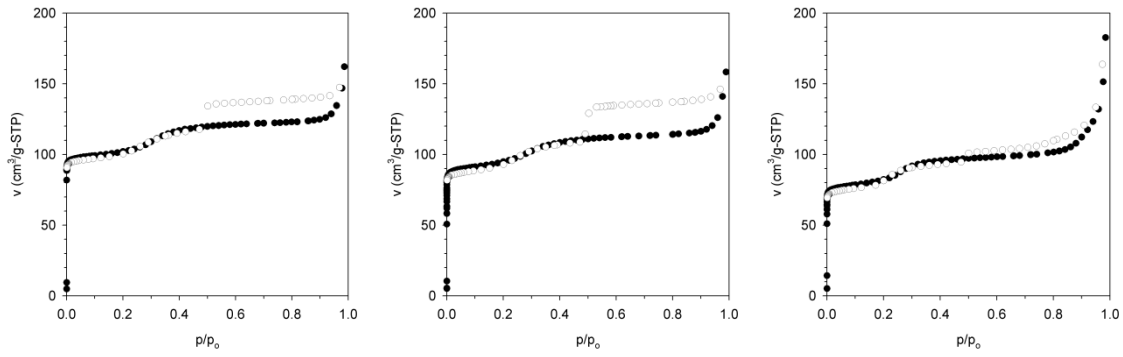

Figure 5.10 Adsorption isotherms of Sn-MFI-*c*-12 samples, clockwise from top left *c* = 100, 50 and 25.

In all three samples, a step in the amount of nitrogen adsorbed is observed at approximately a p/p_o value between 0.2 and 0.25, indicating the presence of a small amount of small (< 4 nm) mesopores. This feature is observed for all samples made with this preparation, even in the case of syntheses that contain no tin. Also, there is an appreciable amount of nitrogen adsorbed at relative pressures above 0.9, and the amount of nitrogen adsorbed in this region correlates with decreasing Si/Sn ratios. While the authors do not have a clear explanation for this, it appears that the nitrogen adsorbed at high relative pressures strongly correlates with the presence of the tin-rich surface phase observed by FE-SEM. Thus, the presence of this surface phase leads to a decrease in the micropore volume as well as the presence of adsorption of nitrogen at high relative pressures. The former could be a consequence of pore blockage or it could be due to the fact that the weight percent of the surface additional phase increases with increasing tin content, which affects the adsorption results that are given on a unit mass basis. Based on the information available to us we cannot eliminate one possibility over the other. Similar trends were observed for the materials made at different pH values.

Several spectroscopic methods were also used to investigate these materials. Figure 5.11 shows the Raman spectra of selected Sn-MFI samples and the FT-IR spectra of the as-made Sn-MFI-*c*-12 materials. The characteristic features of SnO_2 are not observable in the Raman spectra of any of the Sn-MFI materials synthesized, not even in the samples made with the highest tin content and the lowest pH. This suggests that, at least up to the detection limit of Raman, the materials made do not have any extra-framework SnO_2. A signal at approximately 540 cm^{-1} starts to develop in the Raman

spectra of the samples made with the lowest pH and Si/Sn ratios of 25 and 50 (i.e. Sn-MFI-*c*-10.6 with *c* = 25 and 50). These samples exhibited the largest amount of tin/sodium additional phase by SEM and XPS. The Raman spectrum of disodium tin trioxide (Na_2SnO_3) has the strongest signal at 540 cm^{-1} as well, which could indicate that the signal at 540 cm^{-1} in the Raman spectra of the zeolites is coming from the presence of the tin/sodium additional phase and gives more insight on its nature.

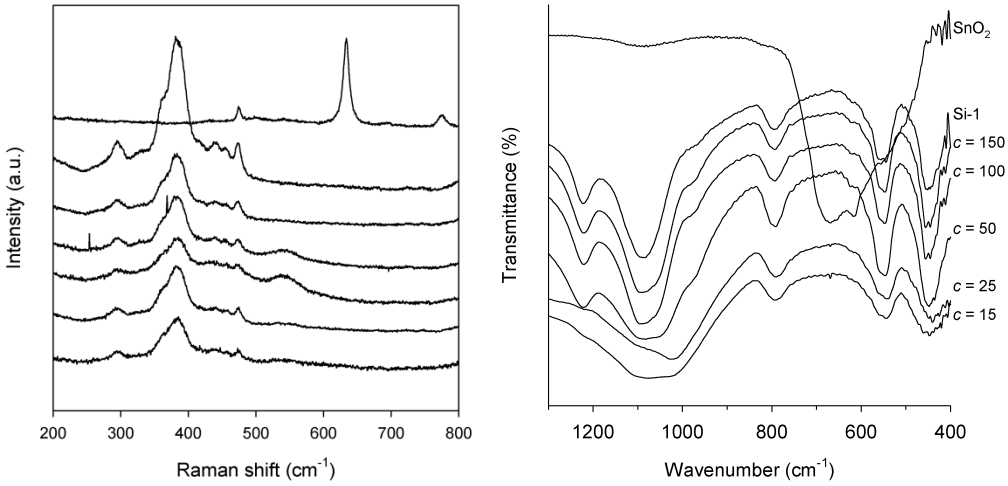

Figure 5.11 (Left) Raman spectra of selected Sn-MFI samples. From bottom to top: Sn-MFI-15-12, Sn-MFI-25-12, Sn-MFI-25-10.6, Sn-MFI-50-10.6, Sn-MFI-100-10.6, Silicalite-1 and SnO_2. (Right) FT-IR spectra of as-made Sn-MFI-*c*-12 samples.

From the FT-IR spectra several observations can be made. First, the asymmetric stretching T-O-T lattice vibration (~1100 cm^{-1}) shifts towards lower values with increasing tin content for both series of samples made at pH of 12 and 13.2. Similar shifts have been observed in other substituted MFI zeolites such as Ti- and Sn-MFI and it is generally taken as an indication of heteroatom incorporation in the framework[43,55,142]. For Sn-MFI-*c*-10.6 samples, the shift is only observed for Si/Sn contents of 50 and

higher. In addition to that, samples made with Si/Sn≥50 exhibit a very weak shoulder at approximately 980 cm^{-1}. A similar but more intense shoulder has been observed in titanium-substituted MFI zeolites[43,142]. It is believed that this band arises from the Ti-O-Si linkages and it is taken as unequivocal substitution of titanium in the MFI framework. In the case of Sn-MFI zeolites this shoulder has been observed as well but the intensities are usually much lower than in the case of Ti-MFI[55,59,156]. Sn-free silicalite-1 also exhibits the presence of that shoulder (possibly due to the presence of siloxy groups) but it is less intense than in the Sn-MFI.

Figure 5.12 shows the ^{29}Si MAS NMR spectra of the as-made and calcined Sn-MFI-50-12 sample. The as-made sample shows a strong resonance at -115 ppm assigned to the $Si(OSi)_4$ species and a weaker one at -105 ppm that corresponds to silicon atoms surrounded by other 3 silicon atoms. The latter resonance could be assigned to either Q^3 groups (where Q^n stands for $X_{4-n}Si(OSi)_n$, X = OH or O^-)[157,158] or $Si(OSi)_3(OSn)_1$ sites, or both. Upon calcination the resonance at -105 ppm decreases considerably. This result indicates that the resonance at -105 ppm for the as-made sample was primarily Q^3 groups, which condense upon calcination[158]. $Si(OSi)_3(OSn)_1$ sites, if present, are not observable most likely due to the low tin content in the materials. Fitting of the ^{29}Si MAS NMR spectra of the as-made sample indicates that Q^3 groups are approximately 19% of the entire signal.

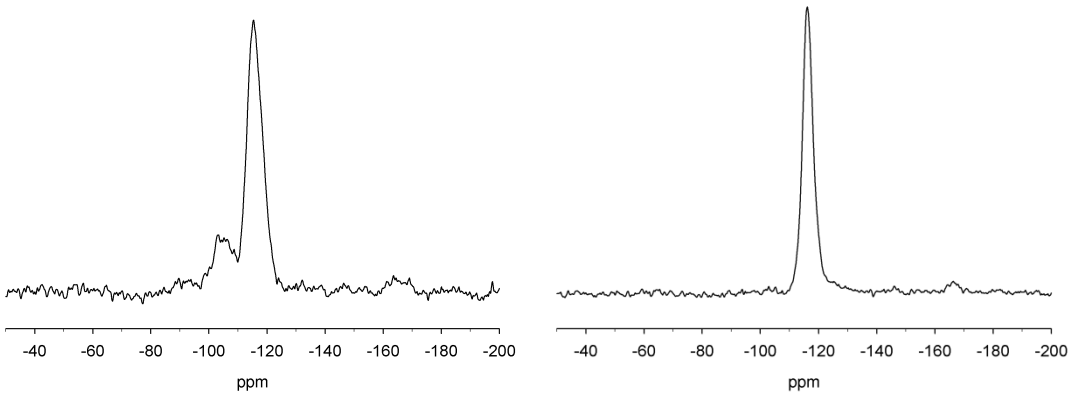

Figure 5.12 ^{29}Si MAS NMR of as-made (left) and calcined (right) Sn-MFI-50-12 sample.

Diffuse reflectance UV-Vis is commonly used to study the coordination environment of the tin in tin-substituted zeolites. However, the silica source used in this work (Ludox AS-40) contains a small amount of iron that absorbs strongly in the 200-300 nm region[159]. After considerable work, it is our conclusion that we cannot unambiguously interpret the UV-Vis spectra of these samples. Consequentially, the Sn-MFI materials made could not be analyzed using this technique. As an alternative, a few Sn-MFI samples were made using fumed silica as the silica source following the same procedure used for the Ludox materials made at a pH of 12. Those samples were analyzed by UV-Vis and the results are shown in Figure 5.13. The spectra obtained are consistent with tin ions being in tetrahedral coordination based on prior literature[59,160]. Again, there is no evidence for SnO_2 given the absence of a strong signal at 280 nm.

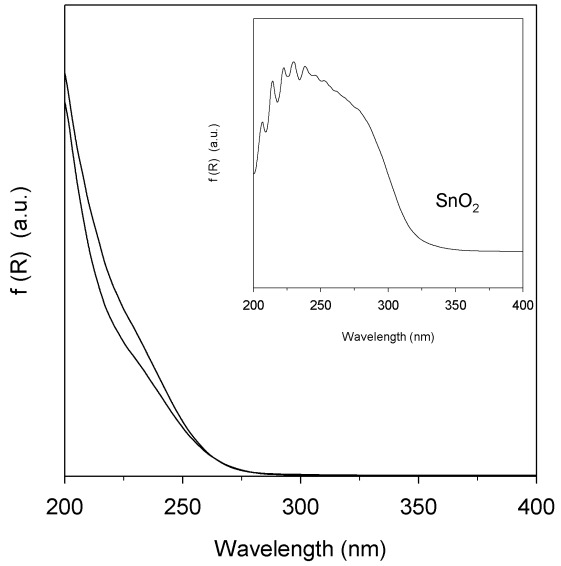

Figure 5.13 Diffuse reflectance UV-Vis spectra of Sn-MFI-*c*-12 samples made using fumed silica in the presence of sodium hydroxide, where from top to bottom c = 50 and 100.

5.3.2 Syntheses in the absence of sodium

5.3.2.1 X-ray diffraction

Given that the XPS and EDS results for the Sn-MFI materials made in the presence of sodium showed a correlation between tin and sodium enrichment in the additional phase on the surface of the zeolite crystals, syntheses in the absence of sodium hydroxide were performed in order to understand in more detail why the surface phase forms and how sodium ions contribute to its formation and to other properties of the material. Figure 5.14 shows the PXRD patterns of the as-made and calcined Sn-MFI-*c*-*NS* samples. The materials are MFI and crystalline impurities are not observable. In general, the materials are highly crystalline with the exception of the one made with Si/Sn ratio of 25 that shows less intense reflections. The as-made Sn- MFI-*c*-*NS* samples

can be indexed using an orthorhombic unit cell. It was observed, however, that upon calcination they retain this type of unit cell as well (reflections at 2θ = 24.4° and 29.3° do not split).

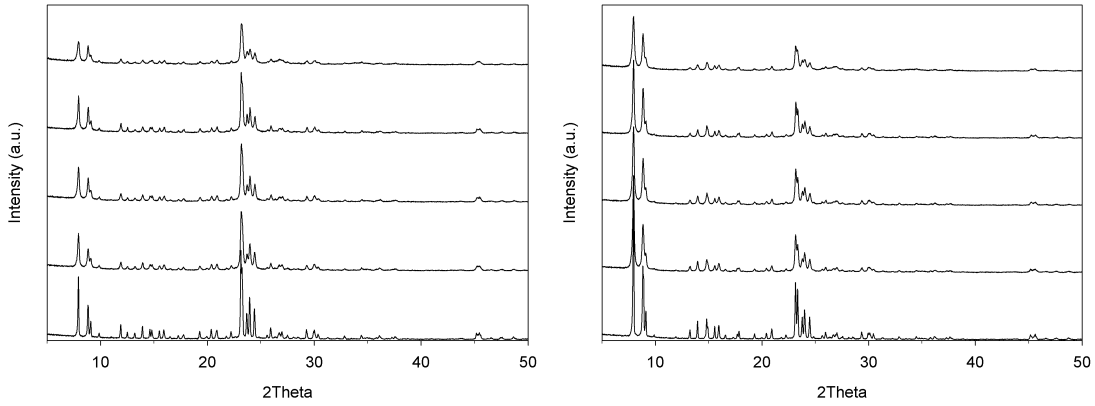

Figure 5.14 PXRD patterns of as-made (left) and calcined (right) Sn-MFI-*c*-*NS* samples, where from top to bottom *c* = 25, 50, 75, 100 and 150.

Retention of the orthorhombic unit cell has been observed for other heteroatom-substituted MFI zeolites and it is taken as an indication of substitution in the framework[43,142]. This is an important difference with respect to the materials made in the presence of sodium since all the sodium-containing zeolites changed to a monoclinic unit cell upon calcination. The unit cell volume of the Sn-MFI-*c*-*NS* materials is shown in Figure 5.15. The unit cell volume decreases as the tin content in the gel increases. This contraction in the unit cell volume was also observed for the sodium containing zeolites made at pH of 13.2 and also for the low tin content ones made at lower pH values.

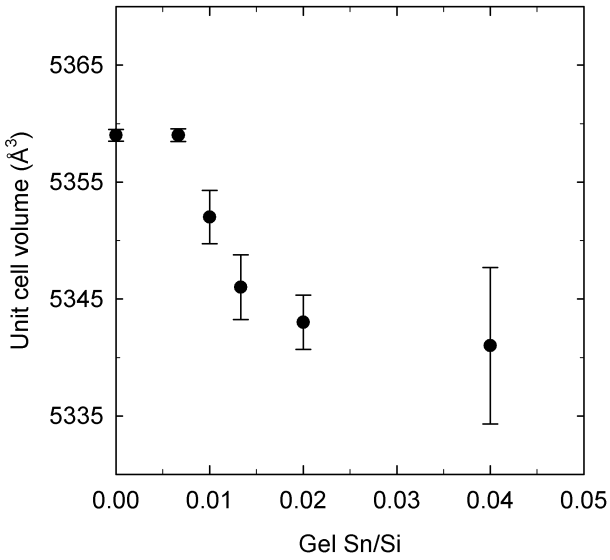

Figure 5.15 Unit cell volume of Sn-MFI-*c*-*NS* samples as a function of the tin content in the gel.

5.3.2.2 FE-SEM

FE-SEM images for the Sn-MFI-*c*-*NS* samples are shown in Figure 5.16. The surface of these materials do not appear to have the additional phase that was observed at high tin contents and low pH values for the sodium-containing zeolites. The fact that these materials do not show the additional phase is most likely due to the absence of sodium ions rather than a pH and tin content effect. This statement is based on the observation that the sample made with a Si/Sn content of 25 (i.e. Sn-MFI-25-*NS*) does not exhibit the particulates that were always very evident in the sodium-containing samples made with the same tin content. Further, the pH of the gel after crystallization of the Sn-MFI-25-*NS* sample dropped below 10. At that pH value, formation of this extra phase was always evident in the sodium-containing syntheses, even for the lowest tin contents used. The particle size and morphology of the crystals vary with the tin

content and a decreasing size with increasing tin content trend is observed. The lowest tin content gel yield large particles with sizes between 5 and 15 μm. Intermediate tin contents (i.e. Si/Sn ratios of 100 and 50) yield particles of 1 to 2 μm and the highest tin content prep yields very small particles less than one micron in size. This trend is very different from the one observed for the sodium-containing Sn-MFI samples in which the particle size always increased as the tin content in the gel increased. In addition, the particles obtained through the non-sodium gels are much more uniform in size and in shape than the ones obtained in the presence of sodium.

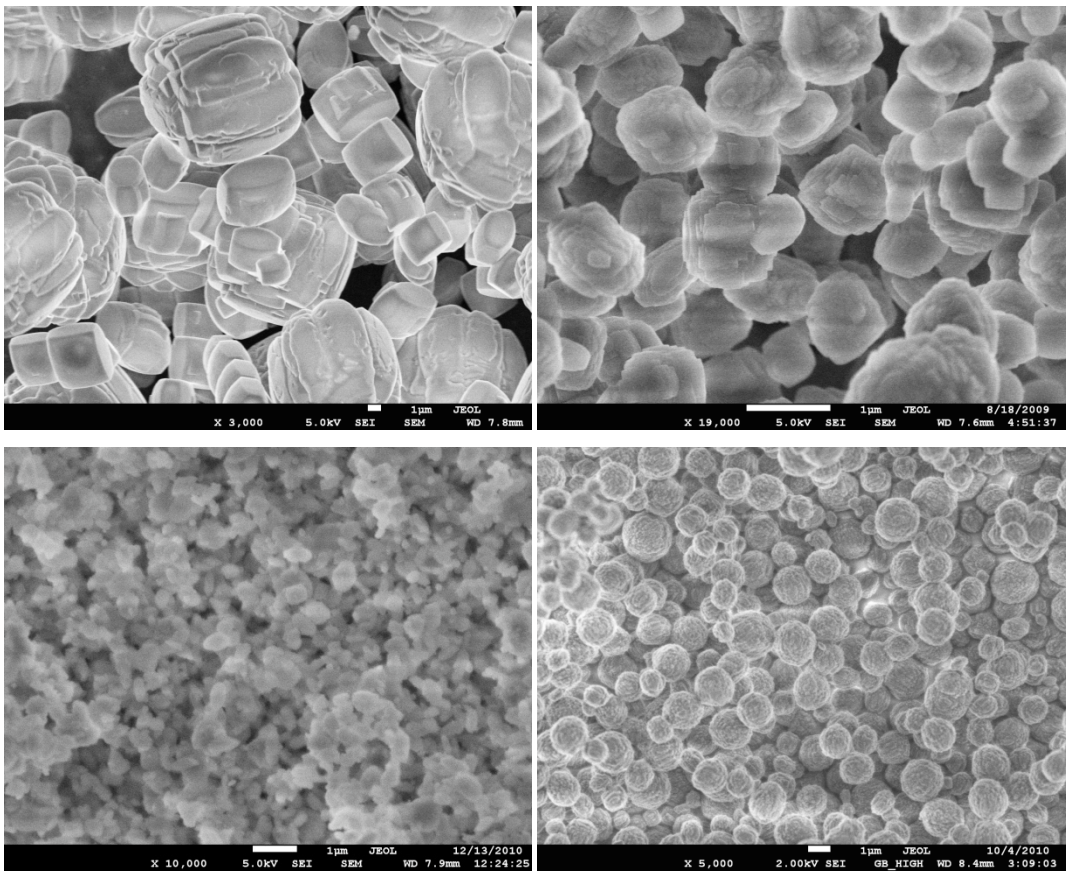

Figure 5.16 FE-SEM images of as-made Sn-MFI-*c*-*NS* samples, where clockwise from top left: c = 150, 100, 50 and 25.

Several possible explanations for the particle size and morphology effects can be made. The particle size effect observed in the non-sodium preparations can be attributed to the increasing TPAOH concentration with increasing tin content. All things being equal one could anticipate that the nucleation rate increases with increasing TPAOH content, leading to smaller particles. The increasing crystallization time needed with increasing tin content has been observed for fluoride-mediated Sn-Beta preparations, and a similar trend is observed in the current work. Given the clear correlation between tin and sodium in the surface additional phase, it is tempting to believe that the presence of sodium leads to the formation of sodium-tin oxide materials or sodium-tin-silicon oxide materials. Controls performed with no sodium hydroxide but addition of sodium chloride yielded similar materials to those made with sodium hydroxide, lending credence to this hypothesis.

5.3.2.3 Bulk and surface composition

The composition of these materials was also investigated via XPS and XRF. The results are shown in Figure 5.17. The uptake of tin in these materials is fairly high since 85% or more of the tin present in the gels is associated with the solid (the yields are always above 95%). The only exception was the sample made with a Si/Sn ratio of 50 in which only 67% of the tin in the gel was present in the final solid. The XPS Si/Sn ratio is a little lower than the bulk ratio for most of the samples (the exception being Sn-MFI-150-*NS* in which the XPS ratio is much larger than that in the bulk and basically no tin ions are found in the surface). Even though there is still some enrichment of tin in the

outer layers of the crystals, this enrichment in not as large as the one observed for the sodium containing samples. In this case, there is a much better agreement of XPS and XRF, which supports the FE-SEM images that indicated the absence of an additional phase in the surface of the particles and consequently more phase pure materials.

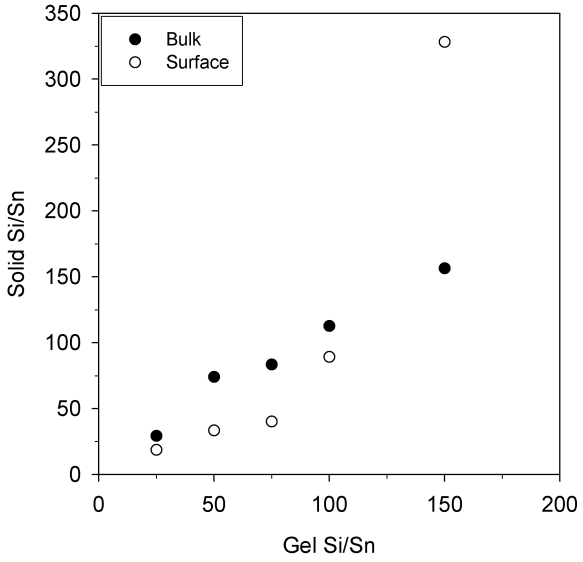

Figure 5.17 Bulk (via XRF) and surface (via XPS) Si/Sn ratios of Sn-MFI-*c-NS* samples as a function of the Si/Sn content in the gel.

5.3.2.4 Porosimetry and spectroscopy

Figure 5.18 shows the nitrogen adsorption isotherms for the Sn-MFI-*c-NS* samples. The micropore volumes as determined by the α_s-method are 0.154, 0.154 and 0.135 cm^3/g for the samples made with a Si/Sn ratio of 150, 50 and 25 respectively. The micropore volume of the non-sodium materials is nearly identical to the one determined for pure silicalite-1 (0.154 cm^3/g) which indicates that there is no loss in sorption capacity upon introduction of tin. The sample made with a Si/Sn ratio of 25 exhibits

little lower micropore volume, which is likely due to the slightly lower crystallinity of this material, compared to the lower tin content ones in the series (via PXRD). In any case, the micropore volumes of the non-sodium samples are always higher than the volumes of the sodium-containing samples.

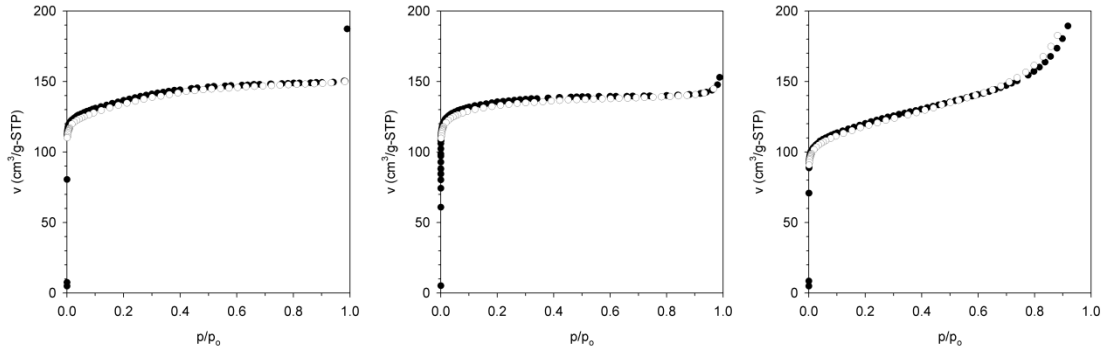

Figure 5.18 Adsorption isotherms of Sn-MFI-*c*-*NS* samples. From left to right: *c* = 150, 50 and 25.

Figure 5.19 shows the FT-IR spectra of the as-made and calcined Sn-MFI-*c*-*NS* materials. In this case, it is also observed that the wavenumber of the T-O-T asymmetric stretching vibration (~1100 cm^{-1}) shifts slightly towards lower values as the tin content increases. The weak shoulder at approximately 980 cm^{-1} is also present in all Sn-MFI-*c*-*NS* materials. In the as-made form, the tin free silicalite-1also exhibits the shoulder at 980 cm^{-1}, but its intensity is lower when compared with the tin-containing samples. After calcination, the shoulder is absent from the silicalite-1 spectrum but remains present for the Sn-MFI-*c*-*NS* samples. Contrary to this, the sodium-containing Sn-MFI did not exhibit the shoulder upon calcination. As was mentioned before, the shift in the wavenumber of the T-O-T vibration and the presence of the shoulder at approximately

980 cm^{-1} are usually taken as positive indication of tin substitution in the framework of MFI zeolites.

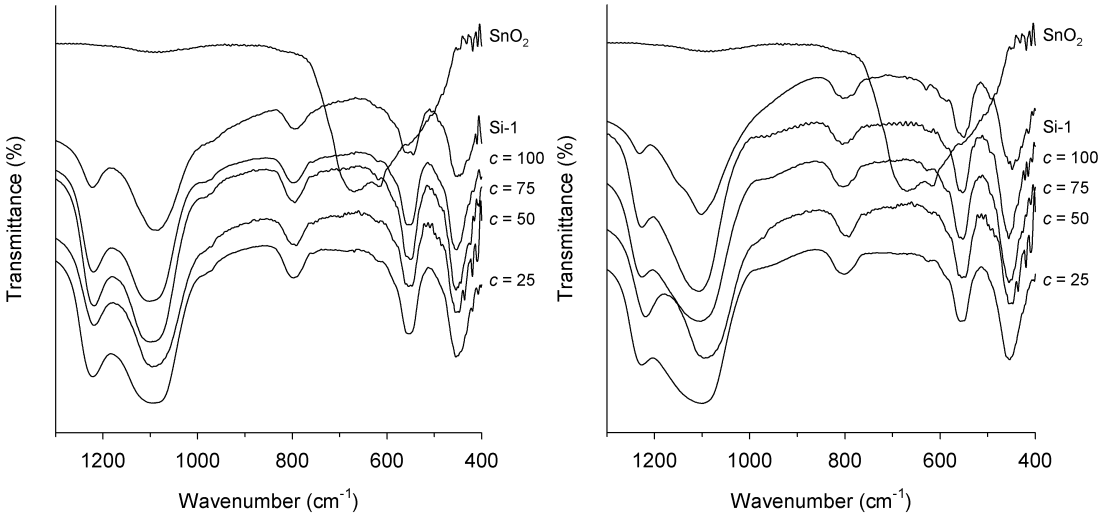

Figure 5.19 FT-IR spectra of as-made (left) and calcined (right) Sn-MFI-*c*-*NS* samples.

NMR was also used to study the non-sodium materials. Figure 3.20 shows the ^{29}Si MAS NMR spectrum of the as-made and calcined Sn-MFI-50-*NS* (sample made with a Si/Sn ratio of 50). The as-made material shows a strong resonance at -115 ppm and weaker one at -105 ppm. The same resonances were observed in the as-made spectrum of the sodium-containing material shown in Figure 5.12. As it was mentioned above, the resonance at -115 ppm arises from the presence of $Si(Osi)_4$ sites and the one at -105 ppm arises from either Q^3 groups or silicon atoms with adjacent tin centers or a combination of both sites. The Q^3 sites are 10% of the entire signal. After calcination, the resonance at -105 ppm is slightly reduced but it is still clearly observable, approximately 12% of the entire signal, in contrast to the samples made in the presence

of sodium. There are two possibilities to explain this; either there is more tin in the framework in $Si(OSi)_3(OSn)_1$ sites or fewer silanol group condense during calcination of these samples. To qualitatively address this, ^{29}Si CP-MAS NMR was performed on the calcined sample. As can be seen in the bottom of Figure 5.20 there is strong enhancement of the line at -105 ppm, consistent with the presence of silanol groups. Given the difficulty in quantifying CP-MAS results, no definitive conclusions can be drawn, other than that it is likely that the silanol groups condense less effectively in the samples without sodium.

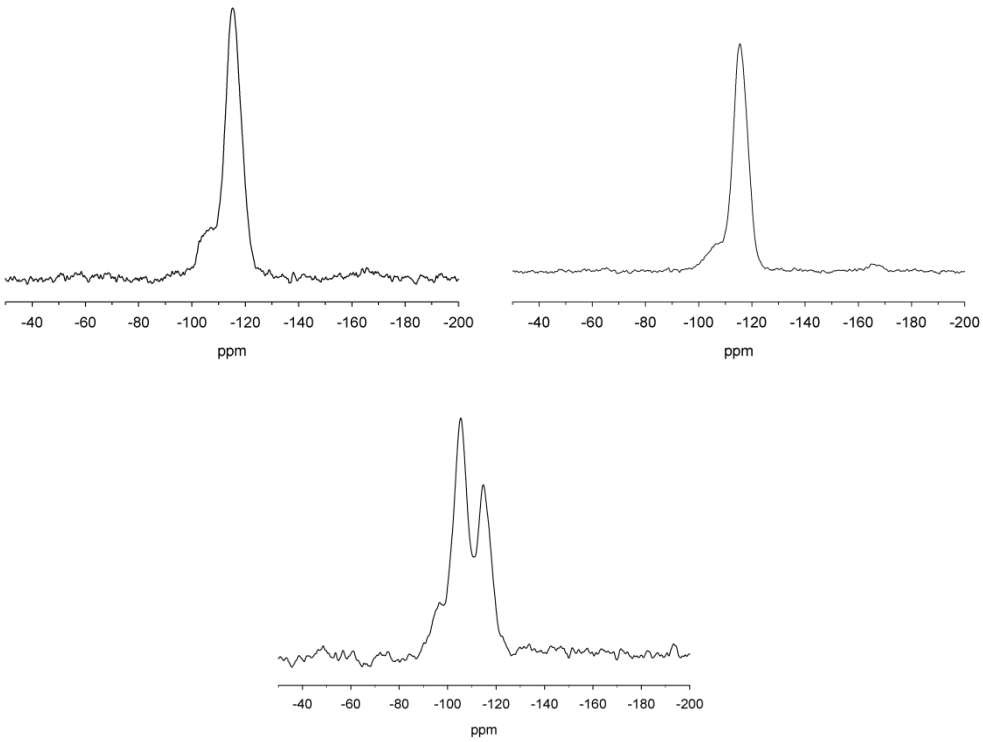

Figure 5.20 ^{29}Si MAS NMR spectra of as-made (top left) and calcined (top right) Sn-MFI-50-*NS* sample. ^{29}Si CP-MAS NMR spectrum of calcined Sn-MFI-50-*NS* sample (bottom).

The Sn-MFI materials made in absence of sodium were also studied by UV-Vis. However, as it was mentioned above, the iron impurities present in the silica source used (Ludox AS-40) did not allow for the spectra to be unambiguously studied. As an alternative, a few Sn-MFI samples were made using fumed silica and following the procedure used to make Sn-MFI-*c*-*NS* materials from Ludox. Figure 5.21 shows the UV-Vis spectra of those samples. The UV-Vis signal at approximately 200-205 nm is in agreement with tin in tetrahedral coordination as suggested in the literature. The weak signal at approximately 220 nm has been related to penta-coordinated tin detected in hydrated Sn-MFI zeolites.

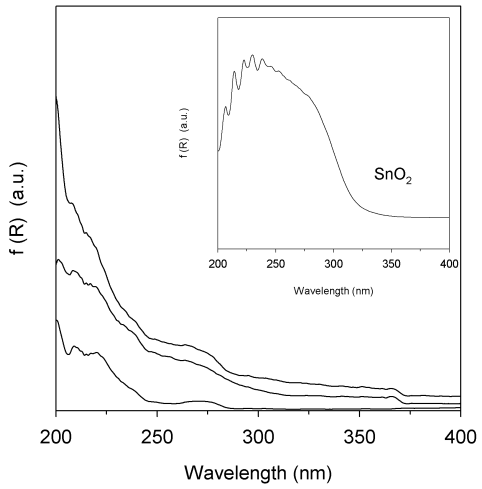

Figure 5.21 Diffuse reflectance UV-Vis spectra of Sn-MFI-*c*-*NS* samples made using fumed silica in absence of sodium hydroxide, where from top to bottom c = 100 and 50 and 150.

Important differences are observed in the properties of Sn-MFI materials synthesized from gels containing sodium ions versus gels without sodium. Sodium containing reagents are routinely used in the synthesis of zeolites but in many cases the

effect of having sodium ions in the gels is not considered, specially in synthesis of substituted zeolites. Sodium-containing gels yield materials that tend to precipitate a sodium-stannate extra phase on the surface of the zeolite particles, which is an impurity for the Sn-MFI materials. The overlayer is especially stable at low pH and it becomes significant at high tin contents. Two control experiments were done to see if varying the sodium source or varying the order of addition of the reagents would affect the formation of the impurity. In the first, sodium chloride was added to the gels in replacement of sodium hydroxide to see if comparable results regarding the formation of the tin/sodium overlayer were obtained. In that case, a Si/Sn ratio of 50 and pH values of 12 and 13.2 were used. The second control experiment involved changing the order of addition of the reagents. Sodium hydroxide was added at the end (after the basic tin-silica-TPAOH gel was formed) to see if there was any positive effect on the overlayer formation. In that case, a Si/Sn ratio of 50 and pH values of 12 and 10.6 were used. In both cases, formation of the tin/sodium extra phase was observed, resulting in materials that resemble the properties of the Sn-MFI originally synthesized. These results support the idea that the presence of sodium ions inhibits the formation of phase pure materials by interacting with tin ions present in the gels to form a stable sodium-stannate phase that precipitates on the crystals.

5.4 Conclusions

A series of Sn-MFI zeolites were made by conventional hydrothermal synthesis in hydroxide media following two synthetic routes that involved the presence and the

absence of sodium ions in highly concentrated synthesis gels. By using a wide range of characterization techniques, significant differences on the properties of the materials made were found. Sodium-containing gels yield materials that tend to have a sodium-stannate impurity on the surface of the particles that forms by interaction of sodium and tin ions in the synthesis gels. The impurity is very stable at low pH, becomes significant when high tin contents are used, decreases the crystallinity of the materials and their adsorption capacity and prevents the tin ions from being substituted in the framework of the zeolite. By keeping the pH of the gels above 12 and by maintaining the tin content below 3 wt% the formation of the extra phase is minimized and materials that appear to be more uniform with some tin substituted in the framework, as indicated by PXRD, FT-IR and UV-Vis, can be synthesized.

On the other hand, the sodium free synthetic route yields materials with very different characteristics. The materials obtained through this route do not contain the sodium-stannate impurity and consequently are phase pure with tin contents up to 6 – 7 wt%. They are highly crystalline materials with very uniform and small particle size, which is advantageous for catalytic applications. These materials also have high adsorption capacity that does not decrease considerably at high tin contents and have a better substitution of tin ions in the framework as indicated by the changes in the unit cell volume, retention of the orthorhombic unit cell upon calcination and features in the FT-IR and UV-Vis spectra.

CHAPTER VI

CATALYTIC ACTIVITY OF SN-MFI ZEOLITES FOR PHENOL HYDROXYLATION

6.1 Introduction

As demonstrated in chapter V, Sn-MFI syntheses are affected by the presence of sodium ions. Synthesis routes involving the use of sodium containing mixtures lead to Sn-MFI zeolites with significant amounts of a surface sodium stannate impurity that prevents the incorporation of tin in the zeolite framework. On the other hand, Sn-MFI zeolites prepared in the absence of sodium cations exhibit better properties in terms of phase purity, absorption capacity and incorporation of tin. One way to investigate the quality of the zeolites and probe the successful incorporation of tin is to test their catalytic behavior.

Sn-MFI zeolites have been previously used to catalyze the hydroxylation of phenol with hydrogen peroxide. As mentioned in chapter I, these materials have been reported to successfully catalyze this reaction with very high hydrogen peroxide conversions and selectivities towards catechol and hydroquinone that range from 40 – 60%. The reported catalytic activity of Sn-MFI in this reaction is significant, although not superior, especially in terms of selectivity, to that obtained with TS-1 (which is in fact the catalyst used at an industrial scale). This chapter reports on the catalytic activity of phenol hydroxylation observed with the Sn-MFI zeolites prepared in this dissertation,

especially those made from sodium free mixtures. The results presented in this chapter are, in some aspects, different from what has been reported in the literature.

The Sn-MFI materials used for catalytic testing in this chapter were prepared using the sodium free synthesis route specified in chapter V, as they exhibit better incorporation of tin and phase purity. The materials were, however, prepared using higher concentrations of TPAOH than those reported in the previous chapter. The reason for this was that increasing TPAOH concentration increases crystallization time, and results in materials with higher crystallinity and more consistent catalytic properties.

6.2 Experimental

Sn-MFI zeolites were prepared from gels with the following composition: SiO_2: *x* $SnCl_4$: *y* TPAOH: 15 H_2O, with molar Si/Sn = 150, 100, 75 and 50. The TPAOH/Si molar ratio was increased with increasing tin content and was equal to 0.21, 0.3, 0.4 and 0.5 respectively. Ludox was used as a silica source and sodium cations were absent. Other Sn-MFI zeolites were also prepared from gels of similar compositions, but using fumed silica and TEOS as silica precursors. The reason for changing the silica source, as will be explained in more detail below, was to be able to study the coordination environment of the tin by using UV-Vis spectroscopy, and use it to rationalize catalytic activity. Details of all synthesis procedures and catalytic testing protocol are given in chapter II.

6.3 Results and discussion

6.3.1 General catalyst characterization

Characterization with powder X-ray diffraction showed that Sn-MFI zeolites made with Ludox were highly crystalline. Only the sample made with the highest tin content (Si/Sn = 50) exhibited diffraction peaks with lower intensity (approximately 20% lower compared to the other zeolites). The lower intensity peaks are attributed to a higher absorption of tin, which is present in larger amount in that particular sample, rather than a loss in crystallinity. Evidence in support of this is that the micropore volume, obtained by nitrogen physisorption, is approximately 0.154 cm^3/g for all samples including the one with the highest tin content. This indicates that the crystallinity is most likely preserved in all samples. Table 6.1 shows the tin content in the zeolites as well as the particle size. It can be seen that, for samples with Si/Sn ≤ 144, the tin content in the surface is a little higher than that of the bulk, indicating some degree of tin enrichment on the surface. This enrichment is, however, not nearly as high as that observed for zeolites made in the presence of sodium (chapter V). The particle size decreases with increasing tin content.

Table 6.1 Particle size and tin content in Sn-MFI zeolites made with Ludox.

Si/Sn *in gel*	Silica source	Si/Sn *in bulk*	Si/Sn *in surface*	Particle size (μm)
∞	Ludox	∞	∞	8 – 9
150	Ludox	172	312	7 – 8
100	Ludox	144	76	2 – 3
75	Ludox	124	59	2 – 3
50	Ludox	88	56	1 – 2

UV-Vis spectroscopy was not suitable for studying the coordination of Sn-MFI samples made with Ludox as silica precursor. As mentioned in chapter V, iron impurities coming from the silica source absorb radiation in the same wavelength region where tin shows absorption. Other characteristics regarding phase purity and tin incorporation (unit cell volume decrease and symmetry retention upon calcination) are in line with the results presented in chapter V for samples made in the absence of sodium.

6.3.2 Catalytic testing

6.3.2.1 Activity of calcined zeolites

Initial catalytic testing of Sn-MFI samples made with Ludox showed low activity in hydroxylation of phenol, even after 24 hours of reaction. The catalysts appeared to poison at low hydrogen peroxide conversions. This statement is based on the visual observation of the catalysts turning dark after typical reaction time periods of 1 – 4 hours. Several different calcination procedures were performed in order to see if the way of activating the zeolites had any effect on their catalytic behavior. Two particular sets of experiments were done in this regard. First, calcination in air (either in static air or flowing air) was compared to calcination in nitrogen (to pyrolyze the TPA cations prior to combustion) followed by calcination in air. The main concern here was to see if calcination in air could possibly alter the tin coordination state by leading to formation of SnO_2 species. The second set of experiments were concerned with calcinations in the presence (or absence) of water vapor in air or nitrogen/air streams. This was done because, based on prior literature for Sn-Beta zeolites, the use of water saturated air

streams leads to improvement of catalytic activity. This improvement has been attributed to an increase in defect OH sites at the tin centers, which are believed to be more reactive than fully oxygen coordinated tin sites. Table 6.2 shows a summary of these experiments and the effect on activity in hydroxylation of phenol.

Table 6.2 Different calcination procedures and activity of Sn-MFI made with Ludox

Gel Si/Sn	Calcination	Comments	H_2O_2 conversion*	Poisoning
150	Air/5h at 500°C	Static air	10.5%	Yes
150	Air/5h at 500°C	Flowing air	6.8%	Yes
150	N_2/6h at 500°C Air/1h at 500°C	Flowing N_2 and air	6.9%	Yes
50	Air/5h at 500°C	Static air	7.6%	Yes
50	Air/5h at 500°C	Flowing air	6.5%	Yes
50	N_2/6h at 500°C Air/1h at 500°C	Flowing N_2 and air	6.1%	Yes
150	Air/5h at 500°C	Flowing dry air *Sample dried in vacuum prior calcination*	7.8%	Yes
150	N_2/3h at 150°C N_2/6h at 500°C Air/1h at 500°C	Flowing dry N_2 and dry air *Sample dried in vacuum prior calcination*	6.5%	Yes
150	Air/5h at 500°C	Flowing air *Saturated with water at 30°C*	11.1%	Yes
150	Air/5h at 500°C	Flowing air *Saturated with water at 50°C*	10.3%	Yes
∞	Air/5h at 550°C	Flowing air	7.2%	No

*Conversion after 24 hours of reaction

The information presented in the table shows that calcined Sn-MFI zeolites made with Ludox are not significantly active for the hydroxylation of phenol. The catalysts appear to poison at low hydrogen peroxide conversions regardless of activation procedure. Thermogravimetric analysis of catalysts after catalytic testing (dark colored samples) revealed a weight loss of approximately 3 wt% in the range of 100 – 500°C.

The zeolites turned from dark brown to white again after the thermal treatment, indicating that organic species were occluded in the zeolites during catalysis. It is important to note that, prior to catalytic testing, all zeolites were white and the weight loss recorded during activation corresponded well to that of TPA cations in MFI zeolite frameworks (4 TPA/u.c.).

These catalytic results are in contrast to what was reported by Mal et al[57]. They reported that Sn-MFI zeolites made with TEOS, which were calcined in air at 500°C, were highly active with hydrogen peroxide conversions of 100% and selectivities to hydroquinone and catechol of approximately 60% after 24 hours of reaction. In an attempt to replicate their published results, a Sn-MFI zeolite (gel Si/Sn = 50) was made with TEOS following their synthesis procedure[55], and then tested in the reaction. This sample was inactive for phenol hydroxylation (hydrogen peroxide conversion of 2.2%). Catalyst poisoning was not observed in this case. Since Sn-MFI zeolites made with TEOS could be studied using UV-Vis spectroscopy (no iron impurities), this technique was used to investigate the zeolite in the as-made and calcined form (Figure 6.1). As can be seen, the figure shows an absorption feature at around 215 nm for the as-made sample, while, upon calcination at 500°C in air, two absorption features at 200 and 300 nm are present. According to the general interpretation of the UV-Vis spectra of Sn-MFI zeolites, the absorption feature at around 215 nm (in as-made sample) is most likely to correspond to tin in tetrahedral coordination.

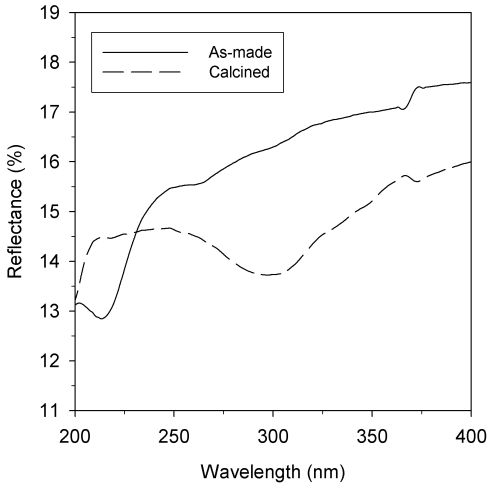

Figure 6.1 UV-Vis spectrum of as-made and calcined Sn-MFI zeolite made with TEOS and following the synthetic procedure described by Mal et al[55].

The absorption feature at 300 nm, in the calcined sample, indicates that octahedral SnO_2 species are most likely present. As shown in chapter V, SnO_2 exhibits a strong absorption that starts at 300 nm. This suggests that a significant change in the environment of tin is occurring during the calcination process, and could be the reason for the lack of catalytic activity of the calcined Sn-MFI zeolite made with TEOS. The materials prepared by Mal were not reported to have SnO_2 species after calcination (per UV-Vis characterization), which is different from what we have observed in this dissertation.

6.3.2.2 Activity of as-made zeolites

Based on the results shown above, the as-made form of Sn-MFI (TEOS) was tested in the reaction. The hydrogen peroxide conversion and selectivity towards hydroquinone and catechol were, after 8 hours of reaction, 57% and 52% respectively

with catechol/hydroquinone (Cat/HQ) ratio of 1.8, indicating that this sample (in as-made form) is in fact active. The coordination environment of tin in as-made versus calcined samples seems to be the key to explain the catalytic behavior observed. This finding led us to investigate the activity of the as-made Sn-MFI (Ludox) samples as well. Tables 6.3 shows the results of those experiments after 8 and 24 hours of reaction.

Table 6.3 Activity data for as-made Sn-MFI (Ludox) samples after 8 and 24 hours. H_2O_2 is the limiting reagent (starting phenol/H_2O_2 = 3). The values listed for catechol (Cat) and hydroquinone (HQ) are the respective selectivities defined as (moles product)/(moles H_2O_2 reacted) x 100%.

Si/Sn *In surface*	**Phenol** *(% Conversion)*	**H_2O_2** *(% Conversion)*	**Cat**	**HQ**	**Total** *(% Selectivity)*	**Cat/HQ**
After 8 hours of reaction						
312	20.5	60.6	30.3	15.9	46.2	1.91
76	24.6	71.6	29.9	16.1	46.0	1.86
59	32.5	96.3	31.5	18.2	49.7	1.73
56	30.5	92.4	31.9	17.0	48.9	1.86
After 24 hours of reaction						
312	28.0	82.9	29.5	15.1	44.6	1.95
76	30.4	88.5	28.3	14.9	43.2	1.90
59	33.5	99.5	35.4	21.3	56.7	1.66
56	33.2	99.5	33.4	19.0	52.4	1.76

As can be seen in the table, Sn-MFI (Ludox) zeolites in as-made form are highly active for phenol hydroxylation. Hydrogen peroxide conversions are above 60% after 8 hours of reaction, with values reaching 92 – 96% for zeolites with the highest tin contents. After 24 hours, the zeolites made with the highest tin contents reach almost complete conversion, while for those with lower tin loadings the conversion is between 83 – 89%. The selectivity of hydrogen peroxide towards hydroquinone and catechol ranges between 46 – 56%, which is in line with the selectivities reported by Mal for calcined Sn-MFI (TEOS) zeolites. The remaining products correspond to "tar" species

that are known to form from non-selective hydroxylation and result in a dark brown coloration of the reaction solution. Formation of these species has been reported for Sn-MFI zeolites, and in some cases, for Ti-MFI (TS-1). The Cat/HQ ratio varies from 1.66 – 1.95. These ratios are in fact very comparable to those reported for calcined Sn-MFI (TEOS) zeolites, which range from 1.6 – 1.8. This is somewhat surprising considering that the reaction is most likely taking place on the external surface in the as-made samples, and yet, the Cat/HQ ratios are very similar to those reported for calcined materials. In general terms, the catalytic activity of as-made Sn-MFI (Ludox) samples is very comparable to the reported activity of calcined Sn-MFI (TEOS) zeolites.

As a control experiment (to check that no decomposition of TPA was taking place during reaction), thermogravimetric analysis (TGA) was performed on selected as-made Sn-MFI samples after catalytic testing. Prior to TGA, the zeolites were rinsed with acetone several times in order to remove tar species from their surface (tar species are easily removed by this procedure). TGA revealed that no decomposition of TPA had taken place. A weight loss of approximately 13 – 14% was recorded in a range from 100 – 600°C, which corresponds well to TPA cations occluded in the MFI framework and to the amount of organic material present in the as-made samples prior catalytic testing.

Catalytic testing of SnO_2 and silicalite-1 (all-silica MFI), in addition to a blank test reaction (no catalyst) were performed as additional control experiments in order to confirm that well dispersed tin sites are the active species in the reaction. The catalytic activity of SnO_2 after 24 hours was negligible (4% H_2O_2 conversion with no catechol or hydroquinone formation). The activity registered with silicalite-1 was also low. H_2O_2

conversion was around 9% with only a very small amount of catechol (7% selectivity to catechol and no formation of hydroquinone) and tar species formed. The activity observed in this case is most likely coming from solution impurities rather than the zeolite. Blank experiments (no catalyst added) revealed that significant activity can arise from the use of low purity reagents and water. If regular hydrogen peroxide bottles are used, specially combined with poorly deionized water, peroxide conversions up to 45% coming from the solution can be obtained. Activity from impurities in solution mainly leads to the formation of tar species and very small amounts of catechol. It was determined that by using properly distilled and deionized water along with ultrapure hydrogen peroxide (ULTREX from J.T. Baker), the activity from solution species was only about 9% in terms of hydrogen peroxide conversion with no formation of catechol or hydroquinone.

The information presented in Table 6.3 and the control experiments mentioned above show that the catalytic activity of Sn-MFI (Ludox) is due to tin sites present in the zeolites.

6.3.2.3 Changes in tin environment and activity implications

In order gain insights about the coordination of tin in the samples made with Ludox, and to understand their lack of activity in calcined form, Sn-MFI zeolites were made from gels with identical composition but using fumed silica as silica source instead of Ludox. The idea was to prepare zeolites that could be characterized using UV-Vis spectroscopy, but following synthesis conditions as similar as possible to those used for

Ludox samples. Two zeolites were prepared (gel Si/Sn = 150 and 50) and characterized by UV-Vis in as-made and calcined form. Calcination was done following two procedures. The first was done under flowing air (5 hours at 500°C), and the second one was done under nitrogen flow (6 hours at 500°C) followed by air flow (1 hour at 500°C) with a heating rate of 2°C/min. These conditions are the same used in Table 6.1. The results of these experiments are shown in Figure 6.2.

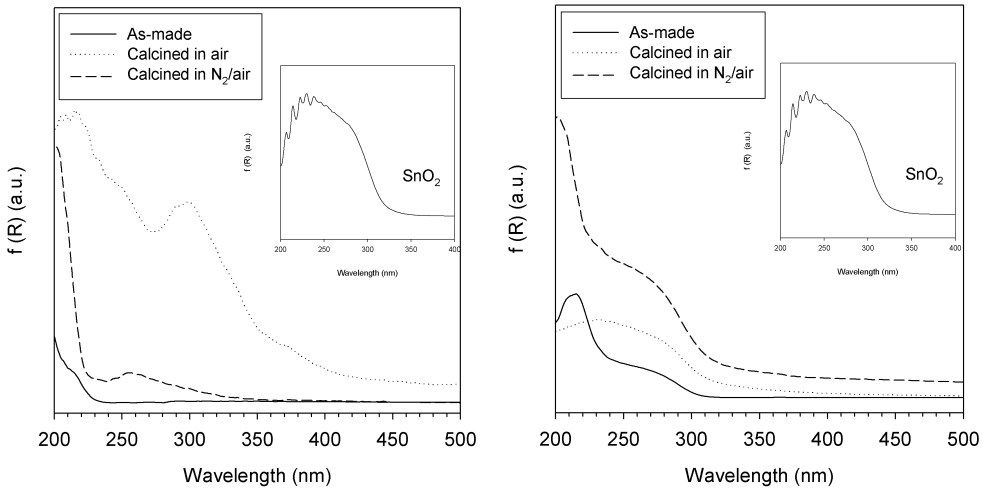

Figure 6.2 UV-Vis spectra of Sn-MFI zeolites made with fumed silica in as-made form and after calcination in air and N_2/air. Gel Si/Sn = 150 (left) and Si/Sn = 50 (right).

It can be seen that the coordination of tin is very sensitive to calcination treatments and varies also from sample to sample. The sample made with Si/Sn = 150 (left figure) exhibits an absorption maximum at 200 nm when it is in as-made form. Upon calcination under nitrogen/air conditions, the absorption maximum remains at 200 nm and another one of less intensity appears at approximately 260 nm. A major change in coordination occurs after calcination in flowing air, where two intense and broad

signals are present at approximately 215 – 220 nm and 300 nm respectively. The absorption band at 300 nm is likely due to SnO_2 species. The other bands at 200 nm, 220 nm and 260 nm represent lower coordination states, possibly tetrahedral and pentahedral coordination. The material made with Si/Sn = 50 shows somewhat different behavior. In the as-made form, two absorption maxima are found at approximately 220 nm and 280 nm, likely corresponding to tetrahedral and octahedral coordination respectively. After calcination under nitrogen/air conditions, the absorption at 220 nm moves to 200 nm while the one at 280 nm remains in the same place. After calcination in air, the absorption at 220 nm is greatly reduced and a broad signal covering a range from 200 – 280 nm is found. It is not clear why the coordination changes with the different calcination treatments and also between samples.

In an attempt to correlate catalytic activity with coordination environment, these materials were tested for phenol hydroxylation using the same protocol as before. Table 6.4 shows that results of these experiments.

Table 6.4 Activity data for Sn-MFI (fumed silica) samples after 24 hours. H_2O_2 is the limiting reagent (starting phenol/H_2O_2 = 3). The values listed for catechol (Cat) and hydroquinone (HQ) are the respective selectivities defined as (moles product)/(moles H_2O_2 reacted) x 100%.

Si/Sn	Treatment	H_2O_2 *(% Conversion)*	Cat	HQ	Total *(% Selectivity)*	Cat/HQ
150	As-made	3.2	0	0	0	
150	Calcined in *N_2/air*	11.5	0	0	0	
150	Calcined in *Air*	96	29.5	15.6	45.1	1.89
50	As-made	64.7	6.9	0	6.9	
50	Calcined in *N_2/air*	11.8	0	0	0	
50	Calcined in *Air*	22.3	0.1	0	0.1	

The results shown in Table 6.4 demonstrate a wide variability in catalytic behavior for the different samples and treatments. However, they can, in a form, be correlated with tin coordination environment. The sample with Si/Sn = 150 shows low activity in as-made form and after calcination in N_2/air. Only a small amount of tar species were produced and no catechol or hydroquinone was formed. The common characteristic of their UV-Vis spectra is the absorption maximum at 200 nm. When this sample was calcined in air, it showed very high activity (96%) and reasonable selectivity (~45%). The spectrum of this sample looks very different from the previous ones. The intense absorption maximum is found at 220 nm, although it also has another one at 300 nm. It is possible to assume that good catalytic activity is observed in samples that exhibit absorption bands at approximately 220 nm instead of 200 nm. This is supported by the data in Table 6.4 and also the spectra shown in Figure 6.1 for the Sn-MFI (TEOS) sample. In that case, it was also observed that the sample with absorption band at 220 nm was catalytically active while the sample with absorptions at 200 nm and 300 nm were not. It is not clear what the difference in absorption wavelengths represents in term of coordination environment. It is likely that both absorptions represent tetrahedral coordination but with a slight different environment, perhaps the presence of defects in tin sites versus fully coordinated tin. More investigations need to be conducted to elucidate this.

The sample made with Si/Sn = 50 was fairly active (~65%) in the as-made form, but exhibited low selectivity leading to a large formation of tar species. This sample exhibited an absorption band at 220 nm, which in accordance with the discussion above,

may be responsible for the higher activity. However, the low selectivity is surprising. It is possible that this can be an effect of tin species that absorb at 280 nm in that same sample. When this sample was calcined in N_2/air, the activity was low and comparable to that obtained for the lower tin content sample treated in the same way. In both cases, samples treated under N_2/air conditions showed absorption bands at 200 nm and low catalytic activity. After calcination in air, this sample showed a rather low activity (~22%) and negligible selectivity. In a sense, this is consistent with the interpretation of the UV-Vis data because this sample exhibits a very reduced 220 nm absorption and a wide 280 nm absorption maximum. In short, the coordination environment of the Sn-MFI samples studied varies considerably with calcination treatment and tin content. The results suggest that samples that exhibit absorption bands at approximately 220 nm are catalytically active while those with bands at 200 nm and 300 nm are not. It also seems that bands at 280 nm are associated with low selectivity.

Unfortunately, no direct comparison between samples made with Ludox and samples made with fumed silica seems possible. Catalyst poisoning was a persistent problem for calcined samples made with Ludox (regardless of calcination treatment) and high catalytic activity was never observed for any of these samples in calcined form. On the other hand, catalyst poisoning was not observed in samples made with fumed silica and high catalytic activity was observed in these samples provided that they contained UV-Vis absorption bands at 220 nm.

Even though insightful information relating tin coordination environment and catalytic activity was obtained through the use of zeolites made with fumed silica, the

issue of catalysts poisoning in Sn-MFI (Ludox) samples remains unexplained. These samples are very active in as-made form but poison when calcined. An explanation for this could be related to impurities present in Ludox. It is possible that the presence of impurities inside these zeolites could lead to formation of by products that bind more strongly to the active sites leading to poisoning or diffusion problems.

Considering the results obtained with as-made Sn-MFI (Ludox) samples and the reported activity data for calcined Sn-MFI (TEOS) in terms of activity, selectivity and especially Cat/HQ ratios, questions arise on whether catalysis occurs inside the zeolite pores or just in the outer surface. The activity and Cat/HQ ratios from as-made samples are very comparable to those from calcined ones, even though the pores of the zeolites are not accessible. This could be indicative that tin sites found in the outer surface (most likely tin sites with pendant OH groups) are the active species for this reaction. This could also be related to the two different UV-Vis absorption bands found at 200 nm and 220 nm, which seems to affect catalytic activity in a very different way, even thought they are both most likely representing tetrahedral tin sites.

6.4 Conclusions

The work presented in this chapter demonstrates that the coordination environment of tin in MFI frameworks is largely affected by calcination procedures and synthesis parameters that include tin content and silica source. Tin sites with tetrahedral, octahedral and even pentahedral coordination can be present in as-made zeolites or result from calcination procedures. This work also demonstrates that the catalytic activity of

these materials in phenol hydroxylation is deeply affected by tin environment. The results suggest that tetrahedral tin sites with pending OH groups are most likely the active species for this reaction. This is supported from the observation that as-made Sn-MFI zeolites catalyze the reaction with comparable activities, selectivities and Cat/HQ ratios than those reported with calcined materials. UV-Vis experiments seem to offer supporting evidence for this as well. Zeolites with tin sites that result in UV-Vis absorption at approximately 220 nm were catalytically active, while those that result in UV-Vis absorption at 200 nm were not. Both sites most likely represent tin in tetrahedral coordination but with slight different environment, perhaps due to the presence of the pending OH group.

Sn-MFI zeolites prepared with Ludox were highly active in as-made form but their activity was negligible after calcination due to what it seemed poisoning of the active sites. Poisoning was only observed in materials made with Ludox and not in those made with TEOS or fumed silica. This suggests that important differences can arise from the use of different silica sources and it needs to be investigated in more detail.

CHAPTER VII

CONCLUSIONS AND FUTURE WORK

7.1 Conclusions

The main objective of this dissertation was to study the single and simultaneous framework incorporation of germanium, boron, aluminum and tin in MFI zeolites using synthesis conditions that are attractive for industrial preparations. These include the use of mixtures in alkaline media with high concentration of precursor species. The general conclusion obtained from this work is that framework incorporation of these elements can be achieved, but it is highly influenced by pH, the concentration of the elements in the synthesis mixtures and the presence of sodium cations. Sodium cations are commonly included in industrial preparations through the use of sodium hydroxide, but we found that they negatively affect framework incorporation due to a tendency to form stable extra-framework impurities with the heteroatoms. This became apparent from the work done with germanium and tin, but similar findings have been reported for boron. The effect of pH and mixture composition on framework incorporation was found to vary depending on the heteroatom, but in general terms, these parameters have more influence on germanium and boron incorporation than for aluminum and tin. Aluminum is readily incorporated under the conditions studied while tin coordination environment is highly susceptible to post-synthesis treatments (although it is also dependent on synthesis conditions).

Three specific systems were studied in this dissertation. MFI zeolites with simultaneous incorporation of germanium and aluminum (i.e. Ge-Al-MFI zeolites), MFI zeolites with simultaneous incorporation of germanium and boron (i.e. B-Ge-MFI zeolites), and MFI zeolites with single incorporation of tin (i.e. Sn-MFI zeolites). The synthesis of Ge-Al-MFI from alkaline mixtures containing sodium cations was addressed in chapter III. From this work, it was concluded that aluminum readily incorporates in the framework with efficiencies close to 100% not affected by the presence of sodium cations or germanium/aluminum contents. Germanium incorporation efficiencies vary from 30 – 75%, but a portion of the germanium is actually present as a surface impurity caused by the presence of sodium. When this impurity is removed, the efficiencies range between 30 – 55%, likely representing germanium framework incorporation. Aluminum decreases the incorporation efficiency of germanium; while this efficiency also decreases when high germanium contents are used. This points out to a preferential incorporation of aluminum over germanium. The aluminum and germanium coordination states were probed using spectroscopic techniques leading to the conclusion that aluminum and at least a part of the germanium are found in the zeolite framework.

The synthesis of B-Ge-MFI zeolites from sodium-free alkaline mixtures was addressed in chapter IV. From this work, it was demonstrated that highly crystalline and phase pure B-Ge-MFI zeolites with tunable compositions and high boron and germanium incorporation efficiencies can be prepared when sodium ions are not present. Mixture pH and composition are the most influential factors to regulate the degree of

substitution. Germanium incorporation efficiencies are entirely controlled by pH, being close to 100% when the pH is below 12. Boron incorporation efficiencies (ranging from 30 – 70%) increase with decreasing pH values and decreasing boron content in the synthesis mixtures. Framework incorporation of boron leads to a decrease in the unit cell volume and can be directly probed by X-ray diffraction and ^{11}B MAS NMR. While framework incorporation of germanium is more difficult to assess, ^{11}B MAS NMR studies suggested that framework boron sites with germanium atoms as nearest neighbors exist. This can be indicative of germanium incorporation in the framework and also could potentially alter the stability of boron sites, and therefore the applications of these materials.

The synthesis of Sn-MFI zeolites from alkaline mixtures was discussed in chapter V. The role of sodium cations was investigated in detail by preparing the materials in the presence and absence of sodium. It was demonstrated that the presence of sodium cations leads to zeolites with significant amounts of a sodium stannate surface impurity that prevents the framework incorporation of tin. Even though the formation of the impurity can, up to some extent, be controlled by means of pH, it still affects the crystallinity and absorption capacity of the materials. It was also demonstrated that highly crystalline Sn-MFI zeolites with high absorption capacity and tin framework incorporation could be obtained through sodium-free syntheses. Typical incorporation efficiencies varied between 60 – 90%. Evidence supporting that framework incorporation of tin was taken place included changes in unit cell volume, changes in crystal symmetry and characteristic features in FT-IR and UV-Vis spectra.

Finally, the catalytic activity of Sn-MFI zeolites for the hydroxylation of phenol was studied in Chapter VI. The work presented in this chapter demonstrated that the coordination environment of tin is largely affected by calcination procedures and synthesis conditions that include tin content and silica source. A variety of tin sties including tetrahedral, octahedral and even SnO_2 impurities can form in these materials. The catalytic activity in phenol hydroxylation was highly affected by the different tin coordination environments. The results suggest that tetrahedral tin sites with pending OH groups are most likely the active species for this reaction. This is supported from the observation that as-made Sn-MFI zeolites catalyze the reaction with comparable activities, selectivities and Cat/HQ ratios than those reported with calcined materials. UV-Vis experiments also offer supporting evidence for this. Zeolites with tin sites that result in UV-Vis absorption at approximately 220 nm were catalytically active, while those that result in UV-Vis absorption at 200 nm were not. Both sites most likely represent tin in tetrahedral coordination but with slight different environment, perhaps due to the presence of the pending OH group.

7.2 Recommendations for future work

The investigations carried out in this dissertation represent an important advance for understanding the incorporation of heteroatoms in zeolite frameworks from mixtures that are of industrial interest. A clearer description of how various synthesis parameters affect the incorporation and properties of the substituted zeolites is now possible. Many different future directions related to this work can be envisioned, especially because the

incorporation of elements in zeolites diversifies the applications of these materials as catalysts. A few recommendations with the purpose to understand the implications of the heteroatom substitution in the properties and applications of the zeolites studied in this dissertation are outlined below.

7.2.1 Ge-Al-MFI zeolites

Considering that the negative effect that sodium cations have on germanium incorporation is now better understood, it would be advantageous to synthesize Ge-Al-MFI zeolites from sodium-free preparations. Improvements in germanium incorporation efficiencies can be expected from this, especially if the pH is carefully monitored. This will lead to materials with larger germanium contents that can make a more meaningful contribution to modify the properties of the zeolites. Once this is achieved, the question that needs to be addressed is how the presence of germanium affects the acidity and/or the potential catalytic activity/stability of these materials. This can be done by comparing the acid strength of Ge-Al-MFI with that of Al-MFI zeolites by means of temperature-programmed desorption of bases and catalytic testing in various reactions. From investigations done on Ge-Al-MFI zeolite prepared in fluoride media, it has been suggested that germanium incorporation does not affect the acidity of the materials but rather affects catalytic stability by modification of morphological features. This is a relevant issue, especially for applications in the petrochemical industry where aluminum-containing zeolites are used in a variety of acid catalyzed reactions. Since Ge-Al-MFI zeolites made from alkaline mixtures are more relevant for industrial

purposes, it will be advantageous to compare the findings of fluoride-mediated preparations with those obtained from zeolites prepared in alkaline media.

7.2.2 B-Ge-MFI zeolites

The simultaneous incorporation of boron and germanium was described in this dissertation for the first time. The motivation for incorporating germanium in zeolites containing boron was derived from the reported catalytic improvements that germanium can impart when combined with other elements like aluminum and titanium. Since a series of well characterized and highly crystalline B-Ge-MFI with tunable compositions has been synthesized here, it is recommended that studies are conducted to assess the effect of germanium in acidity and catalytic activity in reactions performed using B-MFI zeolites. The acidity effect can be investigated by conducting more detailed temperature-programmed desorption of ammonia experiments that the ones presented in chapter IV. Analysis of samples containing the same boron content but variable germanium composition would be a starting point. This can also be coupled with theoretical investigations. Several reactions conducted with B-MFI zeolites were mentioned in chapter I. Among those, the vapor phase Beckmann rearrangement of cyclohexanone oxime would be an interesting test reaction. It has been determined that active sites for this reaction are hydroxyl groups and silanol nests, which can be generated in B-MFI zeolites by different post-synthesis treatments that involve the removal of boron sites. Since boron is weakly bound to the framework, its removal can

be easily done. It would be interesting to determine if the presence of germanium, especially germanium atoms close to boron sites, can have any effect of this process.

7.2.3 Sn-MFI zeolites

The results described in chapter VI demonstrated that the coordination environment of tin in MFI zeolites was very sensitive to calcination procedures. In addition, tin coordination was also variable with tin content for samples made with fumed silica. There is still a need to obtain a clearer picture describing the relation between synthesis parameters (tin content, silica source and calcination treatment) and tin coordination. Some of these parameters were studied in this dissertation and the consequence of their effect on tin coordination was described. However, complete understanding of the underlying reasons leading to the effects observed is still missing. It is recommended that a more systematic investigation, that includes syntheses experiments with difference silica sources and tin contents coupled with UV-Vis and ^{119}Sn MAS NMR, be conducted. More attention should be paid to study the chemistry of tin in zeolites precursors mixtures.

A further investigation of the catalytic properties is also recommended, especially to understand the poisoning and low activity of Sn-MFI zeolites made with Ludox and the nature of the active sites for the reaction. The results obtained in this dissertation suggested that the active sites are tetrahedral tin species with pending OH groups. However, in order to confirm this, a larger number of experiments that include wider compositional ranges couple with UV-Vis spectroscopy need to be done. In

addition, it is recommended that other zeolite topologies be investigated. Topologies in which the amount of defect sites can be controlled would be of particular help.

7.2.4 Other potential systems

The study of other potential systems is also recommended. The simultaneous incorporation of aluminum/tin and aluminum/tin/germanium could be interesting for potential catalytic applications since two different types of acidities (Brønsted versus Lewis) would be present in those systems. Other promising systems could include tin/titanium and tin/titanium/germanium combinations. Again, simultaneous functionalities (Lewis acidity and Redox activity) would be achieved.

7.2.5 Effect of heteroatoms in zeolite nucleation and growth

A persistent finding during the work conducted for this dissertation was that the incorporation of the different heteroatoms in reaction mixtures seemed to affect the time for nucleation and crystallization of the zeolites. It was found that tin was effective at retarding the nucleation and growth of the material since tin-containing zeolites required longer times for formation with increasing tin contents. Germanium was also found to affect this but in the opposite way. Zeolites made in the presence of germanium crystallized in very short times. This is a fundamental problem that could be addressed when studying zeolite nucleation and growth and would lead to a better understanding of the interactions and chemistry occurring in zeolite precursor mixtures.

REFERENCES

1. National Research Council. *Catalysis Looks to the Future*, National Academy Press: Washington D.C., **1992**.

2. Hagen, J. *Industrial Catalysis: A Practical Approach*, Wiley: Weinheim, **2006**.

3. Barrer, R. M. *Hydrothermal Chemistry of Zeolites*, Academic Press Inc.: London, **1982**.

4. Čejka, J. *Introduction to Zeolite Science and Practice*, Elsevier: Oxford, **2007**; Vol. 168 of Studies in Surface Science and Catalysis.

5. Auerbach, S. M.; Carrado, K. A.; Dutta, P. K. *Handbook of Zeolite Science and Technology*, CRC Press: New York, **2003**.

6. Cundy, C. S.; Cox, P. A. *Chemical Reviews* **2003**, *103*, 663-701.

7. Sing, K. S. W. et al. *Pure and Applied Chemistry* **1985**, *57*, 603-619.

8. Csicsery, S. M. *Zeolites* **1984**, *4*, 202-213.

9. Corma, A. *Journal of Catalysis* **2003**, *216*, 298-312.

10. Corma, A. *Current Opinion in Solid State & Materials Science* **1997**, *2*, 63-75.

11. Cronstedt, A. F. *Forsok til Mineralogie, eller Mineral-Rikets Utstallning*, Stockholm, **1758**.

12. Masters, A. F.; Maschmeyer, T. *Microporous and Mesoporous Materials* **2011**, *142*, 423-438.

13. Damour, A. *Ann. Mines* **1840**, *17*, 191.

14. Eichorn, H. *Annual Review of Physical Chemistry* **1858**, 126.

15. Friedel, G. *Bull. Soc. Fr. Mineral. Crystallogr.* **1896**, 19.

16. Weigel, O. *Z. Kristallogr.* **1925**, 125-154.

17. Barrer, R. M. *Journal of the Chemical Society* **1948**, 2158.

18. Barrer, R. M. *Journal of the Chemical Society* **1948**, 127.

19. Breck, D. W.; Eversole, W. G.; Milton, R. M. *Journal of the American Chemical Society* **1956**, *78*, 2338-2339.

20. Breck, D. W. et al. *Journal of the American Chemical Society* **1956**, *78*, 5963-5971.

21. Breck, D. W. U.S. Patent 3,130,007 **1964**

22. Rabo, J. A.; Schoonover, M. W. *Applied Catalysis A-General* **2001**, *222*, 261-275.

23. Plank, C. J. *ACS Symposium Series* **1983**, *222*, 253-271.

24. Weisz, P. B.; Frilette, V. J. *Journal of Physical Chemistry* **1960**, *64*, 382-382.

25. Weisz, P. B. *Pure and Applied Chemistry* **1980**, *52*, 2091-2103.

26. Csicsery, S. M. *Pure and Applied Chemistry* **1986**, *58*, 841-856.

27. Weitkamp, J. *Solid State Ionics* **2000**, *131*, 175-188.

28. Barrer, R. M.; Denny, P. J. *Journal of the Chemical Society* **1961**, 971.

29. Barrer, R. M.; Denny, P. J.; Flanigen, E. M. BE Patent 6,153,311 **1962**

30. Wadlinger, R. L.; Kerr, G. T.; Rosinski, E. J. U.S. Patent 3,308,069 **1967**

31. Argauer, R. J.; Olson, D. H.; Landolt, G. R. GB Patent 1,161,974 **1969**

32. Flanigen, E. M. et al. *Nature* **1978**, *271*, 512-516.

33. McCusker, L. B.; Baerlocher, C. *Chemical Communications* **2009**, 1439-1451.

34. Fyfe, C. A.; Thomas, J. M.; Klinowski, J.; Gobbi, G. C. *Angewandte Chemie-International Edition in English* **1983**, *22*, 259-275.

35. Flanigen, E. M.; Patton, R. L. U.S. Patent 4,073,865 **1978**

36. Kessler, H. et al. *Zeolites* **1987**, *7*, 360-366.

37. Guth, J. L. et al. *ACS Symposium Series* **1989**, *398*, 176-195.

38. Wilson, S. T. et al. *Journal of the American Chemical Society* **1982**, *104*, 1146-1147.

39. Flanigen, E. M.; Lok, B. M.; Patton, R. L.; Wilson, S. T. *Pure and Applied Chemistry* **1986**, *58*, 1351-1358.

40. Lok, B. M. et al. *Journal of the American Chemical Society* **1984**, *106*, 6092-6093.

41. Beck, J. S. et al. *Journal of the American Chemical Society* **1992**, *114*, 10834-10843.

42. Kresge, C. T. et al. *Science and Technology in Catalysis* **1995**, *92*, 11-19.

43. Taramasso, M. U.S. Patent 4,410,501 **1983**

44. Davis, M. E. et al. *Nature* **1988**, *331*, 698-699.

45. Yilmaz, B.; Muller, U. *Topics in Catalysis* **2009**, *52*, 888-895.

46. Martinez, C.; Corma, A. *Coordination Chemistry Reviews* **2011**, *255*, 1558-1580.

47. Smith, J. V. *Chemical Reviews* **1988**, *88*, 149-182.

48. Database of Zeolite Structures: http://www.iza-structure.org/databases/, accessed on September 2012.

49. Davis, M. E.; Lobo, R. F. *Chemistry of Materials* **1992**, *4*, 756-768.

50. Kokotailo, G. T. et al. *Nature* **1978**, *272*, 437-438.

51. Dwyer, F. G.; Jenkins, E. E. U.S. Patent 3,941,871 **1976**

52. Guth, J. L.; Constantini, M.; Lopez, A.; Popa, J. M. U.S. Patent 5,399,336 **1995**

53. Vaughan, D. E.; Rice, S. B. U.S. Patent 4,933,161 **1990**

54. Skeels, G. W.; Chapman, D. M.; Flanigen, E. M. U.S. Patent 5,518,708 **1996**

55. Mal, N. K.; Ramaswamy, V.; Ganapathy, S.; Ramaswamy, A. V. *Journal of the Chemical Society-Chemical Communications* **1994**, 1933-1934.

56. Mal, N. K.; Ramaswamy, V.; Rajamohanan, P. R.; Ramaswamy, A. V. *Microporous Materials* **1997**, *12*, 331-340.

57. Mal, N. K.; Ramaswamy, A. V. *Journal of Molecular Catalysis A-Chemical* **1996**, *105*, 149-158.

58. Janiszewska, E.; Kowalak, S.; Supronowicz, W.; Roessner, F. *Microporous and Mesoporous Materials* **2009**, *117*, 423-430.

59. van Grieken, R. et al. *Microporous and Mesoporous Materials* **2009**, *119*, 176-185.

60. Corma, A.; Nemeth, L. T.; Renz, M.; Valencia, S. *Nature* **2001**, *412*, 423-425.

61. Nemeth, L. et al. *Studies in Surface Science and Catalysis* **2004**, *154*, 2626-2631.

62. Renz, M. et al. *Chemistry-A European Journal* **2002**, *8*, 4708-4717.

63. Corma, A.; Domine, M. E.; Nemeth, L.; Valencia, S. *Journal of the American Chemical Society* **2002**, *124*, 3194-3195.

64. Corma, A.; Domine, M. E.; Valencia, S. *Journal of Catalysis* **2003**, *215*, 294-304.

65. Corma, A.; Renz, M. *Angewandte Chemie-International Edition* **2007**, *46*, 298-300.

66. Moliner, M.; Roman-Leshkov, Y.; Davis, M. E. *Proceedings of the National Academy of Sciences of the United States of America* **2010**, *107*, 6164-6168.

67. Mal, N. K.; Ramaswamy, V.; Ganapathy, S.; Ramaswamy, A. V. *Applied Catalysis A-General* **1995**, *125*, 233-245.

68. Mal, N. K.; Bhaumik, A.; Kumar, R.; Ramaswamy, A. V. *Catalysis Letters* **1995**, *33*, 387-394.

69. Das, T. K.; Chaudhari, K.; Chandwadkar, A. J.; Sivasanker, S. *Journal of the Chemical Society-Chemical Communications* **1995**, 2495-2496.

70. Chaudhari, K. et al. *Journal of Catalysis* **1999**, *183*, 281-291.

71. Corma, A.; Navarro, M. T.; Nemeth, L.; Renz, M. *Chemical Communications* **2001**, 2190-2191.

72. Corma, A.; Navarro, M. T.; Renz, M. *Journal of Catalysis* **2003**, *219*, 242-246.

73. Samuel, P. P.; Shylesh, S.; Singh, A. P. *Journal of Molecular Catalysis A-Chemical* **2007**, *266*, 11-20.

74. Shah, P.; Ramaswamy, A. V.; Ramaswamy, V. *Chemistry Letters* **2006**, *35*, 860-861.

75. Sasidharan, M. et al. *Microporous and Mesoporous Materials* **2009**, *126*, 234-244.

76. Niphadkar, P. S. et al. *Catalysis Letters* **2009**, *133*, 175-184.

77. Boronat, M.; Concepcion, P.; Corma, A.; Renz, M. *Catalysis Today* **2007**, *121*, 39-44.

78. Boronat, M.; Corma, A.; Renz, M.; Viruela, P. M. *Chemistry-A European Journal* **2006**, *12*, 7067-7077.

79. Boronat, M. et al. *Journal of Catalysis* **2005**, *234*, 111-118.

80. Roman-Leshkov, Y.; Moliner, M.; Labinger, J. A.; Davis, M. E. *Angewandte Chemie-International Edition* **2010**, *49*, 8954-8957.

81. Nikolla, E.; Roman-Leshkov, Y.; Moliner, M.; Davis, M. E. *ACS Catalysis* **2011**, *1*, 408-410.

82. Gibbs, R. E. *Proceedings of the Royal Society of London Series A-Containing Papers of a Mathematical and Physical Character* **1926**, *113*, 351-368.

83. Laubengayer, A. W.; Morton, D. S. *Journal of the American Chemical Society* **1932**, *54*, 2303-2320.

84. Tripathi, A.; Johnson, G. M.; Kim, S. J.; Parise, J. B. *Journal of Materials Chemistry* **2000**, *10*, 451-455.

85. Lee, Y. et al. *Microporous and Mesoporous Materials* **2000**, *39*, 445-455.

86. Tripathi, A.; Kim, S. J.; Johnson, G. M.; Parise, J. B. *Microporous and Mesoporous Materials* **2000**, *34*, 273-279.

87. Tripathi, A.; Parise, J. B. *Microporous and Mesoporous Materials* **2002**, *52*, 65-78.

88. Healey, A. M. et al. *Microporous and Mesoporous Materials* **2000**, *37*, 165-174.

89. Johnson, G. M.; Tripathi, A.; Parise, J. B. *Microporous and Mesoporous Materials* **1999**, *28*, 139-154.

90. Johnson, G. M.; Tripathi, A.; Parise, J. B. *Chemistry of Materials* **1999**, *11*, 10.

91. Johnson, G. M.; Lee, Y. J.; Tripathi, A.; Parise, J. B. *Microporous and Mesoporous Materials* **1999**, *31*, 195-204.

92. Jones, R. H. et al. *Chemistry of Materials* **1992**, *4*, 808-812.

93. Conradsson, T.; Dadachov, M. S.; Zou, X. D. *Microporous and Mesoporous Materials* **2000**, *41*, 183-191.

94. Li, H.; Eddaoudi, M.; Richardson, D. A.; Yaghi, O. M. *Journal of the American Chemical Society* **1998**, *120*, 8567-8568.

95. Zhou, Y. M. et al. *Angewandte Chemie-International Edition* **2001**, *40*, 2166-2168.

96. Cascales, C. et al. *Chemistry of Materials* **2002**, *14*, 677-681.

97. Li, H. L.; Yaghi, O. M. *Journal of the American Chemical Society* **1998**, *120*, 10569-10570.

98. Gabelica, Z.; Guth, J. L. *Angewandte Chemie-International Edition in English* **1989**, *28*, 81-83.

99. Lopez, A.; Soulard, M.; Guth, J. L. *Zeolites* **1990**, *10*, 134-136.

100. Tuilier, M. H.; Lopez, A.; Guth, J. L.; Kessler, H. *Zeolites* **1991**, *11*, 662-665.

101. Kosslick, H. et al. *Journal of Physical Chemistry* **1993**, *97*, 5678-5684.

102. van de Water, L. G. A. et al. *Journal of Physical Chemistry B* **2003**, *107*, 10423-10430.

103. Cheng, C. H.; Juttu, G.; Mitchell, S. F.; Shantz, D. F. *Journal of Physical Chemistry B* **2006**, *110*, 21430-21437.

104. Cheng, C. H.; Juttu, G.; Mitchell, S. F.; Shantz, D. F. *Journal of Physical Chemistry B* **2006**, *110*, 22488-22495.

105. Corma, A.; Martinaranda, R. M.; Sanchez, F. *Journal of Catalysis* **1990**, *126*, 192-198.

106. Faraj, M. K. U.S. Patent 5,977,009 **1999**

107. Oldroyd, R. D.; Sankar, G.; Thomas, J. M.; Ozkaya, D. *Journal of Physical Chemistry B* **1998**, *102*, 1849-1855.

108. Zicovich-Wilson, C. M.; Corma, A. *Journal of Physical Chemistry B* **2000**, *104*, 4134-4140.

109. van de Water, L. G. A.; van der Waal, J. C.; Jansen, J. C.; Maschmeyer, T. *Journal of Catalysis* **2004**, *223*, 170-178.

110. van de Water, L. G. A. et al. *Chemphyschem* **2004**, *5*, 1328-1335.

111. Blasco, T. et al. *Journal of Physical Chemistry B* **2002**, *106*, 2634-2642.

112. Corma, V.; Diaz-Cabanas, M. J.; Fornes, V. *Angewandte Chemie-International Edition* **2000**, *39*, 2346-2349.

113. Corma, A. et al. *Angewandte Chemie-International Edition* **2001**, *40*, 2277.

114. Castaneda, R. et al. *Journal of the American Chemical Society* **2003**, *125*, 7820-7821.

115. Corma, A. et al. *Nature* **2002**, *418*, 514-517.

116. Corma, A. et al. *Nature Materials* **2003**, *2*, 493-497.

117. Paillaud, J. L.; Harbuzaru, B.; Patarin, J.; Bats, N. *Science* **2004**, *304*, 990-992.

118. Corma, A. et al. *Chemical Communications* **2004**, 1356-1357.

119. Taramasso, M.; Perego, G.; Notari, B. *Proceedings of the 5th International Zeolite Conference* **1980**, 40-48.

120. Taramasso, M.; Manara, G.; Fattore, V.; Notari, B. GB Patent 2,024,790 **1980**

121. Klotz, M. U.S. Patent 4,269,813 **1981**

122. Gabelica, Z.; Nagy, J. B.; Bodart, P.; Debras, G. *Chemistry Letters* **1984**, 1059-1062.

123. Scholle, K. F. M. G. J.; Veeman, W. S. *Zeolites* **1985**, *5*, 118-122.

124. Holderich, W. F. et al. *Proceeding of the 6th International Zeolite Conference* **1984**, 545-555.

125. Howden, M. G. *Zeolites* **1985**, *5*, 334-338.

126. Cichocki, A.; Parasiewiczkaczmarska, J.; Michalik, M.; Bus, M. *Zeolites* **1990**, *10*, 577-582.

127. Cichocki, A. et al. *Journal of the Chemical Society-Faraday Transactions* **1990**, *86*, 753-756.

128. Deruiter, R.; Jansen, J. C.; Vanbekkum, H. *Zeolites* **1992**, *12*, 56-62.

129. Guth, J. L.; Kessler, H.; Wey, R. *Proceedings of the 7th International Zeolite Conference* **1986**, 121-128.

130. Coudurier, G.; Vedrine, J. C. *Pure and Applied Chemistry* **1986**, *58*, 1389-1396.

131. Axon, S. A.; Klinowski, J. *Journal of Physical Chemistry* **1994**, *98*, 1929-1932.

132. Testa, F. et al. *Catalysis by Microporous Materials* **1995**, *94*, 349-356.

133. Chu, C. T. W.; Kuehl, G. H.; Lago, R. M.; Chang, C. D. *Journal of Catalysis* **1985**, *93*, 451-458.

134. Holderich, W. F. *Proceedings of the 7th International Zeolite Conference* **1986**, 827-834.

135. Takahashi, T.; Nishi, M.; Tagawa, Y.; Kai, T. *Microporous Materials* **1995**, *3*, 467-471.

136. Roseler, J.; Heitmann, G.; Holderich, W. F. *Applied Catalysis A-General* **1996**, *144*, 319-333.

137. Heitmann, G. P.; Dahlhoff, G.; Niederer, J. P. M.; Holderich, W. F. *Journal of Catalysis* **2000**, *194*, 122-129.

138. Clegg, W. *Crystal Structure Determination*, Oxford University Press: Oxford, **1998**.

139. Chester, A. W. and Derouane E.G. *Zeolite Characterization and Catalysis: A Tutorial*, Springer: London, **2009**.

140. Watts, J. F.; Wolstenholme, J. *An Introduction to Surface Analysis by XPS and AES*, Wiley: Chichester, **2003**.

141. Taramasso, M.; Perego, G.; Notari, B. U.S. Patent 4,410,501 **1983**

142. Thangaraj, A.; Kumar, R.; Mirajkar, S. P.; Ratnasamy, P. *Journal of Catalysis* **1991**, *130*, 1-8.

143. Millini, R.; Perego, G.; Bellussi, G. *Topics in Catalysis* **1999**, *9*, 13-34.

144. Coudurier, G. et al. *Journal of Catalysis* **1987**, *108*, 1-14.

145. Zones, S. I.; Hwang, S. J. *Microporous and Mesoporous Materials* **2003**, *58*, 263-277.

146. Hwang, S. J.; Chen, C. Y.; Zones, S. I. *Journal of Physical Chemistry B* **2004**, *108*, 18535-18546.

147. Song, M. Y.; Zhou, W. Z.; Long, Y. C. *Chinese Journal of Chemistry* **2004**, *22*, 119-121.

148. Elomari, S.; Burton, A.; Medrud, R. C.; Grosse-Kunstleve, R. *Microporous and Mesoporous Materials* **2009**, *118*, 325-333.

149. Shvets, O. V. et al. *Chemistry of Materials* **2011**, *23*, 2573-2585.

150. Deruiter, R. et al. *Zeolites* **1993**, *13*, 128-138.

151. Fild, C.; Shantz, D. F.; Lobo, R. F.; Koller, H. *Physical Chemistry Chemical Physics* **2000**, *2*, 3091-3098.

152. Soulard, M.; Bilger, S.; Kessler, H.; Guth, J. L. *Zeolites* **1987**, *7*, 463-470.

153. Millini, R. et al. *Microporous and Mesoporous Materials* **2000**, *35-6*, 387-403.

154. Sen, T.; Rajamohanan, P. R.; Ganapathy, S.; Sivasanker, S. *Journal of Catalysis* **1996**, *163*, 354-364.

155. Fejes, P.; Nagy, J. B.; Kovacs, K.; Vanko, G. *Applied Catalysis A-General* **1996**, *145*, 155-184.

156. Niphadkar, P. S. et al. *Materials Chemistry and Physics* **2009**, *114*, 344-349.

157. Engelhardt, G. and Michel, D. *High-Resolution Solid-State NMR of Silicates and Zeolites*, Wiley: Chichester **1988**.

158. Koller, H.; Lobo, R. F.; Burkett, S. L.; Davis, M. E. *Journal of Physical Chemistry* **1995**, *99*, 12588-12596.

159. Fickel, D. W.; Shough, A. M.; Doren, D. J.; Lobo, R. F. *Microporous and Mesoporous Materials* **2010**, *129*, 156-163.

160. Arean, C. O.; Palomino, G. T.; Geobaldo, F.; Zecchina, A. *Journal of Physical Chemistry* **1996**, *100*, 6678-6690.